UCLouvain

École polytechnique de Louvain

Design and construction of a dual-rotor aero-system for education and research

Auteur: **Tom Irgel**
Promoteurs: **Gianluca Bianchin, François Wielant**
Lecteur: **Nicolas Docquier**
Année académique 2025–2026
Master [120] : ingénieur civil électromécanicien

Abstract

This master's thesis presents the design, construction, and progressive validation of a dual-rotor aero-system intended for education and research in control engineering. The objective is to develop an in-house alternative to commercial platforms such as the Quanser Aero 2, whose mechanical design and embedded software are largely fixed. By designing the platform from scratch, the EPL control laboratory gains a system that can be modified, repaired, and adapted to future teaching and research needs.

The platform is developed through an incremental prototyping approach. A first aero-pendulum (AP) prototype is used to validate the main actuation and sensing chain on a single pitch axis. A second single-axis twin-rotor (SATR) prototype extends the system to two rotors while keeping the yaw axis mechanically constrained. Finally, the Twin Rotor MIMO System (TRMS) integrates both pitch and yaw degrees of freedom in a compact laboratory platform. This progression allows the mechanical structure, the brushless motor and ESC actuation chain, the encoder and IMU measurements, and the Raspberry Pi-based control architecture to be tested and validated step by step.

The mechanical and electrical design choices are documented in detail, which include the 3D-printed propeller cages, the pivot assemblies, the electrical power architecture, the PWM motor control, and the embedded sensing and acquisition code. A simplified dynamic model is derived and experimental drop tests are used to identify the pitch dynamics of the AP and SATR prototypes. Classical PID-based controllers, extended with gravity compensation when required, are then used as validation tools for the electromechanical design.

The results confirm that the proposed architecture is suitable for closed-loop control experiments on the AP and SATR prototypes, and that the final TRMS prototype constitutes a mechanically and electrically operational prototype for future MIMO control studies. The complete design files, source code, and experimental data are archived to support reproduction, maintenance, and further development, both within the EPL control laboratory and by other institutions wishing to reproduce the design and, if necessary, adapt it to their needs.

Acknowledgements

This thesis represents the culmination of several months of work, and also marks the end of my studies at UCLouvain. I would like to take this opportunity to express my gratitude to all the people who contributed to this project, whether through direct supervision, technical support, or simply by supporting me throughout the process.

First, I would like to express my sincere gratitude to my supervisor, Professor Gianluca Bianchin, for his guidance, availability, and valuable feedback throughout this master's thesis. His advice helped to structure the project and maintain a clear engineering direction from the first to the final steps of the project. I sincerely thank him for the trust he placed in me and for the guidance he provided. It has been a real pleasure to carry out this project under his supervision.

I am also deeply grateful to François Wielant for his constant technical support, practical advice, and constructive advice during the development of the platform. I learned a lot from him, and his contributions were particularly valuable in addressing the challenges encountered during the experimental and implementation phases of the project. His expertise in mechanical design, electronics, and control was invaluable, as well as his commitment to ordering the required components and helping with the 3D printing of the custom parts. It was a true pleasure to work with him, and I appreciate his patience and willingness to share his expertise.

Finally, I would like to thank my family and friends for their continuous support and encouragement throughout my studies. This project would not have been possible without their understanding and support, especially during the more challenging moments of the project.

Tom Irgel,
Louvain-la-Neuve,
June 2026.

Disclaimer: AI Usage

AI tools were used during the preparation of this master's thesis to improve the writing process. Claude helped with language editing, reformulation, structural suggestions, and assistance in clarifying technical explanations.

All AI-generated content was critically assessed, reviewed, and revised by the author to ensure technical accuracy, clarity, and coherence with the scientific content of the thesis.

The author remains fully responsible for the scientific content, accuracy, and integrity of this thesis.

GitHub

The CAD files, embedded control code, experimental datasets, additional scripts, and supplementary material associated with this thesis are available in the following GitHub repository:

https://github.com/Tomi0304/Master_thesis_documents

Contents

Abstract i

Acknowledgements ii

Disclaimer: AI Usage iii

GitHub iv

List of Symbols x

List of Figures xiii

List of Tables xvi

Introduction 1

1 System design and mechanical implementation 5

1.1 Design requirements and mechanical constraints 5

1.2 Component selection and mechanical implications 7

1.2.1 Selection criteria 7

1.2.2 Attitude sensor: BNO085 IMU 8

1.2.3 Angular position sensor: HEDS-5540 encoder 9

1.2.4 Propeller: Quarkzmann 8×4 CCW 9

1.2.5 Brushless motor: A2212 1000KV 10

1.2.6 Electronic speed controller: Basic ESC 30A 10

1.2.7 Embedded controller: Raspberry Pi 4 11

1.2.8 Power supply: VOLTCRAFT DPPS-16-30 11

1.2.9 Summary 12
1.3 The aero-pendulum prototype (AP) 12
1.3.1 Design rationale 12
1.3.2 Design and construction 13
1.3.3 Design outcomes and improvements 15
1.4 The single-axis twin-rotor prototype (SATR) 16
1.4.1 Design rationale 16
1.4.2 Design and construction 17
1.4.3 Design outcomes and improvements 20
1.5 The Twin Rotor MIMO System (TRMS) 21
1.5.1 Design rationale and evolution from the SATR 21
1.5.2 Pitch pivot architecture 22
1.5.3 Yaw pivot architecture 23
1.5.4 Rotating beam and routing 25
1.5.5 Tower and base 26
1.5.6 Mechanical locking pins 26
1.5.7 Design improvements and current status 27

2 Electrical Design and Embedded Architecture 29

2.1 System architecture overview 29
2.2 Sensors 31
2.2.1 BNO085 inertial measurement unit 31
2.2.2 HEDS-5540 quadrature encoder 32
2.3 Actuation chain 34
2.3.1 A2212 brushless motor 34
2.3.2 Electronic speed controller: Basic ESC 30A 35
2.3.3 Bench power supply (VOLTCRAFT DPPS-16-30) 36
2.4 Raspberry Pi 4 controller 36
2.5 Wiring and GPIO mapping 37
2.6 Embedded software architecture 37

2.6.1 Low-latency GPIO with pigpio 38
2.6.2 Real-time control loop 38

3 Control Study **41**

3.1 Dynamic modelling 42
3.1.1 Modelling approach and assumptions 42
3.1.2 Actuator model: effective static gain 43
3.1.3 TRMS 2-DoF Lagrangian model 45
3.1.4 Prototype-specific instantiation of the pitch equation 47
3.1.5 Sampling and discrete-time considerations 48
3.2 System identification 50
3.2.1 Identification strategy 50
3.2.2 Drop tests on the AP 51
3.2.3 Drop tests on the SATR 52
3.2.4 Motor, ESC, and propeller actuator 54
3.2.5 Summary of identified parameters 57
3.3 Controller synthesis 57
3.3.1 Controller structure: PID with gravity feedforward 58
3.3.2 Gravity feedforward on the reference angle 59
3.3.3 Anti-windup strategy 59
3.3.4 Encoder-based derivative filtering 60
3.3.5 Empirical tuning methodology 61
3.3.6 Tuned gains on the AP 62
3.3.7 Tuned gains on the SATR 63
3.3.8 Extension to the TRMS 64
3.4 Discussion on the control approach 65
3.4.1 Dependence on CAD-derived mass properties 65
3.4.2 Limitations of the SATR damping identification 65
3.4.3 Empirical feedforward and actuator limitations 66
3.4.4 Actuator asymmetry and workspace limitations 67
3.4.5 Summary 67

4 Experimental Validation **69**

4.1 Experimental setup 69

4.2 Validation on the aero-pendulum 70

4.2.1 Closed-loop step response and reachable pitch range 70

4.2.2 Disturbance rejection 73

4.2.3 Exploratory sinusoidal tracking 74

4.2.4 AP validation summary 75

4.3 Validation on the single-axis twin-rotor prototype 76

4.3.1 Closed-loop pitch step response 76

4.3.2 Disturbance rejection 79

4.3.3 Open-loop tail-rotor coupling 80

4.3.4 SATR validation summary 83

4.4 Validation summary 83

5 Conclusion: Improvements and Future Work **84**

5.1 Summary of contributions 84

5.2 Comparison with the Quanser Aero 2 86

5.3 Limitations of the current prototype 86

5.4 Future work 87

Bibliography **90**

Appendices **93**

A Specification Chart **94**

B U-shape connector **96**

C Connector M6 rod **97**

D M18 rod ring **98**

E Extended M18 rod ring **99**

F Pitch-axis lower connector **100**

G Pitch-axis upper connector **101**

H Yaw blocker connector **102**

I Motor link V2 **103**

J ESC lower connector **104**

K ESC upper connector **105**

L IMU connector **106**

M Propeller cage lower part **107**

N Propeller cage upper part **108**

List of Symbols

Kinematics, states & angles		
ψ	Pitch angle (generalised coordinate)	rad
ϕ	Yaw angle (generalised coordinate)	rad
$\dot{\psi}$	Pitch angular rate	rad/s
$\dot{\phi}$	Yaw angular rate	rad/s
ψ^*	Pitch reference angle	rad
ψ_{enc}	Pitch angle in the encoder convention	rad
Forces, torques & gravity		
τ_ψ	Generalised torque about the pitch axis	N m
τ_ϕ	Generalised torque about the yaw axis	N m
$\tau_1,\ \tau_2$	Thrust torques of the main / tail rotor	N m
$F_1,\ F_2$	Thrust forces of the main / tail rotor	N
M_g	Gravitational restoring moment ($M_g = m_{eq}\, g\, l_{cm}$)	N m
$f_\psi,\ f_\phi$	Viscous friction coefficients (pitch / yaw)	N m s/rad
Inertia & geometry		
$J_\psi,\ J_\phi$	Moments of inertia of the rotating subsystem (pitch / yaw)	kg m^2
m_{eq}	Equivalent arm mass	kg
l_{cm}	Centre-of-mass distance from the pivot	m
$l_1,\ l_2$	Distance from pivot to main / tail rotor	m
g	Gravitational acceleration	m/s^2
Actuator (motor–ESC–propeller)		
Δp	Signed PWM reduction from neutral, positive in the lifting direction	μs
K_{eff}	Effective static actuator gain	deg/μs
K_{lift}	Effective lifting actuator gain	deg/μs

K_{opp}	Effective opposing actuator gain	deg/μs
κ	Effective PWM-to-torque gain	N m/μs
τ_{actuator}	Actuator time constant	s
Control		
K_p	Proportional gain	–
K_i	Integral gain	–
K_d	Derivative gain	–
K_g	Gravity feedforward gain	–
ψ_{off}	Empirical angular offset	deg
u_ψ	Normalised control command, $u_\psi \in [-1, 1]$	–
u_g	Gravity feedforward term (normalised)	–
u_{lim}	Command saturation limit	–
$e(t)$	Tracking error	deg
$I(t)$	Integral state	deg s
$I_{\max}$	Integral anti-windup limit	deg s
α	First-order filter coefficient (derivative LP / complementary)	–
ω_n	Natural frequency of the pitch pendulum	rad/s
ζ	Damping ratio of the pitch pendulum	–
Timing		
T_s	Control-loop sampling period	s
Acronyms		
AP	Aero-pendulum (first prototype)	–
SATR	Single-Axis Twin-Rotor (second prototype)	–
TRMS	Twin Rotor MIMO System (final prototype)	–
BLDC	Brushless Direct Current (motor)	–
CAD	Computer-Aided Design	–
CFD	Computational Fluid Dynamics	–
CPR	Counts Per Revolution	–
DoF	Degree of Freedom	–
ESC	Electronic Speed Controller	–
FDM	Fused Deposition Modelling	–
GPIO	General-Purpose Input/Output	–
IMU	Inertial Measurement Unit	–

I^2C	Inter-Integrated Circuit (bus)	–
LQR	Linear-Quadratic Regulator	–
MIMO	Multiple-Input Multiple-Output	–
PD	Proportional–Derivative	–
PID	Proportional–Integral–Derivative	–
PLA	Polylactic Acid (3D-printing filament)	–
PWM	Pulse Width Modulation	–
RMSE	Root-Mean-Square Error	–
SISO	Single-Input Single-Output	–
UAV	Unmanned Aerial Vehicle	–

Note: the analytical model and identification use SI units (radians). Angles (ψ, ψ^*, ψ_{enc}) are expressed in radians in the model but the embedded controller handles them in degrees. Accordingly, the tracking error e, the integral state I and its limit $I_{\max}$ are reported in degrees (Tables 3.5–3.6), and the effective actuator gains K_{eff}, K_{lift}, K_{opp} are in deg/µs (Table 3.4). The PID output is normalised by 90° *into the dimensionless command u_ψ (Eq. 3.17). In Section 3.2.1, J and b denote J_ψ and f_ψ, and the subscripts "fit" and "CAD" distinguish identified from CAD-derived values.*

List of Figures

1 The Quanser Aero 2, a commercial dual-rotor platform used worldwide for aerospace controls education. The two rotors are mounted perpendicularly and the body can rotate freely around the pitch and yaw axes [2]. 1

1.1 The aero-pendulum prototype. The arm is mounted at the table edge with clamps and can rotate around the pitch axis in a single direction. The motor, propeller, and V1 cage are at the lower end; the pivot, bearings, and HEDS-5540 encoder are at the upper end. The BNO085 IMU is mounted on the arm at a position chosen to avoid collision with the connector block at the angular limit. 15

1.2 CAD model of the single-axis twin-rotor prototype (SATR). 18

1.3 Physical prototype of the SATR, mounted on a Bosch 50×50 structure in the laboratory. 19

1.4 CAD model of the TRMS. 22

1.5 Pitch bearing housing: (a) assembled, (b) cross-section. 23

1.6 Stepped cylindrical pocket machined in each half of the U-shape connector to receive a flanged ball bearing. 24

1.7 Cross-section of the yaw pivot through the M6 rod axis. From top to bottom: the upper bearing housed in the upper branch of the U-shape, the upper pair of half-rings pressing against the inner race of the upper bearing, the rotating beam (Bosch 20×20) clamped between the two pairs of half-rings, the lower pair of half-rings pressing against the inner race of the lower bearing, and the lower bearing housed in the lower branch of the U-shape. 25

1.8 Mechanical locking pin assemblies for the two pivots. 27

1.9 Assembled TRMS prototype in the laboratory. The final platform integrates the pitch and yaw pivots, the rotating beam, the two motor–propeller–cage assemblies, the IMU sensor and actuation chain, and the support tower. The complete structure is mounted on the same Bosch 50 × 50 structure used for the SATR, which provides a rigid support and a fixed reference frame for the pivot. 28

2.1 System-level wiring architecture of the dual-rotor platform. Thick lines represent the motor power connections, while thin lines represent logic and signal connections. The BNO085 IMU is connected to the Raspberry Pi through I^2C, and the two Basic ESC 30A units receive PWM commands from the Raspberry Pi while being powered by the bench power supply. The HEDS-5540 encoder and its dashed connections represent a reserved extension: the encoder was validated on the AP and SATR prototypes, but was not mechanically integrated into the final TRMS prototype at the time of writing. 30

3.1 Representative AP drop test used for passive-model identification. The measured encoder trajectory is compared with the simulated response obtained using the parameters $J_{\text{fit}}^{\text{AP}} = 78.4\,\text{g}\,\text{m}^2$ and $b_{\text{fit}}^{\text{AP}} = 7.95\,\text{mN}\,\text{m}\,\text{s/rad}$ identified on this specific run. The arm is released from $\psi(0) = -18.36°$, with the motor disarmed and the propeller free to rotate. The fit RMSE is 0.43°. 52

3.2 Passive drop test on the SATR (run with the highest identified damping). Grey markers correspond to the measured encoder angle, and the solid blue curve corresponds to the simulated passive-model response obtained with the fitted parameters $J_{\text{fit}}^{\text{SATR}}$ and $b_{\text{fit}}^{\text{SATR}}$. The motors were disarmed and the propellers were free during the test. The fit was restricted to $t \leq 1.7\,\text{s}$. 54

3.3 Static map of the AP actuator chain in the V1 cage configuration: steady-state pitch angle reached for each positive lifting PWM offset Δp (markers, mean over each PWM hold), together with a quadratic fit $\psi_{\text{ss}} \propto \Delta p^2$ giving $R^2 \approx 0.998$. The local slope around the closed-loop operating range gives the nominal gain $K_{\text{lift}} \approx 0.08$ deg/μs. 56

4.1 AP closed-loop step responses for the tested pitch setpoints. The responses at 10°, 20°, and 25° reach the commanded setpoint, whereas the 30° test reveals the actuator limit of the AP configuration. 72

4.2 PWM command during the AP step-response tests. The 30° run reaches the maximum lifting actuation limit, confirming that the corresponding steady-state error is caused by saturation of the actuation chain. 72

4.3 AP disturbance rejection test at a 20° setpoint. The arm is manually perturbed several times and returns toward the commanded pitch angle after each perturbation. 74

4.4 Exploratory AP sinusoidal tracking test. The measured response shows reduced amplitude and visible phase lag with respect to the reference, illustrating the tracking limitations of the AP configuration. 75

4.5 SATR closed-loop pitch step responses for the tested setpoints. The controller reaches all commanded angles with negligible steady-state error and without gravity feedforward. 78

4.6 PWM command during the SATR pitch step-response tests. The steady-state PWM remains in a similar range for all tested setpoints, reflecting the more balanced mass distribution of the SATR compared with the AP. 78

4.7 SATR disturbance rejection test at a 40° setpoint. The arm is manually perturbed and the controller returns the pitch angle towards the commanded position. 80

4.8 Open-loop SATR tail-rotor coupling test. The main rotor is kept at neutral throttle while the tail rotor command is stepped from neutral to maximum actuation. 82

4.9 Measured pitch angle as a function of the tail rotor PWM command. The parasitic pitch coupling remains small up to approximately 1250 µs and then increases rapidly. 82

List of Tables

1.1 Summary of the main design requirements. 7

1.2 Summary of the selected components. The embedded controller and the power supply were reused from the EPL laboratory stock. Nevertheless, their retail price is still given so that the full reproduction cost can be estimated. 12

2.1 Main electrical characteristics of the A2212 1000 KV motor, taken from the manufacturer's datasheet [6]. 34

2.2 PWM convention used by the BLHeli_S firmware in bidirectional mode. 35

2.3 GPIO allocation on the Raspberry Pi 4. 37

3.1 Main symbols used in the dynamic model of the platform. 49

3.2 CAD-based quantities used in the identification of the AP pitch dynamics. 51

3.3 CAD-based quantities used in the identification of the SATR pitch dynamics. 53

3.4 Identified parameters across the AP and SATR prototypes. CAD-derived quantities are extracted from the SolidWorks assembly with all materials assigned. The absolute mechanical parameters J_{fit} and b_{fit} are identified by Nelder–Mead optimisation on the free-drop trajectories. The agreement ratio $J_{\mathrm{fit}}/J_{\mathrm{CAD}}$ provides a cross-validation of the CAD-based mass model. The actuator chain is identified on the AP and assumed shared across prototypes, consistent with the bundled actuator model of Section 3.1.2. 57

3.5 Final tuned gains on the AP. 62

3.6 Final tuned gains on the SATR. 63

4.1 AP closed-loop step-response summary. The final angle is computed over the last five seconds of each run. The values for 10°, 20°, and 25° are averaged over three repeated runs, while the 30° case corresponds to a single limit test. 71

4.2 SATR closed-loop pitch step-response summary. The final angle is computed over the last five seconds of each run. 77

4.3 Open-loop tail-rotor coupling measured on the SATR. The main rotor is kept at neutral throttle while the tail rotor command is varied. 81

Introduction

Motivations

The control courses at the *École polytechnique de Louvain* (EPL, UCLouvain) are complemented by several laboratories that allow students to experiment with real control problems. Among them, a self-balancing two-wheeled robot based on the Balboa 32U4 platform [1] helps students understand the principles of stabilisation, while a coupled water-tank rig is used to explore Multiple-Input Multiple-Output (MIMO) level control. These two experiments are a solid basis for the study of control theory, but the EPL control laboratories aim to extend their experimental offer, and in particular to cover the case study of a Twin Rotor MIMO System (TRMS). The students would face challenges such as nonlinear dynamics, underactuation, and strong coupling between the rotor and body dynamics. These features are precisely what make the TRMS challenging to control and, consequently, particularly well suited for teaching advanced control concepts at UCLouvain.



Figure 1: The Quanser Aero 2, a commercial dual-rotor platform used worldwide for aerospace controls education. The two rotors are mounted perpendicularly and the body can rotate freely around the pitch and yaw axes [2].

The TRMS is a well-known laboratory platform for teaching and research in control engineering, particularly for aerospace control education. As shown in Figure 1, the TRMS consists of two propellers mounted perpendicularly at the end of a beam that can rotate freely around both pitch and yaw axes. Unlike a real helicopter, where lift is generated by changing the blade pitch angle, the TRMS controls its motion by varying the angular velocity of each rotor. Commercial platforms such as the Quanser Aero 2 [2] have become a reference for aerospace controls education worldwide.

While the Quanser Aero 2 is a mature platform, two characteristics make it less suitable for the needs of the EPL control laboratories. First, the platform is delivered as a sealed, ready-to-use unit: its mechanical structure cannot be modified, its CAD files are not distributed, and its internal wiring is not meant to be changed by students. This severely limits the possibility of extending the platform with additional sensors, modifying its geometry, or producing replacement parts. Second, the platform relies on the proprietary QUARC real-time toolbox, which requires the control loop to be implemented in the Simulink/MATLAB environment under a commercial licence, meaning that the embedded software architecture remains proprietary, and any evolution of the software stack depends on the editor's roadmap.

This context motivated the development of an in-house platform, designed from scratch to be documented, modifiable, and reproducible across multiple academic institutions. Many teaching laboratories face a similar limitation with commercial TRMS platforms: they provide mature ready-to-use experiments, but give limited access to the mechanical design, internal wiring, and embedded software required for maintenance, extension, and pedagogical adaptation. By providing the complete mechanical CAD, electrical schematics, and embedded source code, the proposed platform allows the EPL teaching team, and potentially other institutions, to extend the hardware (adding sensors, modifying the structural design, producing replacement parts) and to design guided laboratory exercises in which students engage directly with the control problem (tuning feedback gains, implementing sensor fusion, or comparing identification methods) on a transparent and reproducible experimental platform, without depending on any proprietary software.

Objectives

The main objective of this master's thesis is to design, build and progressively validate a functional Twin Rotor MIMO System (TRMS) from scratch, intended for use in future control laboratories at the *École polytechnique de Louvain* (EPL). The primary contribution lies in the **electromechanical design and construction** of the platform: the selection and integration of the actuation and sensing components, the design

and 3D printing of the custom parts, the wiring and embedded architecture, and the architectural choices that make the platform reproducible, modifiable, and maintainable within the EPL control laboratory. The platform is built from commonly available components and 3D-printed parts, which keeps the unit cost low and allows additional units to be built whenever needed. The complete mechanical CAD, electrical schematics, and embedded software are documented alongside the manuscript and archived in a public GitHub repository `Tomi0304/Master_thesis_documents` so that the platform can be reproduced and adapted by the EPL control laboratory and by other institutions.

To demonstrate that the electromechanical design fulfils its intended dynamic behaviour, the project also encompasses the closed-loop control of the platform. The control work is treated here as a validation tool for the electromechanical design rather than as an independent research contribution. The complete work is decomposed into three engineering fields:

- **Mechanical design and construction:** producing a structure capable of rotating around the pitch and yaw axes, while remaining safe for student use, transportable by a single person, and manufacturable on a standard desktop FDM 3D printer.
- **Electrical instrumentation and embedded architecture:** instrumenting the platform with orientation tracking on both axes, actuating it with two independently driven brushless motors, and closing the control loop on a Raspberry Pi 4 embedded computer.
- **Control synthesis and experimental validation:** deriving a dynamic model of the platform, identifying key parameters experimentally on the AP and SATR prototypes, synthesising PID controllers (with gravity feedforward when required), and using closed-loop experiments to validate the electromechanical design step by step. For the final TRMS prototype, the control structure is extended as a starting point for future pitch and yaw closed-loop tuning.

A distinctive feature of this work is its *incremental development process*. Rather than trying to build the full TRMS in one step, three prototypes of increasing complexity are produced successively: the aero-pendulum (AP), the single-axis twin-rotor prototype (SATR), and the full Twin Rotor MIMO System (TRMS). This incremental approach is beneficial because each prototype can isolate and validate a specific subset of the dynamics before moving on to the next stage, which limits the number of unknowns at any stage.

Thesis outline

The thesis is organised into four chapters, framed by this introduction and a concluding chapter on improvements and future work. Given the construction-oriented nature of this work, the theoretical background relevant to each engineering discipline is introduced inline in the corresponding chapter rather than gathered in a dedicated state-of-the-art chapter.

Chapter 1 presents the system design and mechanical implementation of the three prototypes. It begins by establishing the design requirements imposed by the educational context, then presents the selection of the main physical components, including the actuators and sensors, whose dimensions, mass, and mounting interfaces directly constrain the mechanical architecture. The three prototypes are then described one after another, justifying the structural choices made at each stage and showing how the lessons learned from the AP and the SATR guided the architecture of the final TRMS.

Chapter 2 details the electrical and embedded architecture shared by the three prototypes. The sensor and actuation chains are described, and the real-time control loop is presented. The chapter shows that the same hardware and software stack scales from the single-rotor AP to the full 2-DoF TRMS with only minor wiring adjustments.

Chapter 3 combines dynamic modelling, experimental identification and controller synthesis. A simplified dynamic model is first derived for the pitch dynamics and then extended to the TRMS configuration. The relevant parameters are identified experimentally from AP and SATR drop tests, and the actuator chain is characterised with sufficient detail for controller tuning. A controller structure, based on a PID controller and augmented with gravity compensation when required, is then synthesised, and its empirical tuning methodology is detailed for the AP and SATR prototypes.

Chapter 4 develops the experimental validation of the controller on the AP and SATR prototypes, through closed-loop step responses, disturbance rejection, and the open-loop characterisation of the tail-rotor coupling. These results are used to evaluate the electromechanical architecture and to define the remaining steps required for future pitch and yaw control of the final TRMS prototype.

The manuscript closes with the **Conclusion**, which summarises the main contributions, discusses the limitations of the current prototype, including the incomplete closed-loop MIMO validation of the TRMS and pending encoder integration. It also compares the developed platform with the Quanser Aero 2 in terms of adaptability and laboratory usability, and details future improvements such as CFD characterisation of the propeller cages, yaw and pitch encoder integration, and full MIMO control validation.

Chapter 1

System design and mechanical implementation

The mechanical platform is developed incrementally through three prototypes: the aero-pendulum (AP), the single-axis twin-rotor prototype (SATR), and the Twin Rotor MIMO System (TRMS). Each prototype has its own specific objectives: the AP validates the electrical chain, the choice of the motor and propeller, and the feasibility of designing a controller for the pitch axis. The SATR introduces the second rotor while keeping the yaw axis mechanically locked, allowing the validation of another controller for the pitch axis but in a balanced configuration and by taking into account the cross-coupling from the tail rotor to the pitch axis. Finally, the TRMS integrates the complete mechanical and electrical architecture for the two degrees of freedom. Its assembly and electrical operation validate the feasibility of the full platform, while complete MIMO control validation is left as future work. The chapter first defines the mechanical requirements imposed by the educational context. It then presents the selection of the main physical components from a mechanical-integration perspective, since their dimensions, mass, mounting interfaces, and safety constraints directly shape the prototypes. The three prototypes are then described one after another, highlighting their design rationale, construction, and lessons learned from each stage.

1.1 Design requirements and mechanical constraints

The design of the platform is motivated by the educational context in which it will be used: the EPL control laboratory where students are expected to interact directly with the system through guided experiments. In the present implementation, the real-time control loop is executed directly on the Raspberry Pi through Python scripts, while a MATLAB/Simulink interface is left as a possible future extension for laboratory use.

The functional requirements of the platform are inspired by the functionalities of the Quanser Aero 2 [2], which serves as a reference for the desired capabilities: two degrees of freedom (pitch and yaw axes), dual-rotor actuation, and attitude measurement on both axes. The main differences from the commercial platform are the cost and the possibility to modify the design and adapt it to the laboratory needs.

The primary functional requirement is to provide a dual-rotor system with two degrees of freedom in which the pitch and yaw axes can rotate as freely as possible, reproducing the coupled MIMO dynamics of a real TRMS. In the mechanical design, the pitch pivot is intended to allow 360° rotation in principle. In the implemented prototype, however, the usable pitch range is limited by cable routing. The yaw axis is limited to approximately ±60° (120° total) due to the mechanical constraints of the pivot.

Given that the platform is intended to be used by students in a supervised laboratory, safety is essential. Propeller cages must enclose each propeller to prevent any contact between the students and the rotating blades. The system is also powered exclusively from a laboratory bench supply, excluding LiPo batteries to avoid potential fires in a classroom environment.

Reproducibility is another key design requirement: every custom 3D-printed part must be easily manufacturable on a standard FDM 3D printer, and every purchased component must be easy to purchase at retailers. This ensures that every piece of the platform can be easily replaced if a component is damaged, and that the design is highly reproducible for scaling the laboratory in the future.

The base of the platform must fit within an A3 footprint ($420 \times 297\,\text{mm}$) so that it can be placed on existing laboratory benches without requiring any modification to the workspace. No constraint is imposed on the total mass of the system, except that it should be sufficiently light to be easily transported by a single person.

Finally, the platform must include attitude sensing on both axes (pitch and yaw) with sufficient accuracy and bandwidth for closed-loop control at a sufficient sampling rate.

The key parameter values are summarised in Table 1.1. The complete specification chart in the Functions / Functional Requirements / Constraints / Constraint Requirements format is provided in Appendix A.

Parameter	Requirement
Degrees of freedom	2 (pitch + yaw)
Actuation	Dual rotor
Pitch pivot capability	360° rotation
Usable pitch range	Limited by cable routing
Yaw range	Approximately ±60° (120° total)
Propeller cages	Mandatory (student safety)
Power supply	Mains-powered bench supply (no LiPo)
Base footprint	Intended to fit within A3 (420 × 297 mm)
Attitude measurement	Pitch and yaw
Custom parts fabrication	FDM 3D printing
Purchased parts availability	Common suppliers

Table 1.1: Summary of the main design requirements.

1.2 Component selection and mechanical implications

The next step after establishing the specifications consisted in selecting the main components that constitute the actuation and sensing chain of the TRMS. Although several of these components belong to the electrical architecture, they are introduced here because their dimensions, mass, mounting interfaces, and safety requirements directly impact the mechanical design. Their electrical implementation is detailed later in Chapter 2.

1.2.1 Selection criteria

Four criteria were used to evaluate potential components for the platform, which are listed below in decreasing order of importance for this project.

The first criterion is **performance**. The platform must be able to reproduce the dynamic characteristics of the Quanser Aero 2 [2], without aiming for an exact replication. This leads to concrete performance targets at the component level: sufficient motor thrust to move in every possible configuration about both the pitch and yaw axes, attitude sensing with adequate bandwidth and accuracy for closed-loop control at the targeted frequency, and bidirectional motor actuation to allow trajectory tracking for both axes.

The second criterion is **availability**. Components had to be available for purchase

from suppliers offering rapid delivery within Belgium, in particular Amazon, RobotShop, and Be-RS. Components requiring import from overseas resellers were naturally excluded due to the extended delivery times, as the iterative nature of the project would have made such delays incompatible with the project timeline.

The third criterion is the availability of complete **documentation**. Every component had to be accompanied by a datasheet that provided sufficient technical information to know exactly whether the component met the performance requirements, and to design the mechanical and electrical interfaces.

The fourth and final criterion is **cost**. This was not the primary concern for this project, but it was something that we considered during the selection process. If a component was available that met the performance, availability, and documentation criteria, but was significantly more expensive than alternatives, we would have considered the cheaper option.

Two components were already available from the existing EPL control laboratory stock and did not require purchase: the Raspberry Pi 4 used as the embedded controller of the platform, and the aluminium Bosch profiles (20×20 and 50×50, slot 10) used as structural elements. All other mechanical and electrical components were purchased for this project, and their choice is explained in the next sections. The following sections present the selected components in the order of the signal chain: attitude sensor, angular position sensor, brushless motor, electronic speed controller, embedded controller, and power supply.

1.2.2 Attitude sensor: BNO085 IMU

Closed-loop control of the TRMS requires simultaneous measurement of both pitch and yaw orientations, which excludes single-axis sensors and motivates the use of an inertial measurement unit (IMU). The selected sensor is the BNO085 IMU, mounted on a breakout board from Adafruit and connected to the Raspberry Pi via I^2C.

The key advantage of this IMU over the other alternatives considered is its on-chip sensor fusion: it provides quaternion outputs directly, which removes the need to implement a Kalman filter on the Raspberry Pi. This makes it well suited for a laboratory prototype whose objective is to validate the electromechanical architecture rather than to develop a dedicated sensor fusion algorithm.

From a mechanical integration point of view, the breakout board is compact and light enough to be mounted directly on the rotating arm or beam with limited impact on the mass distribution. Its position is adapted on each prototype to avoid mechanical interference while remaining close to the rotation axis when possible. The detailed

electrical interface, configuration, calibration procedure, and limitations of the selected orientation mode are described in Section 2.2.1.

1.2.3 Angular position sensor: HEDS-5540 encoder

Although the BNO085 IMU is in principle sufficient to measure pitch and yaw simultaneously, an optical quadrature encoder was added to the AP and SATR prototypes and kept in the architecture as a planned extension for the final TRMS prototype. The motivation for this addition is twofold. From a technical point of view, an optical encoder provides drift-free angular measurements with low latency and high resolution. These characteristics complement the attitude estimates provided by the IMU, which can be affected by fusion latency, high-frequency noise, and yaw drift depending on the selected orientation mode. From an educational perspective, the addition of a second sensor allows students to explore new concepts such as sensor fusion and Kalman filtering.

The chosen encoder is the HEDS-5540 from Avago [3]. It was selected following a recommendation by the co-supervisor, based on prior integration experience at the EPL control laboratory. It offers a resolution of 500 counts per revolution (CPR), which becomes 2000 counts per revolution after $\times 4$ quadrature decoding, equivalent to an angular resolution of 0.18° per tick. This resolution is lower than that of the encoders used on the Quanser Aero 2 [2] (2880 CPR for pitch, 4096 CPR for yaw) but sufficient for the control bandwidth targeted by this project. The encoder housing is designed for a 6 mm shaft, a constraint that directly influenced the mechanical design of the pivots on each prototype (Sections 1.3.2, 1.4.2, and 1.5.3). The detailed wiring, quadrature decoding, and integration into the real-time control loop are described in Section 2.2.2 of Chapter 2.

1.2.4 Propeller: Quarkzmann 8×4 CCW

The propeller is the first component that was selected for the platform, since its diameter and pitch directly determine the thrust performance and therefore constrain the choice of the motor and the ESC. The selection process of the propeller was guided by two requirements: the propeller must generate sufficient thrust to meet the performance targets defined in Section 1.1, and its diameter had to be small enough to keep the propeller cages within the A3 base footprint requirement.

The final choice was an 8-inch diameter propeller, the Quarkzmann 8×4 inch CCW model, whose static thrust performance was verified against the APC PER3 test bench data [4] and confirmed to satisfy the project requirements when paired with the A2212

1000 KV motor. Propellers of this size operate at low Reynolds numbers, a regime in which empirical performance data is needed because simple analytical predictions are unreliable [5]. The propeller is compatible with the motor shaft thanks to the supplied hole adapter. A 6×4 inch alternative was tested experimentally during the AP testing phase: equipped with the V1 cage, it failed to produce any visible elevation of the beam at full throttle, confirming that the combination of cage losses and the reduced diameter was incompatible with the static thrust requirement. Whether this smaller version would be sufficient on the balanced TRMS, given the V2 cage redesign, was not retested in the present work and is left as a possible cost-optimisation in future iterations. A $10''$ model was also considered but rejected, as the larger diameter would have required larger propeller cages, conflicting with the A3 footprint requirement.

On the SATR and TRMS prototypes, two such propellers are used, one for each rotor (main and tail), while the AP uses a single one mounted on the main rotor. Bidirectional but asymmetric thrust is achievable through the forward and reverse modes of the ESC. The thrust asymmetry, resulting from the CCW blade geometry, is characterised in Chapter 3.

1.2.5 Brushless motor: A2212 1000KV

For the actuation of the platform, brushless DC (BLDC) motors were selected over brushed DC motors for three reasons: higher power density, absence of mechanical brushes (eliminating brush friction and the associated friction torque), and longer service lifespan, which is particularly relevant in an educational laboratory context where the motors will be subjected to repeated testing cycles by students.

The selected motor is the A2212 1000 KV [6], a brushless outrunner motor widely used in UAV projects. Its 3.2 mm shaft is compatible with the selected propeller through a supplied hole adapter, and its rated maximum current of 13 A per motor sets the lower bound for the ESC sizing developed in Section 1.2.6. A first motor candidate, the Hawk's Work 2212 920 KV, was purchased but rejected after delivery due to an incompatibility between the motor shaft and the propeller. The detailed mechanical interface between the motor and the beam is described in Sections 1.3.2, 1.4.2, and 1.5.7.

1.2.6 Electronic speed controller: Basic ESC 30A

The BLDC motors are controlled by electronic speed controllers (ESCs), which convert the PWM commands generated by the Raspberry Pi into the three-phase currents that drive the motor windings. The ESC was selected based on two criteria. First, it must support bidirectional operation, allowing each motor to produce thrust in both

directions; this is required on the full TRMS to enable bidirectional trajectory tracking on both pitch and yaw axes. Second, it must deliver the maximum motor current with sufficient margin. Each ESC drives a single A2212 motor. Since the motor datasheet specifies a maximum current of 13 A per motor, the 30 A continuous rating of the Basic ESC provides a comfortable margin for each actuation channel. The two-motor worst case, approximately 26 A, is instead used to size the bench power supply.

The chosen model is the Basic ESC 30A from Blue Robotics [7]. It is shipped with the BLHeli_S firmware, which supports bidirectional operation natively, without requiring firmware modifications. The detailed PWM mapping, slew-rate limiter, and arming procedure are documented in Section 2.3.2 of Chapter 2. The asymmetric thrust response between forward and reverse directions, identified during system identification, is reported in Chapter 3.

1.2.7 Embedded controller: Raspberry Pi 4

The embedded controller executes the real-time control loop, acquires sensor data, and generates PWM commands for the ESCs. Three criteria guided its selection: a sufficient number of GPIO and bus interfaces to connect the sensor suite (I^2C for the BNO085, two GPIO channels for the HEDS-5540 quadrature signals) and the actuation chain (two hardware PWM channels for the ESCs), support of a complete Linux distribution, and full compatibility with the maintained Adafruit Python driver for the BNO085 selected in Section 1.2.2.

The selected unit is the Raspberry Pi 4 Model B with 8 GB of RAM [8], which satisfies all three criteria. The 40-pin GPIO header provides sufficient margin for the required interfaces and future hardware additions, and the official Raspberry Pi OS supports remote code editing through VS Code over SSH, which facilitates the development process. An additional practical consideration was that a unit was already available from the EPL control laboratory stock, which eliminated procurement delays. The full software stack is described in Section 2.6 of Chapter 2.

1.2.8 Power supply: VOLTCRAFT DPPS-16-30

The actuation chain is powered by a laboratory bench power supply rather than by LiPo batteries. This choice was motivated by three considerations. First, LiPo batteries introduce a fire risk if physically damaged or improperly charged, which is incompatible with the safety requirements of a student laboratory. Second, a mains-powered bench supply removes the operational burden associated with batteries (charging cycles, dedicated storage, and life monitoring), which would be impractical to maintain in a

teaching environment. Third, a bench supply delivers a constant voltage over time, whereas a LiPo battery voltage decreases during discharge, which would introduce a slow but significant variation in the system dynamics during operation.

The selected unit is the VOLTCRAFT DPPS-16-30 [9], which can deliver up to 16 V at 30 A. This rating provides sufficient margin for the platform: the A2212 1000 KV motor operates nominally at 12 V, and the two-motor maximum current remains below the 30 A continuous rating (Section 1.2.6). The supply also features a USB interface for voltage and current logging, which is exploited during the system identification campaigns reported in Chapter 3. The detailed wiring and integration into the control loop are described in Section 2.3.3 of Chapter 2.

1.2.9 Summary

The selected components and their key specifications are summarised in Table 1.2. This component set defines the mechanical and electrical envelope within which the rest of the project is developed: the structural design presented in the following sections is conceived to accommodate these components, and the dynamic model of Chapter 3 is derived for the actuation and sensing capabilities listed below.

Table 1.2: Summary of the selected components. The embedded controller and the power supply were reused from the EPL laboratory stock. Nevertheless, their retail price is still given so that the full reproduction cost can be estimated.

Component	**Selected model**	**Unit cost**
Attitude sensor (IMU)	Bosch BNO085 (Adafruit breakout)	48.92 €
Angular position sensor	Avago HEDS-5540 (500 CPR optical)	59.65 €
Brushless motor	A2212 1000 KV (×2 + spare)	10.99 €
Propeller	Quarkzmann 8 × 4 inch CCW	12.49 €
Electronic speed controller	Basic ESC 30A (BLHeli_S firmware) (×2)	44 €
Embedded controller	Raspberry Pi 4 Model B (8 GB)	158.53 €
Power supply	VOLTCRAFT DPPS-16-30 (16 V / 30 A)	247.90 €

1.3 The aero-pendulum prototype (AP)

1.3.1 Design rationale

The aero-pendulum is the first prototype developed in the incremental design of the TRMS. It is also a classical low-cost benchmark for teaching linear and nonlinear feedback-control principles [10], which serves as a logical step before introducing the full twin-rotor dynamics. Its primary objective is not to reproduce the full dynamics

of the TRMS, but rather to validate fundamental elements of the system that will be reused in the following prototypes.

Specifically, the AP is used to:

- experimentally characterise the thrust performance of the chosen BLDC motor with its 8-inch propeller, both with and without the propeller cage;
- verify the correct operation of the complete electrical chain (ESC, Raspberry Pi, IMU, encoder);
- evaluate the performance of a PID controller with gravity feedforward on the pitch angle.

The design of the AP deliberately corresponds to a worst-case configuration in terms of thrust: the motor is attached at the end of the Bosch rail and a heavy propeller cage (referred to as V1) is mounted around it. This ensures that if the motor is capable of lifting the arm in that scenario, it will also be suitable for the next prototypes (SATR and TRMS), which feature more favourable mass distributions. The lessons learned from the AP, particularly regarding the cage design, are detailed in Section 1.3.3.

1.3.2 Design and construction

The aero-pendulum consists of a 0.4 m aluminium Bosch 20×20 rail which serves as the pendulum arm. The pivot is located at one end of the arm and the motor–propeller–cage assembly at the other end. The pivot is mounted at the edge of a laboratory table using clamps, so that the arm hangs vertically downwards in its rest position, free to rotate around the pitch axis. The angular range is limited to approximately 100° in a single direction from the rest position (vertical, arm pointing downwards), constrained by contact between the Bosch rail and the connector block. Rotation in the opposite direction is prevented by the table itself.

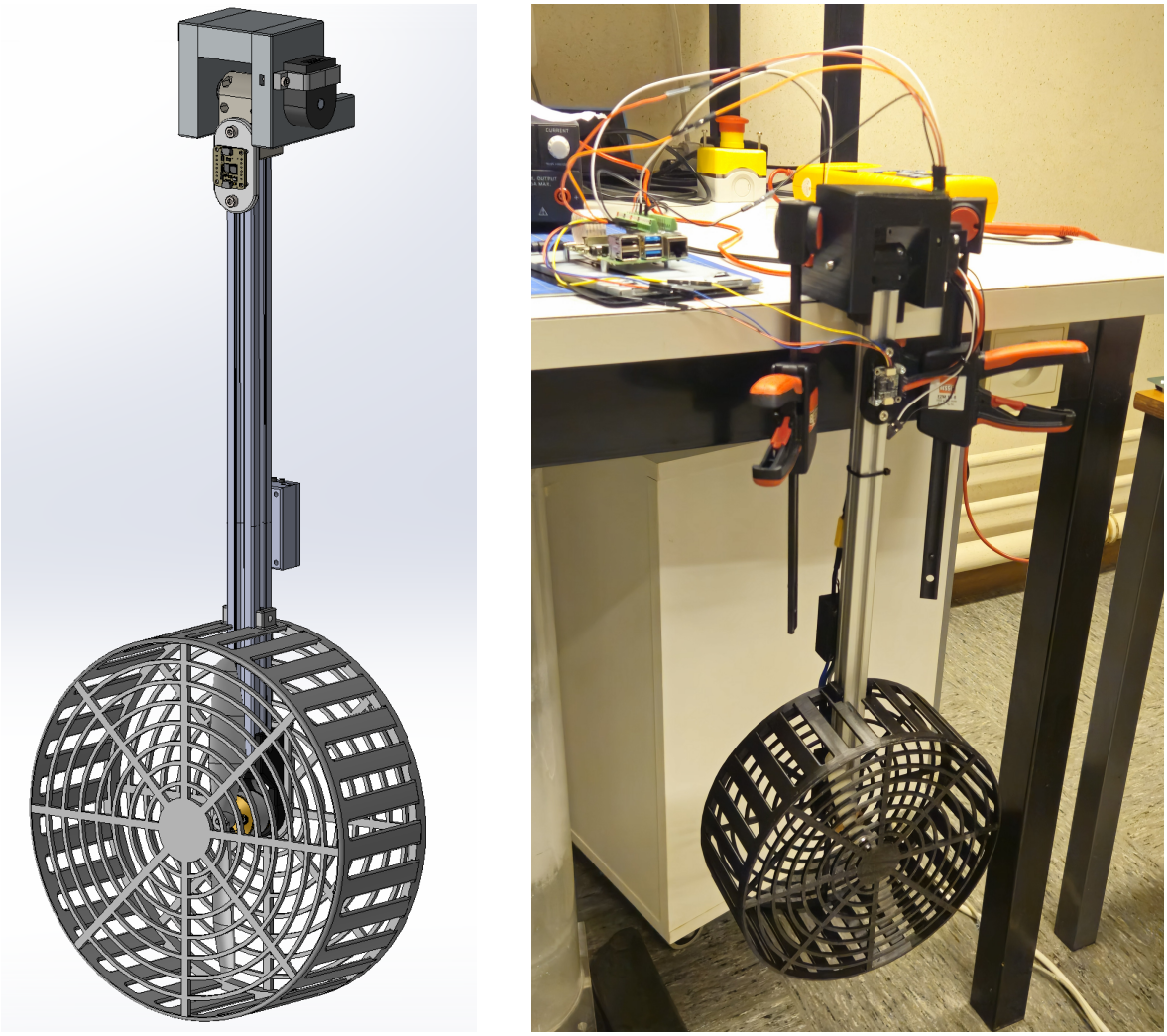
The pivot is built around an aluminium M6 rod, whose 6 mm diameter was specifically chosen to match the housing of the HEDS-5540 encoder (Section 1.2.3), enabling direct mounting without an additional adapter. The rod is supported by two flanged ball bearings (6 mm ID, 13 mm OD), whose outer races are inserted into a dedicated 3D-printed connector block. The rod is fitted to the inner races of the bearings, so that it rotates freely within the connector block. A second 3D-printed part clamps onto the rod using M3 screws and receives the Bosch 20×20 rail, making the arm and the rod rotate as a single rigid body. The HEDS-5540 encoder [3] is housed in a dedicated pocket within the connector block, with the M6 rod passing through its central bore and

clamped to the encoder's rotor via a set screw. This ensures that the encoder's rotor follows the arm while its housing remains stationary, referenced to the fixed connector block. The IMU [11] is mounted at a certain position along the rail chosen to provide clearance with the connector block when the arm reaches its upper angular limit.

At the lower end of the arm, an A2212 BLDC motor [6] is attached via a 3D-printed motor link, which is bolted to the Bosch rail through M4 screws and matching slot nuts inserted into the rail's profile slots. The motor is fastened to the motor link using M3 screws, and an 8-inch CCW propeller is mounted on the motor shaft with the provided propeller adapter. Both motor and propeller are enclosed in a propeller cage (version V1) that is printed in PLA, split into two parts (upper and lower) and assembled around the motor link and the arm using M4 screws. This cage is taller than the future version V2 used on the SATR and TRMS, which makes the pendulum heavier and more penalising in terms of aerodynamic efficiency.

The ESC is rigidly attached to the arm through a dedicated 3D-printed bracket, both to keep its mass coupled to the pendulum (avoiding dangling components that would interfere with the dynamics) and to protect it from mechanical impacts. Power cables are fixed to the arm with zip ties and the signal cables are routed from the sensors and ESC to the Raspberry Pi 4, which sits on the table next to the pivot.

Figure 1.1 shows the SolidWorks CAD model alongside the physical prototype installed in the laboratory.



(a) CAD model (b) Physical prototype

Figure 1.1: The aero-pendulum prototype. The arm is mounted at the table edge with clamps and can rotate around the pitch axis in a single direction. The motor, propeller, and V1 cage are at the lower end; the pivot, bearings, and HEDS-5540 encoder are at the upper end. The BNO085 IMU is mounted on the arm at a position chosen to avoid collision with the connector block at the angular limit.

1.3.3 Design outcomes and improvements

The AP prototype met its primary validation objective: it confirmed that the A2212 BLDC motor with an 8-inch propeller is capable of producing sufficient thrust to lift the pendulum arm even in the worst-case configuration (heavy V1 propeller cage). This result provided confidence that the motor would also be suitable for the SATR and TRMS, where the second rotor at the opposite end of the beam mechanically balances the system.

The most valuable outcomes drawn from this stage concern the design of the propeller cage. The first design (V1) of the cage enclosed the propeller, the motor, and even the

motor link, resulting in a tall and heavy structure that added significant mass at the end of the arm and restricted the reachable pitch range at full throttle. This observation directly motivated the redesign of the cage into a more compact version (V2) for the later prototypes, which encloses only the propeller. This second version reduces both the height and total mass by leaving the motor and motor link outside the cage, while still providing full propeller protection for the students during laboratory sessions.

The pivot connector also required a redesign. On the AP, the connector received the rail at its end, whereas the SATR requires the Bosch 20×20 rail to pass through the connector at its centre. Anticipating this geometrical constraint led to a redesign of the pivot used for the next prototypes.

Finally, the electrical chain (ESC calibration, PWM generation, IMU reading, encoder decoding, and Raspberry Pi communication) was validated on this prototype, confirming that all building blocks function correctly before introducing the complexity of a second rotor. A PID controller with gravity feedforward was implemented on the pitch axis and demonstrated stable closed-loop behaviour, with the detailed synthesis and experimental evaluation reported in Chapter 3.

1.4 The single-axis twin-rotor prototype (SATR)

1.4.1 Design rationale

The single-axis twin-rotor prototype (SATR) is the second stage in the iterative development of the TRMS platform. While the AP validated the electrical chain and the thrust capabilities of a single rotor in a worst-case pendulum configuration, the SATR adds a second rotor (tail rotor) and a quasi-symmetric beam configuration. Its objectives are threefold: to validate the quasi-symmetric beam design by demonstrating the feasibility of closed-loop pitch stabilisation, to verify the proper functioning of the second electrical chain (tail motor and ESC), and to expose any unexpected cross-axis coupling effects introduced by the dual-rotor structure before moving on to the full TRMS.

Unlike the AP, which hangs from the edge of a table, the SATR is mounted on an existing Bosch 50×50 aluminium structure present in the laboratory, providing a more rigid and reliable support. The pivot is located at the centre of the beam, with one motor-propeller assembly on each side, mirroring the perpendicular rotor configuration of the final 2-DoF TRMS. On the SATR, however, the yaw axis is mechanically blocked by the flanged bearings, which only allow rotation in the pitch plane.

A small residual asymmetry remains in this nominally symmetric configuration: the

BNO085 IMU and its mount are placed on the main-rotor side of the beam for cable routing convenience. As a result, the beam rests automatically at a vertical orientation rather than in indifferent equilibrium: the main rotor side at the bottom and the tail rotor side at the top, which produces a small residual gravitational torque that the controller must compensate.

In an idealised model, the tail rotor's thrust acts perpendicular to the pitch plane, producing zero torque about the pitch axis. The closed-loop control campaign on the SATR is thus restricted to the main rotor, while the tail rotor and its electrical chain are validated independently in open-loop. This restriction allows the pitch controller to be designed and tuned before introducing the cross-coupling effects of the tail rotor. In practice, the decoupling assumption is not exact: a small residual coupling is observed and is discussed in the lessons learned (Section 1.4.3) and quantified in Chapter 4.

1.4.2 Design and construction

The SATR consists of a 0.5 m aluminium Bosch 20 × 20 rail serving as the main arm, with a motor–propeller–cage assembly at each end and the pivot at the centre. Both propellers are enclosed in the redesigned V2 cages introduced as a result of the AP lessons learned (Section 1.3.3): these cages surround only the propeller and not the brushless motor, which significantly reduces both the cage volume and the mass concentrated at the arm extremities.

The pivot was redesigned to adapt to the new geometry of the SATR. The Bosch 20 × 20 rail passes through the 3D-printed connector block at its centre, and the aluminium M6 rod traverses a transverse hole drilled through the rail. The rod is tightened to the rail using a 3D-printed part fixed with M3 screws, so that the rod and the arm rotate together as a single body. Two flanged ball bearings (6 mm ID, 13 mm OD), identical to those used on the AP, are pressed into each of the two connector blocks, and the rod rotates within the bearings. The connector blocks are then bolted to the Bosch 50 × 50 structure using M8 T-bolts.

At each tip of the arm, an A2212 brushless motor is mounted via a redesigned 3D-printed motor link (version V2), which is bolted to the rail using M4 screws. Each motor is equipped with an 8-inch CCW propeller enclosed in a V2 propeller cage. The ESCs are mounted on each side of the arm through the same 3D-printed connectors used on the AP, and the BNO085 IMU is fixed on the rail close to the pivot. Unlike on the AP, where this position was constrained by the upper angular limit of the arm, the pivot geometry of the SATR allows the IMU to be placed as close as possible to the rotation axis. The HEDS-5540 encoder is coupled to the M6 rod at the pivot, using the same pocket and screw arrangement as on the AP, so that it rotates with the arm while

its housing remains referenced to the fixed connector block. Signal and power cables are routed along the arm and along the Bosch 50×50 structure to the Raspberry Pi 4 and the VOLTCRAFT bench supply.

Figures 1.2 and 1.3 show the SolidWorks CAD model and the physical prototype, respectively.

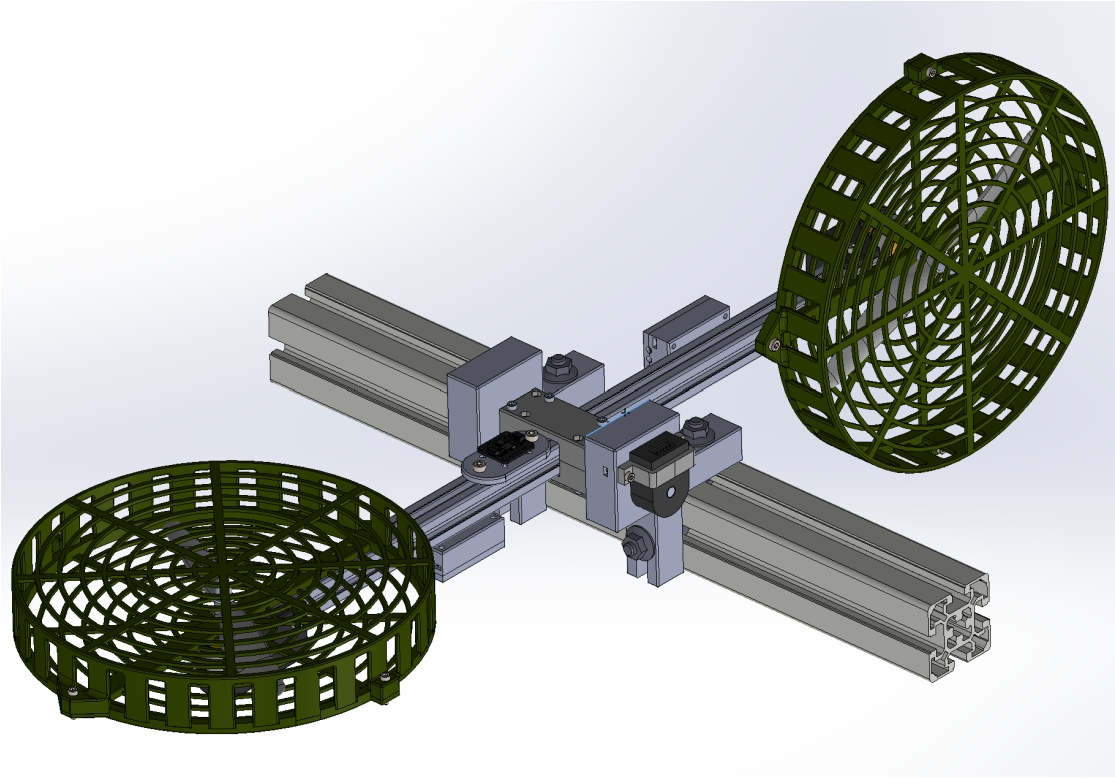


Figure 1.2: CAD model of the single-axis twin-rotor prototype (SATR).

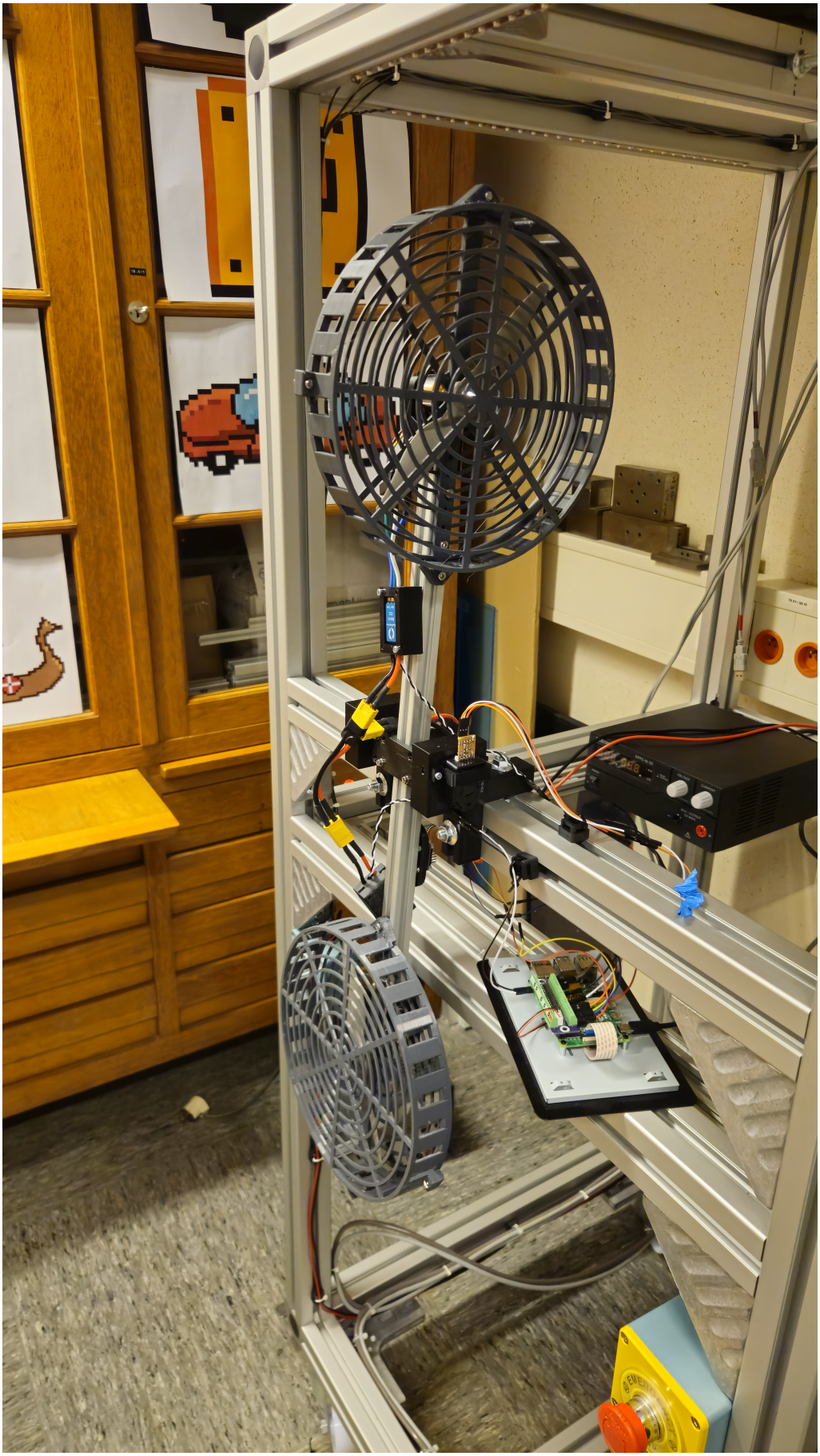


Figure 1.3: Physical prototype of the SATR, mounted on a Bosch 50×50 structure in the laboratory.

1.4.3 Design outcomes and improvements

The SATR validated the quasi-symmetric beam design under closed-loop pitch control. The mass redistribution introduced by the centred pivot and the additional tail motor eliminated the need for the explicit gravity feedforward term required on the AP, with the small residual asymmetry due to the IMU placement being fully compensated by the integral action of the PID. The detailed gains and performance metrics are reported in Chapter 4.

As expected from the change in mass distribution, the closed-loop gains were re-tuned rather than transferred directly from the AP. The removal of the gravity feedforward was made possible thanks to the new mass distribution of the SATR. That same near-symmetry, however, almost cancels the gravitational restoring moment that naturally anchors and stabilises the AP about its rest position (quantified later in Section 3.2.3). With this natural restoring action largely nonexistent, the SATR pitch dynamics behave closer to those of a freely pivoting inertia with little stabilisation, an effect that becomes more pronounced as the tested setpoints approach the horizontal. The derivative gain was therefore increased, compared to the AP configuration, to provide the damping and stabilisation that gravity no longer provides. The integral gain stayed the same, but with a lower anti-windup limit to prevent windup during the rise phase.

The second electrical chain (tail motor and ESC) was validated independently through open-loop tests. The tail motor worked as expected, responding correctly to PWM commands across its operating range. However, during the open-loop characterisation, a non-negligible parasitic coupling affecting the pitch axis was observed, becoming significant above a certain value of the tail PWM command. This observation confirmed early in the design process that the SATR cannot be treated as a completely decoupled SISO system, even though the yaw axis is mechanically blocked. Identifying this effect early directly motivated the dedicated open-loop characterisation of the tail-rotor coupling reported in Chapter 4, and flagged it as a key phenomenon to take into account for the future MIMO control of the full TRMS.

Finally, the installation of the SATR on a rigid Bosch 50×50 structure, compared to the table clamping used for the AP, significantly improved the mechanical stability of the system and provided a permanent reference frame for the pivot. This motivated the design of a dedicated support tower for the TRMS, described in Section 1.5.

1.5 The Twin Rotor MIMO System (TRMS)

1.5.1 Design rationale and evolution from the SATR

The Twin Rotor MIMO System (TRMS) is the final stage of the iterative development of the platform. It extends the SATR by unlocking the yaw axis, thus providing two independent rotational degrees of freedom (pitch and yaw) that interact through the cross-coupling between the two rotors. While the SATR had validated the pitch dynamics and exposed a parasitic coupling between the tail rotor and the pitch axis, the full TRMS allows the cross-coupling effects to be observed and characterised in the configuration for which the system is designed: the tail rotor primarily controls the yaw axis, while the main rotor primarily controls the pitch axis.

The pivot developed for the SATR was made specifically for a single-axis configuration: a single rod mounted in two flanged bearings allowed only one degree of freedom. Improving this architecture to support two degrees of freedom is not a trivial modification: the addition of a second rotation axis can be achieved either through a Cardan joint (limited angular range) or through two independent pivots in series. The TRMS adopts the second option: a horizontal pitch pivot is mounted on a fixed support tower, while a vertical yaw pivot is mounted at the end of the pitch pivot, which enables the beam, IMU, motors, ESCs, and propeller cages to rotate freely about both axes. This separated two-pivot architecture keeps the mechanical simplicity used for the AP and SATR while maintaining the pitch and yaw axes geometrically orthogonal.

Compared to the SATR prototype, the same rotating beam (Bosch 20×20) is reused without any modification, along with several mechanical elements, such as the M6 rod and ball bearings for the yaw pivot, as well as the propeller cages, originally built for the SATR. Several 3D-printed parts are redesigned: the motor link (V3), the ESC connectors, the IMU connector, and the half-rings clamping the rotating beam onto the yaw rod. New mechanical elements and 3D-printed parts are introduced for the TRMS, such as the support tower (Bosch 50×50), carbon fibre rod for the pitch pivot, the U-shape connector linking the two pivots, yaw and pitch locking pins and finally the pitch bearing housing fixed to the support tower. The CAD model is shown in Figure 1.4.

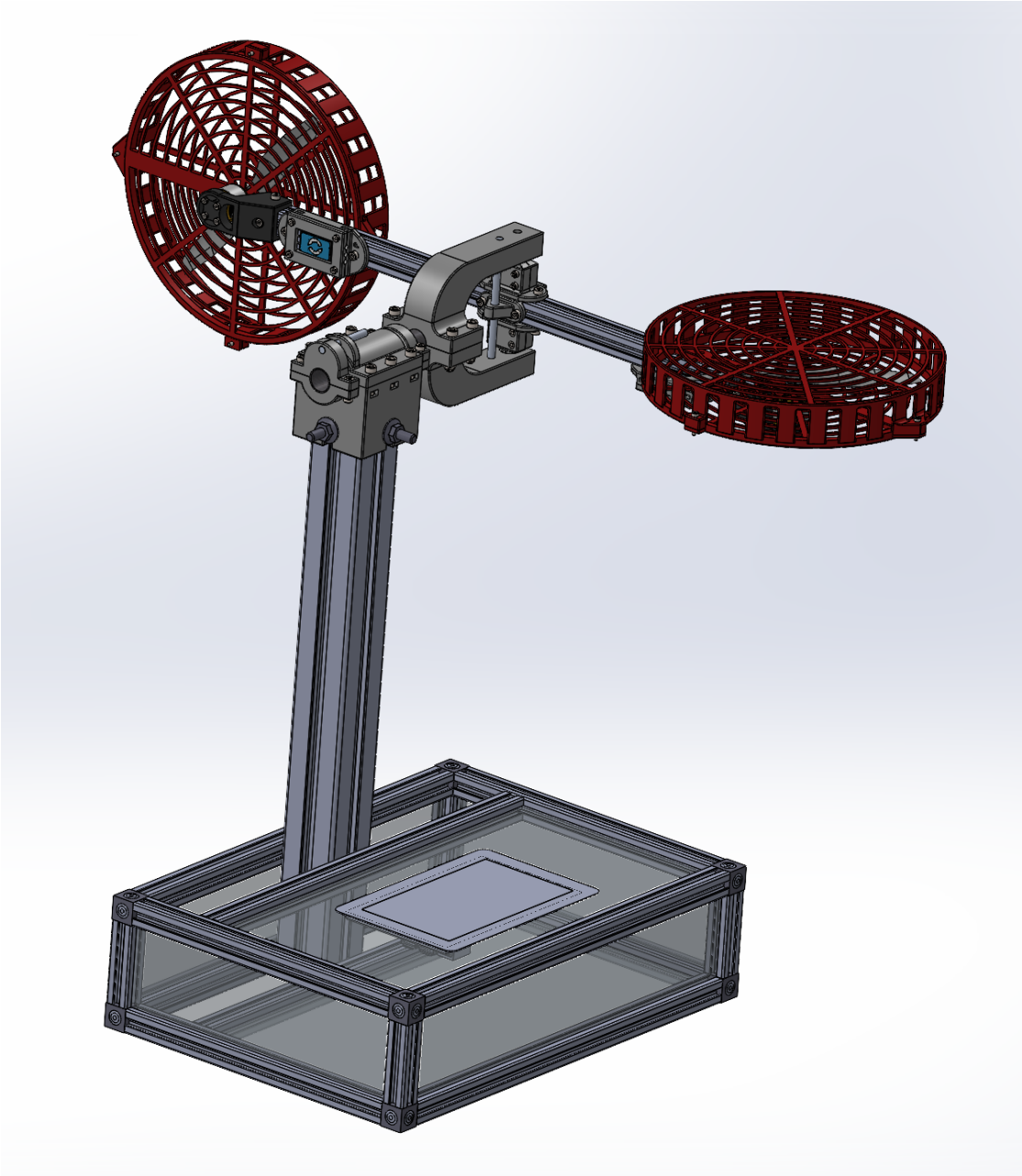


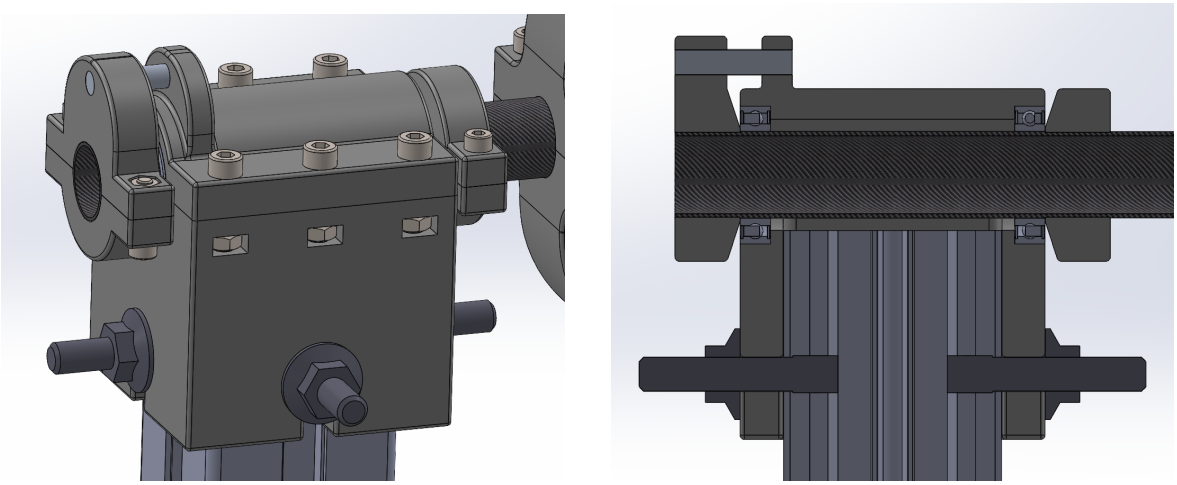
Figure 1.4: CAD model of the TRMS.

1.5.2 Pitch pivot architecture

The two degrees of freedom of the TRMS are achieved through two independent pivots placed in series. The first pivot, attached to the support tower, allows a carbon fibre rod to rotate about a horizontal axis, providing the pitch rotation. The second pivot, supported by a U-shape connector that rotates with the pitch pivot, enables the yaw rotation about a vertical axis when the beam is at the horizontal position.

The pitch pivot is redesigned from the SATR pivot to accommodate the new geometry and withstand the larger structural and inertial loads of the full two-degree-of-freedom

platform. A hollow carbon fibre rod of 20 mm outer diameter passes through two ball bearings (20 mm ID, 32 mm OD) maintained in a two-part 3D-printed housing fixed to the support tower: a lower body that receives the bearings on its half-shells, and an upper body that closes the housing once the rod and bearings are in position, secured by M5 screws. Two 3D-printed retaining rings, clamped onto the carbon rod on each side of the housing, press against the outer face of the bearings and maintain them axially within their housing pockets. The retaining ring on one side also receives the pitch locking pin (described in Section 1.5.6). The choice of a carbon fibre tube was motivated by its high specific stiffness, which limits the bending of the rod under the weight of the rotating subsystem (U-shape, yaw pivot, beam, motors, and cages).



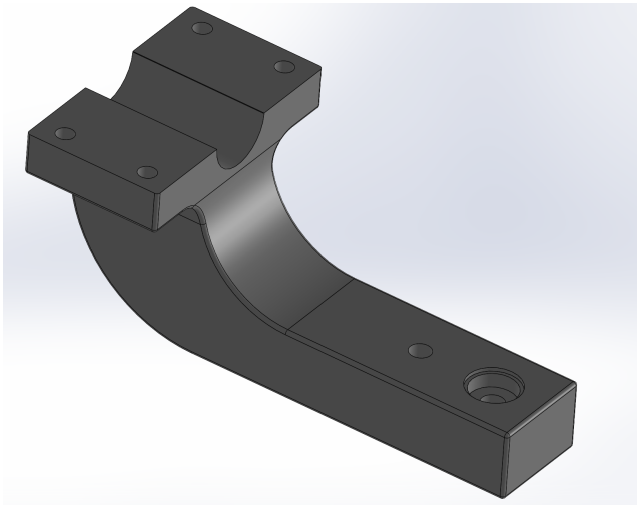
(a) Assembled view, showing the upper and lower bodies secured by M5 screws.

(b) Cross-section through the pitch axis, revealing the two bearings, the carbon rod, and the retaining rings on each side.

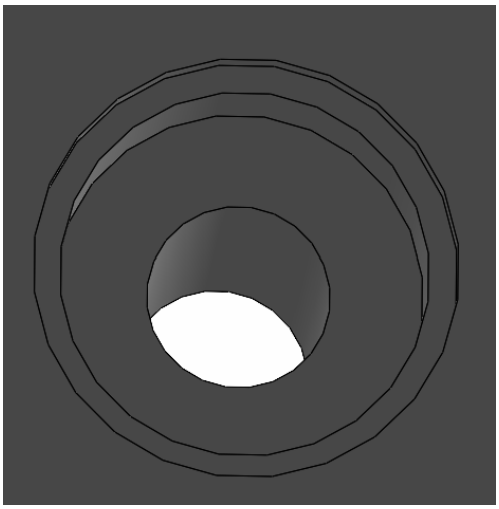
Figure 1.5: Pitch bearing housing: (a) assembled, (b) cross-section.

1.5.3 Yaw pivot architecture

The yaw pivot reuses the mechanical concept validated on the AP and the SATR: an M6 aluminium rod rotates within two flanged ball bearings (6 mm ID, 13 mm OD) housed in two pockets added in the upper and lower branches of the U-shape connector. Each pocket is stepped to receive both the outer race and its flange, fully constraining the bearing axially.



(a) Oblique view of one half of the U-shape connector, showing the stepped pocket on its inner face.



(b) Front view, revealing the three concentric diameters: outer recessed seat for the bearing flange, inner cylindrical seat for the bearing body, and central through-hole for the M6 rod.

Figure 1.6: Stepped cylindrical pocket machined in each half of the U-shape connector to receive a flanged ball bearing.

Each pair of 3D-printed half-rings (upper and lower) is clamped onto the M6 rod with M3 screws, and is positioned to bear axially against the inner race of the corresponding bearing. This contact transmits the rotation between the M6 rod and the bearing inner race, while the outer race remains fixed in the U-shape connector. The rotating beam (Bosch 20×20, 0.5 m, the same as on the SATR) is bolted to these half-rings through M4 screws and matching slot nuts inserted into the rail's profile slots. The resulting kinematic chain is such that the rod, the inner races of the two bearings, the four half-rings, and the rail form a single rigid body rotating about the yaw axis, while the U-shape connector and the outer races of the bearings remain in the non-rotating frame.

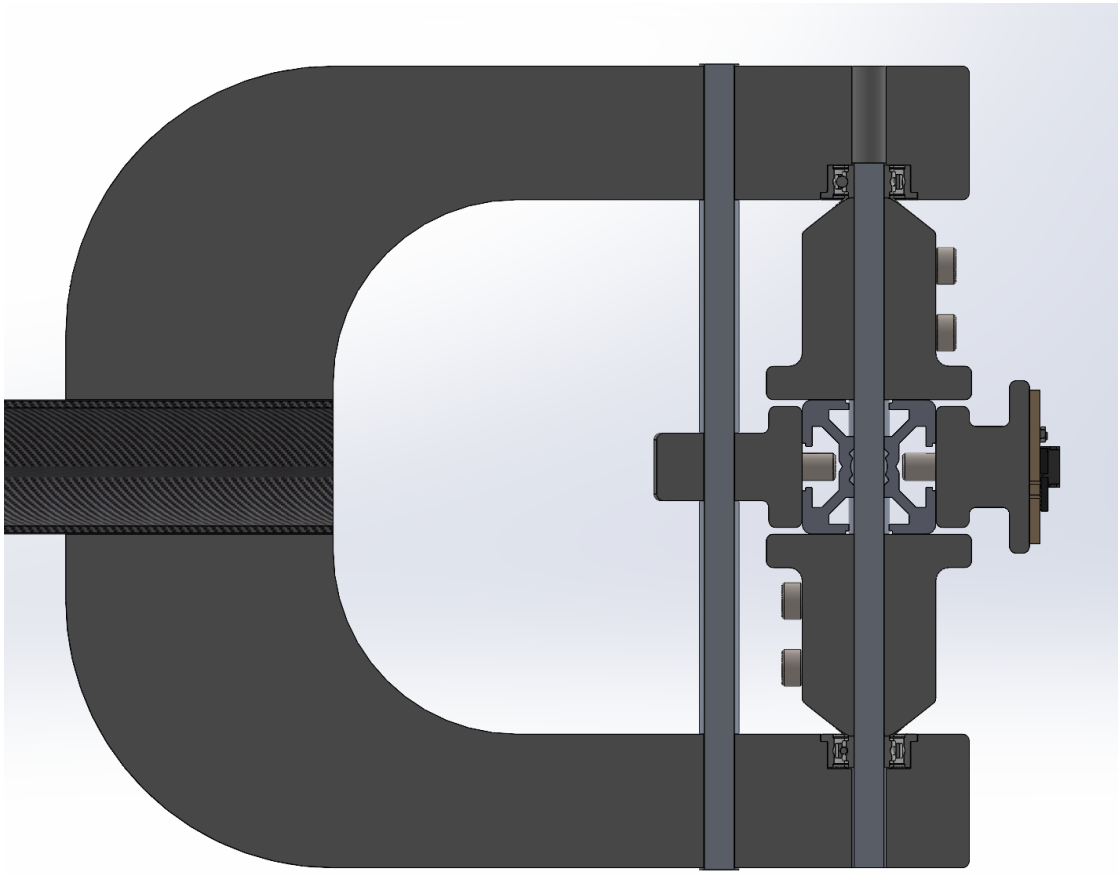


Figure 1.7: Cross-section of the yaw pivot through the M6 rod axis. From top to bottom: the upper bearing housed in the upper branch of the U-shape, the upper pair of half-rings pressing against the inner race of the upper bearing, the rotating beam (Bosch 20×20) clamped between the two pairs of half-rings, the lower pair of half-rings pressing against the inner race of the lower bearing, and the lower bearing housed in the lower branch of the U-shape.

1.5.4 Rotating beam and routing

The rotating beam, whose dimensions were already chosen to be compatible with the TRMS design, is the same one used for the SATR. It consists of a 0.5 m aluminium Bosch 20×20 rail, with an A2212 brushless motor at each end mounted via the V3 motor link, each equipped with an 8-inch CCW propeller enclosed in a V2 cage. The two ESCs are mounted along the rail via the redesigned 3D-printed ESC connectors, and the BNO085 IMU is fixed at the centre of the rail via the IMU connector, redesigned to fit the new TRMS geometry. This co-location minimises the centripetal accelerations sensed by the IMU during yaw rotation and keeps the IMU placement consistent with the previous prototype.

The cables for the two ESCs (PWM signal and ground) and for the IMU (I^2C signal

(SCL/SDA), power and ground) are routed along the rail towards the yaw pivot, then enter the hollow carbon fibre rod to finally reach the base.

As the yaw axis admits a finite angular range enforced by the TRMS geometry, the cable bundle can rotate with the U-shape without wrapping around the yaw rod. The cable length is chosen to be sufficient to ensure the full yaw and pitch ranges without applying any parasitic torque on the rotating subsystem.

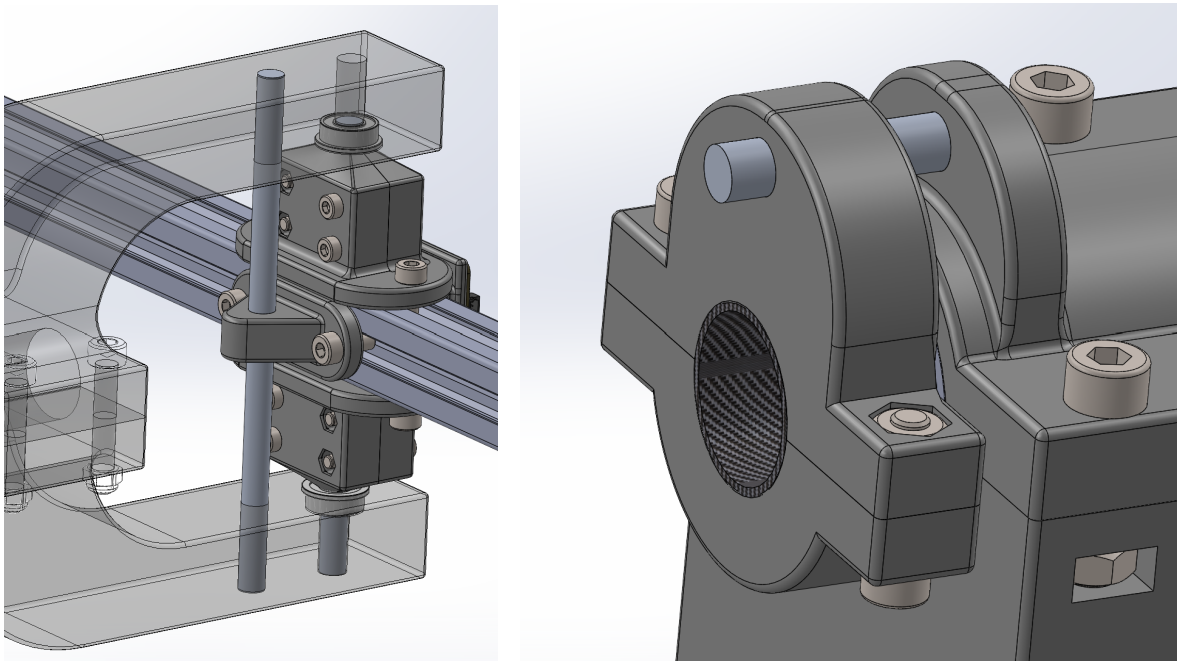
1.5.5 Tower and base

The support tower is a vertical 0.65 m Bosch 50×50 profile, rigidly bolted to the laboratory bench. The pitch bearing housing is mounted at the top of the tower with M8 T-bolts, providing a fixed reference frame for the entire assembly.

The Raspberry Pi, together with the official Raspberry Pi touch display, is housed in a dedicated enclosure built from four laser-cut acrylic panels of various dimensions. The enclosure protects the embedded computer and provides a stable mounting surface for the display, which is used as the local interface to the platform during operation. At the time of writing, the base has not been built yet, and the Raspberry Pi is instead placed on the laboratory bench next to the tower. The design of the base and its integration with the support tower are reported as future work.

1.5.6 Mechanical locking pins

Two axis-locking pin assemblies allow each of the two pivots to be mechanically locked at a discrete reference position. The yaw locking assembly consists of a 3D-printed pin holder, fixed onto the rotating beam (Bosch 20×20) and aligned with two through-holes drilled in the U-shape connector. When a removable M6 pin is inserted through the holder and into the U-shape connector, the rotating beam is immobilised relative to the U-shape and the yaw axis is locked at 0°. The pitch locking assembly follows the same principle: a removable M6 pin is inserted through two aligned holes in the U-shape connector and in the pitch bearing housing on the support tower, locking the carbon fibre rod relative to the tower and therefore freezing the pitch axis at its horizontal reference position. These two locking assemblies serve two purposes. First, they allow the platform to be reduced to a single-axis configuration on demand: inserting the yaw pin enables an aero-pendulum-like configuration about the pitch axis only, while inserting the pitch pin isolates the yaw dynamics. Both configurations are useful for future laboratory sessions in which one degree of freedom is studied in isolation. Second, these locking assemblies allow the platform to be mechanically locked, preventing unintended rotations of the subsystem during transport and storage.



(a) Yaw locking assembly: the M6 pin is inserted through the pin holder on the rotating beam and into the U-shape connector, locking the yaw axis at 0°.

(b) Pitch locking assembly: the M6 pin is inserted through the retaining ring and into the pitch bearing housing, locking the pitch axis at its horizontal reference.

Figure 1.8: Mechanical locking pin assemblies for the two pivots.

1.5.7 Design improvements and current status

Two design improvements were carried out specifically for the TRMS, beyond the structural changes required by the addition of the second rotation axis. First, the motor link was updated to a third revision (V3), shortened compared to the V2 used on the SATR. The reduction in vertical envelope frees up space around the U-shape connector when the beam is close to the horizontal pitch position, and removes a potential interference between the motor link and the U-shape geometry. Second, the ESC connectors were redesigned to improve the assembly procedure. In the SATR version, the M4 mounting screw that fixed the connector to the Bosch 20×20 rail was located inside the ESC cavity, which made the screw inaccessible once the ESC was placed and required removing the ESC to access the mounting screw. In the redesigned version, the M4 mounting screw is relocated outside the ESC cavity, so that the ESC can be installed or removed without having to undo the rail mounting. This is a small but representative design-for-assembly improvement that emerged from the construction experience on the SATR.

At the time of writing, the TRMS is fully assembled mechanically, and the electrical chain (Raspberry Pi, ESCs, BLDC motors, BNO085 IMU, power supply) has been validated: both motors respond correctly to PWM commands, and the IMU returns

valid pitch and yaw measurements through the I^2C interface. The mechanical and electrical design verified on the AP and the SATR has therefore been successfully transferred to the full two-degree-of-freedom platform.

Figure 1.9 shows the assembled TRMS prototype in the laboratory.

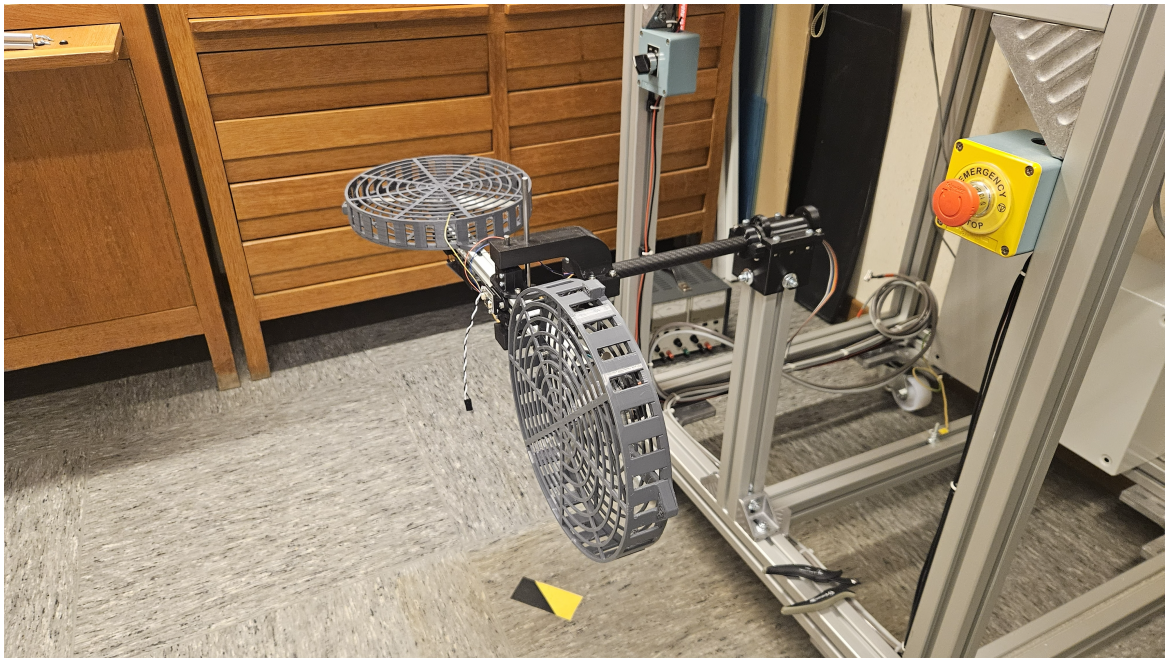


Figure 1.9: Assembled TRMS prototype in the laboratory. The final platform integrates the pitch and yaw pivots, the rotating beam, the two motor–propeller–cage assemblies, the IMU sensor and actuation chain, and the support tower. The complete structure is mounted on the same Bosch 50 × 50 structure used for the SATR, which provides a rigid support and a fixed reference frame for the pivot.

This closed-loop MIMO campaign constitutes the immediate next phase of the project and is developed as future work in the conclusion (Chapter 5). Pitch and yaw orientation data are currently provided by the BNO085 IMU at 200 Hz, which is sufficient for initial hardware validation and short-term control experiments. However, because the selected Game Rotation Vector mode has no absolute yaw reference, yaw sensing based on encoder measurements remains necessary for robust long-duration yaw control. Adding the HEDS-5540 on the yaw axis, which is already supported by the reserved GPIO interface (discussed in Section 2.5), is a planned enhancement that will add an accurate and drift-free yaw measurement and allow the sensor-fusion exercises discussed in Section 2.6.2. With the MIMO controller synthesis and the characterisation of the cross-coupling effects, these extensions constitute the immediate future work for the TRMS platform.

The technical drawings of the main custom TRMS parts are provided in Appendices B–N to support reproduction and future modifications of the platform.

Chapter 2

Electrical Design and Embedded Architecture

The electrical and embedded architecture of the TRMS is developed incrementally across the three prototypes. The same core sensing and actuation principles are maintained throughout the project, but the hardware chain is gradually extended as the platform evolves: the aero-pendulum uses a single motor–ESC channel, while the SATR and TRMS add a second motor–ESC channel for the tail rotor. The embedded code follows the same path, keeping the same basic idea of a Python control loop running on the Raspberry Pi, while extending the control loop with additional sensor readings and actuator commands as the platform evolves.

This chapter presents the electrical architecture and embedded implementation used to command the platform. It first describes the complete electrical system architecture, including the power distribution, sensor interfaces, actuator commands, and communication links. The sensors are then described individually, followed by the actuation chain, the Raspberry Pi controller, the wiring and GPIO allocation, and finally the embedded acquisition and actuation software. The control laws implemented on top of this architecture are introduced separately in Chapter 3.

2.1 System architecture overview

The electrical architecture of the platform is centred around a Raspberry Pi 4 running a control loop at a nominal frequency of 200 Hz. At each iteration, the controller acquires the selected sensor data, either from the HEDS-5540 encoder, from the BNO085 IMU over I^2C, or from a fused estimate depending on the selected mode, computes the control law, and generates PWM commands for the Basic 30A ESCs that drive the

A2212 brushless motors. The same principle is used across the three prototypes, with the number of active motor–ESC channels growing from one on the AP to two on the SATR and TRMS.

The HEDS-5540 quadrature encoder was integrated and validated on the AP and SATR prototypes as an independent angular position sensor. For the final TRMS prototype, the electrical and software architecture reserves the corresponding GPIO inputs for future yaw encoder integration, but the encoder was not mechanically mounted on the physical prototype at the time of writing. Consequently, the final TRMS prototype relies only on the BNO085 IMU measurements for both pitch and yaw.

Figure 2.1 shows the system-level electrical architecture used across the three prototypes. The schematic corresponds to the complete dual-motor configuration intended for the final TRMS and also includes the reserved connection for the HEDS-5540 quadrature encoder. The aero-pendulum and the SATR use the same architecture as subsets of this configuration, with respectively one and two active motor–ESC channels.

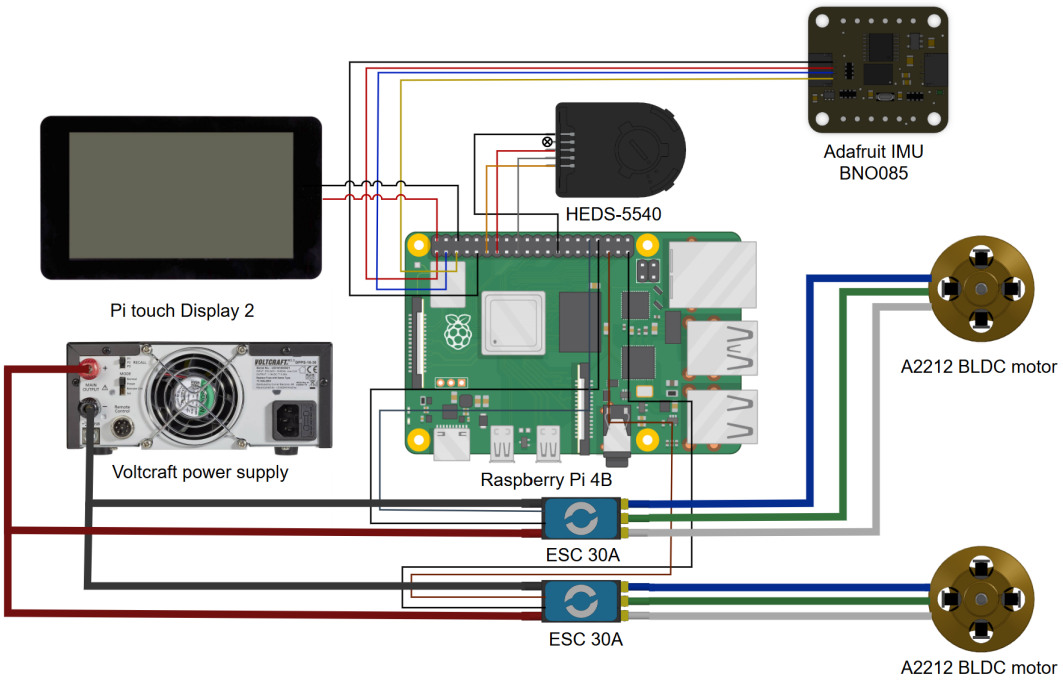


Figure 2.1: System-level wiring architecture of the dual-rotor platform. Thick lines represent the motor power connections, while thin lines represent logic and signal connections. The BNO085 IMU is connected to the Raspberry Pi through I^2C, and the two Basic ESC 30A units receive PWM commands from the Raspberry Pi while being powered by the bench power supply. The HEDS-5540 encoder and its dashed connections represent a reserved extension: the encoder was validated on the AP and SATR prototypes, but was not mechanically integrated into the final TRMS prototype at the time of writing.

The ESCs are powered at 12 V by the VOLTCRAFT DPPS-16-30 bench power supply, while the Raspberry Pi is powered independently from its own USB-C charger. This separation between power and logic levels is intentional to isolate the high-current motor bus from the sensitive logic signals. However, a common ground reference is maintained between the Raspberry Pi and the ESCs to ensure reliable PWM signalling.

The PWM output uses a 200 Hz refresh rate, aligned with the frequency of the embedded control loop. This means that the commanded PWM is recomputed and updated every 5 ms. The ESC itself supports a refresh rate of up to 400 Hz, but the 200 Hz value was kept as a compromise between command responsiveness, implementation simplicity, and reliable behaviour observed during the development of the controller. Since the control loop and the PWM update run at the same nominal frequency, each control iteration produces a new value for the next PWM frame. This introduces a worst-case delay of one PWM period, approximately 5 ms at 200 Hz. This delay is therefore not expected to be a clear limitation in the closed-loop responses observed experimentally.

2.2 Sensors

The platform architecture uses two different sensing principles. The BNO085 IMU provides quaternion-based attitude estimates, while the HEDS-5540 encoder provides relative angular position measurements on the AP and SATR prototypes. On the final TRMS prototype, the encoder interface is kept as a reserved extension for future yaw sensing.

2.2.1 BNO085 inertial measurement unit

The BNO085 IMU introduced in Section 1.2.2 is integrated into the platform as the primary orientation sensor. This section describes its electrical interface, software configuration, calibration procedure, and the conversion from the raw quaternion output to the pitch and yaw angles used by the controller.

The IMU communicates with the Raspberry Pi over I^2C at address `0x4A`, through the `adafruit_bno08x` Python library. At startup, two SH-2 reports are enabled: the *Game Rotation Vector* report, which provides a 6-axis fusion quaternion (accelerometer and gyroscope only, without magnetometer), and the *Gyroscope* report, which provides the raw angular velocity vector. Both reports are configured with an update interval of 5000 µs, corresponding to 200 Hz and matching the control loop frequency. The Game Rotation Vector mode is preferred over the full 9-axis Rotation Vector mode because

of the 100 Hz refresh rate of the magnetometer, which is slower than the control loop frequency. Because the Game Rotation Vector mode excludes the magnetometer, the yaw estimate has no absolute heading reference and is subject to slow gyroscopic drift. This is acceptable for the short bench checks reported here but motivates the planned encoder-based yaw measurement on the TRMS (Section 5.4).

A calibration procedure is performed at startup while the beam is held stationary at its rest position. During this procedure, 50 quaternion samples are collected over 2 s, and the mean pitch and yaw values are stored as offsets. These offsets are subtracted from all subsequent measurements, so that the calibrated angles correspond to a deviation from the rest position rather than from the sensor's internal reference frame.

The quaternion returned by the BNO085 must be converted into the platform's pitch and yaw conventions before being passed to the controller. This is done in software through an `asin`–`atan2` Euler-angle decomposition. For the pitch axis, the platform convention defines positive ψ as the upward motion of the beam from its rest position. Because the IMU is mounted with its local Y-axis pointing in the opposite direction relative to this convention, a sign inversion is required:

$$\psi_{\mathrm{IMU}} = -\left(\mathrm{pitch}_{\mathrm{raw}} - \mathrm{pitch}_{\mathrm{offset}}\right). \tag{2.1}$$

The same sign convention is applied to the pitch angular rate in IMU-only mode:

$$\dot{\psi}_{\mathrm{IMU}} = -\omega_y, \tag{2.2}$$

where ω_y is the gyroscope measurement around the sensor's local Y-axis.

For the yaw axis, the raw yaw angle is similarly corrected by subtracting the yaw offset, and the result is wrapped to the interval $[-180°, 180°]$:

$$\phi_{\mathrm{IMU}} = \mathrm{wrap}(\mathrm{yaw}_{\mathrm{raw}} - \mathrm{yaw}_{\mathrm{offset}}), \qquad \mathrm{wrap} : \mathbb{R} \to [-180°, 180°]. \tag{2.3}$$

2.2.2 HEDS-5540 quadrature encoder

The HEDS-5540 quadrature encoder introduced in Section 1.2.3 is integrated into the platform as an independent angular position sensor for the pitch axis on the AP and the SATR prototypes. It is coupled to the M6 pivot rod via a set screw. This section describes its electrical interface, the software decoding scheme, and the conversion from raw counts to the platform's pitch angle and angular rate. The two quadrature channels (A and B) are connected to GPIO 27 and GPIO 17 of the Raspberry Pi. The HEDS-5540 outputs require external pull-up resistors to provide a defined logic level. 2.7 kΩ resistors pulled up to 3.3 V were soldered between each channel and the supply

rail, which makes the encoder outputs directly compatible with the Raspberry Pi logic levels without the need for an additional voltage divider. The two channels are decoded in software using a $\times 4$ multiplication scheme, leading to an effective resolution of 2000 counts per revolution, equivalent to an angular resolution of $0.18\,^\circ$ per tick.

The quadrature decoding is implemented through a lookup table indexed by the previous and current states of the two channels. Each edge transition on either channel triggers a `pigpio` callback, which updates the position counter. This approach avoids polling and provides reliable edge detection for the angular velocities encountered during the experiments, including fast transients such as the free fall of the beam after release from a displaced position.

The pitch angle is computed from the accumulated position as:

$$\psi_{\text{enc}} = -\frac{\text{position}}{2000} \times 360^\circ \tag{2.4}$$

The negative sign aligns the encoder convention with the platform convention, where positive ψ corresponds to the beam moving upward. The encoder position is reset to zero after the IMU calibration, so that $\psi_{\text{enc}} = 0$ corresponds to the rest position of the beam.

The pitch angular rate $\dot{\psi}_{\text{enc}}$ is obtained by numerical differentiation of the encoder angle:

$$\dot{\psi}_{\text{enc}}(k) = \frac{\psi_{\text{enc}}(k) - \psi_{\text{enc}}(k-1)}{T_s} \tag{2.5}$$

where $T_s = 5\,\text{ms}$ is the sampling period, the same as the control loop period. Because the encoder position is discrete, the raw derivative can exhibit large variations at the control-loop sampling rate. In the implemented controller, the angular rate based on encoder measurements is therefore filtered by a first-order low-pass filter before being used in the derivative term. The filter implementation and its role in the controller are detailed in Section 3.3.4.

On the AP and SATR prototypes, the encoder serves as the primary sensor for pitch closed-loop control at 200 Hz, owing to its drift-free relative measurement and low latency. On the final TRMS prototype, the corresponding GPIO inputs and software interface are kept as a reserved extension for future yaw encoder integration.

2.3 Actuation chain

2.3.1 A2212 brushless motor

The two A2212 1000 KV brushless motors introduced in Section 1.2.5 are mounted at the ends of the rotating beam, each driving an 8-inch CCW propeller. This section presents the electrical characteristics of the motor relevant for its integration into the control loop.

The main electrical parameters of the motor, obtained from the manufacturer's datasheet [6], are summarised in Table 2.1. $K_v = 1000\,\mathrm{rpm\,V^{-1}}$ corresponds to the motor speed constant, which indicates the rotational speed produced per volt when the motor is running at no load. At the selected bench supply voltage of 12 V, the theoretical no-load speed is therefore 12 000 rpm, which is consistent with the trend observed in the datasheet no-load test data (10 500 rpm at 10 V). This voltage is slightly above the nominal 11.1 V value of a 3S LiPo pack, but remains close to the voltage of a fully charged 3S LiPo battery. The motor also accepts a continuous current of up to 13 A per unit, which sets the lower bound for the dual-motor ESC sizing already discussed in Section 1.2.6.

Table 2.1: Main electrical characteristics of the A2212 1000 KV motor, taken from the manufacturer's datasheet [6].

Parameter	**Value**
Velocity constant K_v	$1000\,\mathrm{rpm\,V^{-1}}$
Nominal supply voltage	7.4 V to 11.1 V (2–3 Li-Po)
Winding resistance R	$0.090\,\Omega$
No-load current I_0	0.5 A at 10 V
Maximum current	13 A for 60 s
Maximum power	150 W
Number of poles	14

From the controller's perspective, the motor is not commanded directly: its speed is set indirectly through the PWM command sent to the corresponding ESC (Section 2.3.2). The motor–ESC combination is therefore treated by the controller as a single actuator whose input is a PWM pulse width, expressed in microseconds, and whose output is an aerodynamic thrust applied at the propeller. The static relationship between the two, which is strongly nonlinear and exhibits a forward–reverse asymmetry (Section 2.3.2), is characterised experimentally during the system identification campaign reported in Chapter 3.

2.3.2 Electronic speed controller: Basic ESC 30A

Each motor is driven by a Basic ESC 30A unit (Section 1.2.6), shipped with the BLHeli_S firmware operating in bidirectional mode. The ESC accepts a PWM signal on its signal wire and converts it into three-phase currents for the motor windings. The PWM convention, as specified in the ESC datasheet, is reported in Table 2.2.

Table 2.2: PWM convention used by the BLHeli_S firmware in bidirectional mode.

Pulse width	**Motor state**
1100 µs	Maximum reverse
1475 µs	Deadband lower limit
1500 µs	Neutral (motor stopped)
1525 µs	Deadband upper limit
1900 µs	Maximum forward

According to the datasheet of the ESC, 1500 µs corresponds to the neutral point where the motor stops being driven, 1900 µs corresponds to maximum forward throttle, and 1100 µs corresponds to maximum reverse throttle. The BLHeli_S firmware uses a deadband of ±25 µs around the neutral point, meaning that the PWM values between 1475 µs and 1525 µs do not produce any actuation on the BLDC motor. This deadband is taken into account in the controller design to make sure that the control commands are effective across the full operating range. In the present prototypes, the CCW propellers are mounted such that the ESC reverse direction produces the required lifting force on the arm. Consequently, the controller uses PWM values below neutral during the AP and SATR control experiments. In the following, this range is therefore referred to as the lifting actuation range of the platform, although it corresponds to the reverse direction in the ESC convention. To avoid ambiguity in the following chapters, the PWM offset used in the actuator model is defined as a positive reduction from the neutral PWM command in the lifting direction:

$$\Delta p = 1500\ \mu\text{s} - p_{\text{PWM}}.$$

With this convention, increasing Δp corresponds to increasing lifting command, even though the physical PWM pulse width decreases. The ESC deadband still applies: values $|\Delta p| \leq 25\ \mu$s remain inside the neutral deadband and do not produce effective actuation.

Two software protections are implemented in the embedded control code to prevent electrical damage to the ESC and the motors. A **slew rate limiter** restricts the

maximum change in pulse width to 2 µs per control iteration. At the 200 Hz loop rate, this corresponds to a maximum command rate of 400 µs s^{-1}, which prevents large variations in the PWM command that could cause current spikes in the motor windings and damage the ESC.

A **dwell timer** enforces a minimum hold time of 0.5 s at the neutral pulse width whenever the controller commands a reversal of the motor direction, that is, a transition from the forward band to the reverse band or vice versa. Without this safeguard, rapid variations of the PWM signal were observed to cause the ESC to reset and re-arm, a behaviour likely related to the back-EMF generated by the still-spinning motor, which feeds a transient current back into the ESC power stage and triggers its overcurrent protection. The 0.5 s dwell allows the motor to decelerate through the neutral zone before the opposite-direction drive is applied, and was determined experimentally as the shortest duration that reliably prevents re-arming across the full operating range.

The ESC is armed at startup by holding the neutral pulse width (1500 µs) for 3 s. This arming sequence is required by the BLHeli_S firmware before the ESC will respond to any non-neutral command. When the controller is active, the PWM command is updated at the 200 Hz control-loop frequency. The effective static response of the complete actuation chain, as well as the asymmetry between the two ESC command directions, is characterised experimentally and discussed in Chapter 3.

2.3.3 Bench power supply (VOLTCRAFT DPPS-16-30)

The VOLTCRAFT DPPS-16-30 bench supply, introduced in Section 1.2.8, provides the platform with a regulated DC voltage. The output is set to 12 V, close to the voltage of a fully charged 3S LiPo battery and slightly above the nominal 11.1 V value of the A2212 motors. The 30 A maximum current capacity of the supply provides sufficient margin for the dual-motor configuration, which can draw up to approximately 26 A at full throttle according to the motor datasheet. The supply is connected to the ESC power inputs through XT60 connectors, which were soldered in place of the former connectors, and its voltage and current outputs are monitored during operation to ensure that the motors are not overloaded. This can be achieved thanks to the supply's display or remotely through its USB interface, which enables data logging and real-time monitoring of the supply's output parameters.

2.4 Raspberry Pi 4 controller

The Raspberry Pi 4 Model B (8 GB) introduced in Section 1.2.7 serves as the central embedded controller of the platform. It runs the 64-bit Raspberry Pi OS (Debian-

based) and executes the control loop through a Python program. Remote access to the Raspberry Pi is performed over Wi-Fi via SSH, which allows the code to be edited in real time and the controller to be started without interacting physically with the platform.

To obtain a low-latency and reliable PWM signal, the Raspberry Pi runs the `pigpiod` daemon, a background process used to control the GPIO pins with highly accurate timing. The Python program uses the `pigpio` client library to interface with the daemon and access its services for hardware PWM generation and GPIO callbacks. These two services are described in detail in Section 2.6.1.

2.5 Wiring and GPIO mapping

The complete GPIO allocation of the Raspberry Pi 4 is summarised in Table 2.3. Only four GPIO lines and the I^2C bus are used, leaving the remaining pins available for future extensions, such as one future quadrature encoder for yaw sensing on the TRMS or additional sensor inputs for student projects.

Table 2.3: GPIO allocation on the Raspberry Pi 4.

GPIO	Function	Connected to	Status
GPIO 12	Hardware PWM0	Main rotor ESC	AP/SATR/TRMS
GPIO 13	Hardware PWM1	Tail rotor ESC	AP/SATR/TRMS
GPIO 27	Digital input	Encoder channel A	AP/SATR, reserved on TRMS
GPIO 17	Digital input	Encoder channel B	AP/SATR, reserved on TRMS
GPIO 2	I^2C data (SDA)	BNO085 breakout	AP/SATR/TRMS
GPIO 3	I^2C clock (SCL)	BNO085 breakout	AP/SATR/TRMS

Power and signal cables are routed along the beam and attached with zip ties to prevent interference with the beam dynamics. The I^2C bus operates at 400 kHz instead of the default 100 kHz, to reduce the transaction time of each IMU read within the 5 ms control loop period.

2.6 Embedded software architecture

The control software runs as a single Python process on the Raspberry Pi 4, structured around a timed loop that executes at 200 Hz. The software is organised into four classes — `IMU_BNO085`, `EncoderHEDS5540`, `ESC`, and `PIDController` — orchestrated by a top-level `TRMSController` class that handles initialisation, calibration, the main loop, data logging, and controlled shutdown.

2.6.1 Low-latency GPIO with pigpio

The `pigpio` library [12] provides the interface between the Python control script and the Raspberry Pi hardware. Three services are used concurrently:

Hardware PWM generation on GPIO 12 and GPIO 13 is performed through the `hardware_PWM` primitive of the `pigpio` library. The PWM frequency is set to 200 Hz, corresponding to a frame period of 5 ms. The ESC command is expressed as a PWM value between 1100 µs and 1900 µs. This pulse signal is converted in the Python script into the corresponding duty cycle for the 200 Hz PWM frame. Because the pulse signal generation is handled by the Raspberry Pi hardware PWM peripheral, the Python process only updates the commanded duty cycle and does not need to maintain precise timing for the individual pulse edges.

Edge-triggered callbacks on GPIO 27 and GPIO 17 are used for quadrature decoding of the HEDS-5540 encoder. The `pigpio` daemon monitors the two lines at its internal sampling rate (5 µs by default) and fires a Python callback on every rising or falling edge. The callback function updates the encoder position counter using the lookup table described in Section 2.2.2.

I^2C communication with the BNO085 is performed through the `adafruit_bno08x` library [13], which internally uses the kernel I^2C driver via the `board` and `busio` modules from the Adafruit Blinka compatibility layer.

2.6.2 Real-time control loop

The control loop is the core of the embedded software. At each iteration of the loop, the following operations are performed in sequence: reading the encoder position and computing the pitch angle and angular rate, reading the IMU quaternion and gyroscope, selecting the active sensor source according to the selected mode (encoder-only, IMU-only, or fused), computing the PID controller output, applying the slew rate limiter and dwell timer, sending the resulting pulse width to the ESC, and logging all variables to a CSV file in a folder on the local filesystem.

The timing of the loop is maintained by a `time.sleep(max(0, DT - elapsed))` call at the end of each iteration, where `DT` is the target period of 5 ms and `elapsed` is the duration of the operations performed in the current iteration. This approach does not provide hard real-time guarantees, but empirical observation over runs of 90 s and longer shows that the loop consistently completes within the allotted period, with occasional overruns of less than 1 ms attributed to Python garbage collection and I^2C bus contention.

Three sensor modes are implemented, selectable via a command-line argument passed when starting the control loop: `enc`, `imu`, and `fused`.

The `enc` mode uses the HEDS-5540 encoder as the sole source for both ψ and $\dot{\psi}$. This is the default mode and the one used for all closed-loop validation experiments reported in Chapter 4. It operates at the full 200 Hz loop rate.

The `imu` mode uses the BNO085 as the sole source: ψ is derived from the orientation quaternion and $\dot{\psi}$ from the gyroscope report. Because the IMU may not deliver a new sample at every loop iteration (depending on I^2C timing), the controller detects whether the quaternion has changed since the previous read. If no new data is available, the PID computation is skipped and the previous PWM command is maintained, preventing the integral term from accumulating error on delayed measurements.

The `fused` mode implements a first-order complementary filter that blends the encoder and IMU pitch estimates:

$$\psi_{\text{fused}} = \alpha\, \psi_{\text{enc}} + (1 - \alpha)\, \psi_{\text{IMU}} \tag{2.6}$$

with $\alpha = 0.98$, heavily favouring the drift-free encoder while allowing the IMU to correct long-term encoder offset, which can occur if ticks are missed during very fast transients. The angular rate in this mode is taken from the encoder derivative.

The availability of three sensor modes on the same platform is a deliberate pedagogical feature: future laboratory sessions can ask students to compare the closed-loop performance of each mode, to tune the complementary filter coefficient, or to implement more advanced fusion strategies such as an extended Kalman filter.

The sequence of operations performed at each loop iteration is summarised in Listing 2.1. The complete commented implementation is provided as supporting material in the public GitHub repository, so that it can be reused and extended by other laboratories.

Listing 2.1: Pseudocode of the embedded real-time control loop.

```
# Initialization (once): arm ESC, calibrate IMU, reset encoder
integral = 0

for each control step (every dt = 5 ms):

    # 1/ Read the selected sensor source (enc / imu / fused)
    psi, psi_dot = read_sensor()

    # 2/ Safety check
    if abs(psi) > PSI_MAX:
```

```
11          emergency_stop()
12
13      # 3/ Tracking error
14      error = psi_set_point - psi
15
16      # 4/ Anti-windup: integrate only if the command is not
            saturating
17      if not saturating(error):
18          integral = clip(integral + error * dt, -I_max, I_max)
19
20      # 5/ PID with gravity feedforward (computed on the
            reference)
21      u_p = Kp * error
22      u_i = Ki * integral
23      u_d = -Kd * psi_dot
24      u_g = Kg * sin(psi_off + psi_set_point)
25      u = sat((u_p + u_i + u_d)/90 + u_g)
26
27
28      # 6/ Map to PWM (lifting direction only), apply slew-rate +
            dwell
29
30      pwm = to_pwm(u)
31      send_to_esc(pwm)
32
33      # 7/ Log data and wait until next period
34      log()
35      wait(dt)
```

Chapter 3

Control Study

This chapter introduces the dynamic modelling, the system identification, and the controller synthesis performed on the AP and the SATR, with a discussion about the TRMS. As stated in the introduction of this thesis, the control work is used as a validation tool for the electromechanical design of the platform, rather than as an independent research contribution. The control approach therefore remains deliberately simple by implementing a classical PID feedback, rather than implementing more advanced TRMS control schemes such as the nonlinear cascaded strategy proposed by Belmonte et al. [14].

The chapter is structured in four sections. Section 3.1 derives the dynamic model of the TRMS from a single 2-DoF Euler–Lagrange formulation, from which the AP and SATR cases follow by writing the pitch equation directly in the chosen sensor convention of each prototype. Section 3.2 reports the experimental identification of the dynamic parameters that cannot be obtained analytically, using free-oscillation drop tests on the AP and the SATR. Section 3.3 presents the controller structure, a PID augmented with a gravity feedforward term applied to the reference angle, and details the empirical tuning methodology used to set the gains on the AP and the SATR. Section 3.4 discusses the limitations of the model and of the chosen approach.

Before delving into the details of this chapter, two important choices deserve to be highlighted upfront. First, the motor–ESC–propeller assembly is modelled as a static gain, which is justified by the fact that the actuator dynamics are faster than the mechanical dynamics of the arm, although the margin is moderate. Its quantitative basis and limitations are discussed in Section 3.1.2. Second, the controller gains are not computed analytically by pole placement but tuned empirically on the bench, starting from the proportional term and progressively adding the other terms such as the derivative, integral, and gravity-feedforward. This approach is consistent with the role of the control work in the present thesis, and reflects the difficulty of deriving

analytical gains for a system whose linear parameters are only partially identified.

3.1 Dynamic modelling

3.1.1 Modelling approach and assumptions

The dynamic model of the platform is derived from the Euler–Lagrange approach applied to a system composed of rigid bodies. This approach is regularly used in the literature for the modelling of TRMS platforms [14], [15] because it is particularly adequate for multi-body systems with revolute joints and for the derivation of the equations of motion in generalised coordinates.

The complete TRMS model is derived in Section 3.1.3 through the Euler–Lagrange formalism applied to a rigid-body system with two degrees of freedom. The AP and SATR equations are then obtained in Section 3.1.4 by removing the yaw coordinate (absent due to the mechanical design on those two prototypes) and adjusting the mass parameters specific to the prototypes $\{J_\psi, f_\psi, M_g\}$. This approach avoids the redundancy of writing three separate Lagrangians, while highlighting the structural continuity between the prototypes presented in Chapter 1.

The model is built under the following assumptions.

Rigid bodies. The rotating beam, the U-shape connector, the carbon-fibre rod, and the motor–cage assemblies are modelled as rigid bodies. This is justified by the relatively low rotational speeds and moderate inertial loads involved in the operating regime of the platform.

Aerodynamic losses not modelled explicitly The aerodynamic drag on the rotating structure (beam, U-shape connector, cages) is neglected. The aerodynamic losses related to the propeller cage are not modelled explicitly and appear in practice as a residual dependent on the setpoint that is partially compensated by the gravity feedforward gain (see Section 3.4). This choice is consistent with the desired scope of the thesis and is discussed further in Section 3.4.

Static actuator. The motor–ESC–propeller assembly is represented through an effective static gain. In the equations of motion, its action is written as a generalised torque applied to the arm, while the experimental characterisation is performed through the steady-state pitch response of the AP. This representation avoids the introduction of a thrust variable that is not measured directly on the bench.

Identical model structure across prototypes. The Euler–Lagrange formulation yields a pitch equation whose structural form is common to the three prototypes: the

AP and SATR equations differ from the TRMS equation only in the angular convention used for the gravity term and in the values of the inertia, damping, and gravitational moment specific to each prototype (Section 3.1.4).

The coordinate convention used for the derivation of the full TRMS follows the standard literature [14]: the pitch angle ψ is measured from the horizontal plane and is positive when the main-rotor side of the arm rises above the horizontal. The yaw angle ϕ is measured around the vertical axis. The two generalised coordinates of the full TRMS are therefore $q = (\psi, \phi)^T$. In the present platform, the TRMS is balanced about the pitch axis given its inherent mass distribution, so that $\psi = 0$ corresponds to a passive equilibrium of the unactuated system, with small residual moments due to manufacturing tolerances and to the asymmetric placement of electronic components.

For the AP and the SATR, a different convention is used: the pitch reference is taken at the natural rest position of each prototype, with $\psi_{\text{enc}} = 0$ when the heavier side hangs downwards and ψ_{enc} increasing as the arm rises. This is the convention introduced in Chapter 2, in which the encoder is mechanically reset to the rest position. Unlike the TRMS, the AP lacks a symmetric mass distribution and therefore exhibits a strong restoring moment around its rest position. The SATR, on the other hand, is nearly balanced by design and shows only a small residual restoring moment due to the asymmetric placement of the IMU and the cables (Section 3.2.3). The detailed derivation of how each prototype is written directly in its natural convention, and the resulting form of the gravity term in the reduced models, is detailed in Section 3.1.4.

3.1.2 Actuator model: effective static gain

The actuation chain of the platform is composed of three elements connected in series: the Basic ESC 30A electronic speed controller, the A2212 brushless motor, and the propeller. From the controller's viewpoint, this chain is treated as a single actuator block. In the present work, it is not characterised through a direct thrust measurement, but through an effective static gain relating the PWM offset to the steady-state pitch angle reached by the AP.

Static gain approximation

The actuator block is characterised by the following effective static relation:

$$\psi_{\text{ss}} = K_{\text{eff}}\, \Delta p, \tag{3.1}$$

where $\Delta p = 1500\ \mu\text{s} - p_{\text{PWM}}$ is the signed PWM reduction from neutral, defined positive in the lifting direction and expressed in μs, and K_{eff} is the effective static gain relating

this PWM offset to the steady-state pitch angle of the AP. Because the ESC has a ± 25 μs deadband around neutral, this relation is only meaningful outside the neutral deadband. In practice, the identified static map is used as a local approximation over the lifting range.

This gain is not a direct thrust coefficient of the motor–propeller assembly. It is a coefficient regrouping the complete actuator system in the AP configuration. It therefore includes the motor, ESC, propeller, cage effects, PWM normalisation, and the static equilibrium of the AP arm.

The relation (3.1) is a local approximation. The measured static map is nonlinear over the full lifting range (Section 3.2.4) and is better described by a quadratic law. Equation (3.1) should therefore be interpreted as a local linearisation of this map around the operating range used for closed-loop tuning. This approximation is sufficient for the empirical controller tuning performed in this work, but it should not be interpreted as a general motor performance model.

The internal dynamics of the motor–ESC–propeller assembly are not identified directly in this thesis, since no rotational speed encoder is mounted on the shaft. The actuator is therefore treated as a static element with respect to the dominant mechanical dynamics of the arm. The validity and limitations of this assumption are discussed in Section 3.4.

Lifting and opposing asymmetry. Experimental characterisation of the actuator (Section 3.2.4) reveals that the effective static gain depends on the direction of the PWM offset:

$$K_{\text{eff}}(\Delta p) = \begin{cases} K_{\text{lift}}, & \Delta p \geq 0, \\ K_{\text{opp}}, & \Delta p < 0, \end{cases} \qquad K_{\text{opp}} < K_{\text{lift}}. \tag{3.2}$$

The two coefficients are quantified in Section 3.2.4, where a lifting-to-opposing ratio of approximately 4:1 is reported. This asymmetry is attributed to the aerodynamic profile of the CCW propeller, whose blades are designed for efficient operation in one direction of rotation.

One-sided controller policy. Equation (3.2) describes the open-loop actuator behaviour observed on the bench. The controller used in the closed-loop experiments of Chapter 4, however, does not use the opposing direction: whenever the PID output would correspond to an opposing (downward) thrust, the ESC command is set to the neutral pulse width rather than to the corresponding opposing PWM. The effective

actuator law seen by the closed-loop dynamics is therefore the saturated mapping

$$\tau_{\psi}^{\text{eff}}(\Delta p) = \begin{cases} \kappa\,\Delta p, & \Delta p \geq 0, \\ 0, & \Delta p < 0, \end{cases} \tag{3.3}$$

where κ is an effective gain from PWM to torque in the lifting direction, combining the experimentally identified gain K_{lift} and the steady-state conversion from angle to torque of the AP.

Two arguments motivate this choice. First, the opposing gain K_{opp} would deliver only $\sim 25\,\%$ of the lifting actuation capacity while imposing the ESC reversal constraints (slew-rate limit and 0.5 s neutral dwell, Section 2.3.2), which would in practice penalise the rejection of fast disturbances rather than improve it. Second, the AP and SATR prototypes rest with their heavier side hanging downwards, so that the controller is primarily used to lift the arm above its rest position and to hold it at the commanded setpoint. Downward corrections rely on gravity and aerodynamic damping rather than on active opposing actuation.

The price of this policy is an asymmetric closed-loop response: the rise phase exploits the full K_{lift} actuator authority, while the fall phase is governed by the passive dynamics of the arm (gravity restoring moment and viscous friction). This asymmetry is quantified experimentally in Section 4.2.1.

3.1.3 TRMS 2-DoF Lagrangian model

The full TRMS is a system with two degrees of freedom whose generalised coordinates are the pitch angle ψ and the yaw angle ϕ. The pitch axis is horizontal and supported by the carbon-fibre rod mounted on the support tower, while the yaw axis is vertical when the beam is in its horizontal pitch position, and is supported by the M6 aluminium rod in the U-shape connector (Sections 1.5.2 and 1.5.3). The convention adopted for the TRMS derivation follows the standard literature [14]: $\psi = 0$ corresponds to the arm in the horizontal plane and increases when the main-rotor side rises above the horizontal. The yaw angle ϕ is defined positive in the counter-clockwise sense around the vertical axis when viewed from above.

Kinetic and potential energy. Under the rigid-body assumption, the kinetic energy of the rotating subsystem is the sum of the rotational kinetic energies about the two joint axes:

$$T_{\text{kin}}(t) = \tfrac{1}{2} J_{\psi} \dot{\psi}(t)^2 + \tfrac{1}{2} J_{\phi} \dot{\phi}(t)^2, \tag{3.4}$$

where J_ψ is the moment of inertia of the rotating subsystem (beam, motors, ESCs, propellers, IMU) about the pitch axis carried by the carbon fibre rod, and J_ϕ is the moment of inertia of the same subsystem about the M6 rod that supports the yaw pivot.

The coordinate ϕ is defined as the joint angle of the rotation around the M6 rod, in the convention adopted by Belmonte et al. [14], rather than as the projection of the beam orientation onto a horizontal plane. With this convention, the pitch axis (horizontal in the base frame) and the yaw axis (the M6 rod, fixed in the U-shape connector) remain orthogonal by mechanical construction (Sections 1.5.2 and 1.5.3), independently of the value of ψ. Under the additional assumption that the gyroscopic coupling between $\dot{\psi}$ and $\dot{\phi}$ (arising when the body's angular velocity is projected onto its principal inertia axes) is negligible in the operating regime of the platform, J_ψ and J_ϕ are treated as constant in the simplified model, and no inertial coupling term in $\dot{\psi}\dot{\phi}$ appears.

The potential energy is associated with the small residual gravitational imbalance of the TRMS around the pitch axis. Since the nominal centre of mass is designed to lie on the pitch axis, only a residual gravitational moment M_g^{TRMS} is retained:

$$V\Big(\psi(t)\Big) = -M_g^{\mathrm{TRMS}} \cos\Big(\psi(t)\Big). \tag{3.5}$$

With this convention, the contribution of gravity to the pitch equation is $M_g^{\mathrm{TRMS}} \sin\Big(\psi(t)\Big)$.

Equations of motion. Applying the Euler–Lagrange equations $\frac{d}{dt}\frac{\partial L}{\partial \dot{q}_i} - \frac{\partial L}{\partial q_i} = Q_i$ to the Lagrangian $L = T_{\mathrm{kin}} - V$, with Q_i the generalised force on the coordinate q_i, the equations of motion read:

$$J_\psi\, \ddot{\psi}(t) + f_\psi\, \dot{\psi}(t) + M_g^{\mathrm{TRMS}} \sin\Big(\psi(t)\Big) = \tau_\psi(t), \tag{3.6}$$

$$J_\phi\, \ddot{\phi}(t) + f_\phi\, \dot{\phi}(t) = \tau_\phi(t). \tag{3.7}$$

The terms $f_\psi\dot{\psi}(t)$ and $f_\phi\dot{\phi}(t)$ model the viscous friction in the two pivots, lumping together the bearing friction and the linearised aerodynamic damping. The $\sin\Big(\psi(t)\Big)$ term in the pitch equation reflects the residual gravitational moment arising from the small CoG offset out of the pitch axis; for the TRMS, this term is small and its effect is in practice absorbed by the integral action of the controller.

Coupling between actuators and torques. The two torques τ_ψ and τ_ϕ are generated by the two propellers mounted at the extremities of the beam. The main rotor is positioned at $\mathbf{r}_1 = l_1\, \hat{\mathbf{e}}_{\mathrm{beam}}$ in the body frame, with its thrust $\mathbf{F}_1$ directed perpendicularly

to the beam in the plane spanned by the beam axis and the pitch axis. The generated torque about the pivot is therefore $\mathbf{r}_1 \times \mathbf{F}_1 = F_1 \, l_1 \, \hat{\mathbf{e}}_\psi$, i.e. strictly aligned with the pitch axis in the body frame, independently of ψ. By the same argument, the tail rotor, whose thrust is perpendicular to the beam in the plane spanned by the beam axis and the yaw axis, generates a torque strictly aligned with the yaw axis. The ideal decoupled actuation reads:

$$\begin{pmatrix} \tau_\psi(t) \\ \tau_\phi(t) \end{pmatrix} = \begin{pmatrix} \tau_1(t) \\ \tau_2(t) \end{pmatrix} \qquad \text{in the ideal decoupled configuration.} \tag{3.8}$$

This ideal decoupling is a geometric approximation expressed in the chosen joint coordinates and under the rigid-body and ideal thrust-direction assumptions. In practice, two effects make it imperfect: the parasitic pitch torque produced by the tail rotor at high PWM, already observed on the SATR open-loop tests (Section 1.4.3), and the gyroscopic torque induced by rotor angular momentum during simultaneous pitch and yaw motion. Both are treated here as unmodelled disturbances absorbed by the feedback action of the closed loop.

3.1.4 Prototype-specific instantiation of the pitch equation

The AP and SATR prototypes are modelled using the encoder convention introduced in Chapter 2. In this convention, $\psi_{\text{enc}} = 0$ corresponds to the natural rest position of the arm, with the heavier side hanging downwards, and ψ_{enc} increases as the arm rises. The reduced pitch model is therefore written directly in this convention, rather than obtained via a trigonometric change of variable from the literature TRMS convention.

With this choice of coordinate, the gravitational moment corresponds to that of a physical pendulum around its stable rest configuration. The height of the centre of mass relative to the pivot is proportional to $-\cos(\psi_{\text{enc}})$, such that the potential energy can be written as

$$V(\psi_{\text{enc}}) = -M_g \cos(\psi_{\text{enc}}), \tag{3.9}$$

where M_g is the gravitational moment coefficient. The corresponding generalised gravitational contribution is then

$$\frac{\partial V}{\partial \psi_{\text{enc}}} = M_g \sin(\psi_{\text{enc}}). \tag{3.10}$$

The reduced pitch dynamics of the AP and SATR are consequently written as

$$J_\psi \, \ddot{\psi}_{\text{enc}}(t) + f_\psi \, \dot{\psi}_{\text{enc}}(t) + M_g \, \sin\Big(\psi_{\text{enc}}(t)\Big) = \tau_\psi(t). \tag{3.11}$$

The TRMS follows the literature convention with $\psi_{\text{lit}} = 0$ at the horizontal balanced configuration, meaning that its pitch equation is already given by (3.6) in Section 3.1.3, with M_g^{TRMS} representing the remaining residual moment due to manufacturing tolerances and to the asymmetric placement of the electronic components. The AP, SATR, and TRMS pitch equations therefore share the same single-axis structure, but they are expressed in different angular conventions specific to each prototype and use different numerical parameters.

The AP, with its single motor concentrated at one end, exhibits the largest M_g and the strongest gravitational restoring moment. The SATR has M_g close to zero by symmetric mass distribution, with only the IMU offset producing a small residual moment $M_g^{\text{SATR}} \ll M_g^{\text{AP}}$. The TRMS is designed to be balanced about the pitch axis, with M_g^{TRMS} expected to be of the same order as M_g^{SATR} or even smaller.

3.1.5 Sampling and discrete-time considerations

The plant dynamics described by equations (3.11) and (3.6) are used in the following sections of this chapter as the analytical reference against which the identification campaign of Section 3.2 is interpreted, and against which the structure of the controller of Section 3.3 is motivated. Nevertheless, the controller gains themselves are not computed analytically from the parameters of these equations, but tuned empirically, as discussed in Section 3.3.5.

The controller is implemented on the Raspberry Pi as a discrete-time algorithm running at a sampling frequency of 200 Hz, corresponding to a sampling period $T_s = 5\,\text{ms}$ (Chapter 2). This rate is well above the dominant dynamics of the arm identified in Section 3.2.2, providing an ample margin for the controller to track the system dynamics.

The PWM signal sent to the ESC is generated through the `pigpio` library, which relies on the hardware PWM pins of the Raspberry Pi. The signal produced is a standard PWM signal, with a fixed frame rate of 200 Hz. This frequency was chosen to align with the control-loop frequency, so that each control decision is taken into account in the next loop iteration.

The control-loop timing was characterised empirically on the Raspberry Pi and is reported in Chapter 2. The measurements confirm that the loop reliably completes within the allotted 5 ms period under nominal operating conditions, with a typical

compute budget of approximately 2 ms per iteration. The sampling assumption is therefore satisfied in practice.

The controller is realised in discrete time at the sampling period $T_s = 5\,\text{ms}$. The continuous PID action of Section 3.3 is implemented with elementary discretisation rules consistent with this small sampling period. The integral term uses a rectangular (forward-Euler) rule,

$$I_k = I_{k-1} + e_k\, T_s, \tag{3.12}$$

subject to the conditional update and clamping described in Section 3.3.3. The derivative action is obtained from a backward finite difference of the measured angle,

$$\dot{\psi}_k = \frac{\psi_k - \psi_{k-1}}{T_s}, \tag{3.13}$$

followed by the first-order low-pass filter of Section 3.3.4, which attenuates the quantisation noise amplified by the difference. Because T_s is more than two orders of magnitude shorter than the dominant arm dynamics ($\omega_n/2\pi \approx 0.77\,\text{Hz}$ on the AP, Section 3.2.2), these first-order approximations introduce negligible distortion; more elaborate schemes such as the Tustin transform were therefore not required, and the empirical tuning of Section 3.3.5 further absorbs any residual discretisation effect.

Table 3.1: Main symbols used in the dynamic model of the platform.

Symbol	**Description**	**Unit**
ψ	Pitch angle (generalised coordinate)	rad
ϕ	Yaw angle (generalised coordinate)	rad
ψ_{enc}	Pitch angle in the encoder convention	rad
J_ψ	Pitch moment of inertia of the rotating subsystem	$\text{kg}\,\text{m}^2$
J_ϕ	Yaw moment of inertia of the rotating subsystem	$\text{kg}\,\text{m}^2$
$f_\psi,\ f_\phi$	Viscous friction coefficients (pitch, yaw)	$\text{N}\,\text{m}\,\text{s}\,\text{rad}^{-1}$
M_g	Gravitational moment, $M_g = m_{\text{eq}}\, g\, l_{\text{cm}}$	N m
m_{eq}	Equivalent arm mass	kg
l_{cm}	Centre-of-mass distance from the pivot	m
g	Gravitational acceleration	$\text{m}\,\text{s}^{-2}$
$\tau_\psi,\ \tau_\phi$	Generalised torques about the pitch / yaw axes	N m
Δp	Signed PWM reduction from neutral, positive in the lifting direction	µs
K_{eff}	Effective static actuator gain (PWM $\rightarrow$ angle)	deg/µs
T_s	Control-loop sampling period	s

3.2 System identification

The dynamic model derived in the previous section contains mechanical and aerodynamic parameters whose values cannot be obtained from datasheet values or from first principles alone. The inertia, the gravitational moment, the damping coefficient, and the actuator gain must be identified through experimental tests on the bench. This section reports the identification campaign on the AP and the SATR through drop tests, and on the electrical actuator chain through dedicated PWM step experiments. The full TRMS is not identified independently in this work, and the consequences of this choice are discussed in Section 3.4.

3.2.1 Identification strategy

The mechanical parameters of the AP and SATR pitch dynamics are identified from drop tests, fitted against the nonlinear pendulum equation of motion. For each prototype, the arm is treated as a rigid body of equivalent mass m_{eq} concentrated at the centre of mass, located at a distance l_{cm} from the pivot, both extracted from the SolidWorks CAD model with all materials assigned to each component. With these two quantities known, the nonlinear equation of motion of the arm reduces to a two-parameter model:

$$J\,\ddot{\psi}(t) + b\,\dot{\psi}(t) + m_{\text{eq}}\,g\,l_{\text{cm}}\,\sin\Big(\psi(t)\Big) = 0, \tag{3.14}$$

in which the inertia J and the viscous damping coefficient b are the only remaining unknowns. The identification campaign therefore targets these two parameters directly, by fitting the recorded trajectories against the numerical solution of (3.14) using a dedicated optimiser. The absolute values of J and b are thereby recovered, and the identified J provides an independent cross-validation of the CAD-based inertia retrieved from the SolidWorks model.

The use of m_{eq} and l_{cm} from SolidWorks as independent inputs allows the identification to recover absolute values of J and b from free-response experiments alone, rather than only the ratios $m_{\text{eq}}\,g\,l_{\text{cm}}/J$ and b/J that would otherwise be observable. The trade-off is that the identified J and b depend directly on the accuracy of the CAD model for m_{eq} and l_{cm}. The cross-validation between J_{fit} and J_{CAD} on both prototypes, reported in the next two subsections, indicates that the CAD model is sufficiently faithful to support this approach.

The actuator chain is treated separately, with its static gain identified through dedicated step experiments reported in Section 3.2.4. Its internal time constant is not characterised on the present setup, and a literature-based range is adopted instead.

In the identification, we use the notation J for J_ψ and b for f_ψ for compactness. The gravitational moment M_g is expressed through its defining product $M_g = m_{\text{eq}} g l_{\text{cm}}$.

3.2.2 Drop tests on the AP

The AP provides the first identification configuration. A single V1 propeller cage mounted at the end of the arm with the BLDC motor and propeller inside constitutes an almost ideal pendulum. During the drop tests, the motor is disarmed and the propeller is free to rotate under the airflow generated by the arm's motion, which introduces a moderate aerodynamic damping. The arm is manually pulled to $\psi(0) = \pm 18°$ from its rest position and released without initial velocity. The pitch angle is recorded at 200 Hz via the HEDS-5540 encoder. Five runs are recorded under identical conditions to assess repeatability.

The CAD-based quantities used as inputs to the identification are extracted from the SolidWorks assembly with all materials assigned, and are reported in Table 3.2.

Quantity	Value	Source
m_{eq} (equivalent arm mass)	0.583 kg	SolidWorks
l_{cm} (CoM distance from pivot)	0.327 m	SolidWorks
J_{CAD} (CAD-based inertia at pivot)	0.0776 kg·m^2	SolidWorks

Table 3.2: CAD-based quantities used in the identification of the AP pitch dynamics.

For each run, the recorded encoder trajectory is fitted to the solution of (3.14) using a Nelder–Mead optimiser. The fit minimises the root-mean-square error between the simulated and measured trajectories over the full recorded duration. The five runs yield consistent values:

$$J_{\text{fit}}^{\text{AP}} = 80.7 \pm 1.3 \text{ g} \cdot \text{m}^2, \qquad b_{\text{fit}}^{\text{AP}} = 9.0 \pm 0.9 \text{ mN} \cdot \text{m} \cdot \text{s/rad}. \tag{3.15}$$

From these values, the natural frequency and damping ratio of the AP pitch pendulum follow as $\omega_n = \sqrt{M_g/J_\psi} \approx 4.8$ rad/s (i.e. $\omega_n/2\pi \approx 0.77$ Hz) and $\zeta = b/(2\sqrt{M_g J_\psi}) \approx 0.01$, confirming a very lightly damped second-order behaviour. The identified inertia agrees with the CAD-based value within 4 % ($J_{\text{fit}}^{\text{AP}}/J_{\text{CAD}}^{\text{AP}} = 80.7/77.6 = 1.04$), which provides a strong cross-validation of the SolidWorks mass model. The fit quality varies across the runs, with RMSE values ranging from 0.43° on the best-conditioned release to 3.91° on the noisiest one, the variation being attributable to the manual release. A representative fit is shown in Figure 3.1.

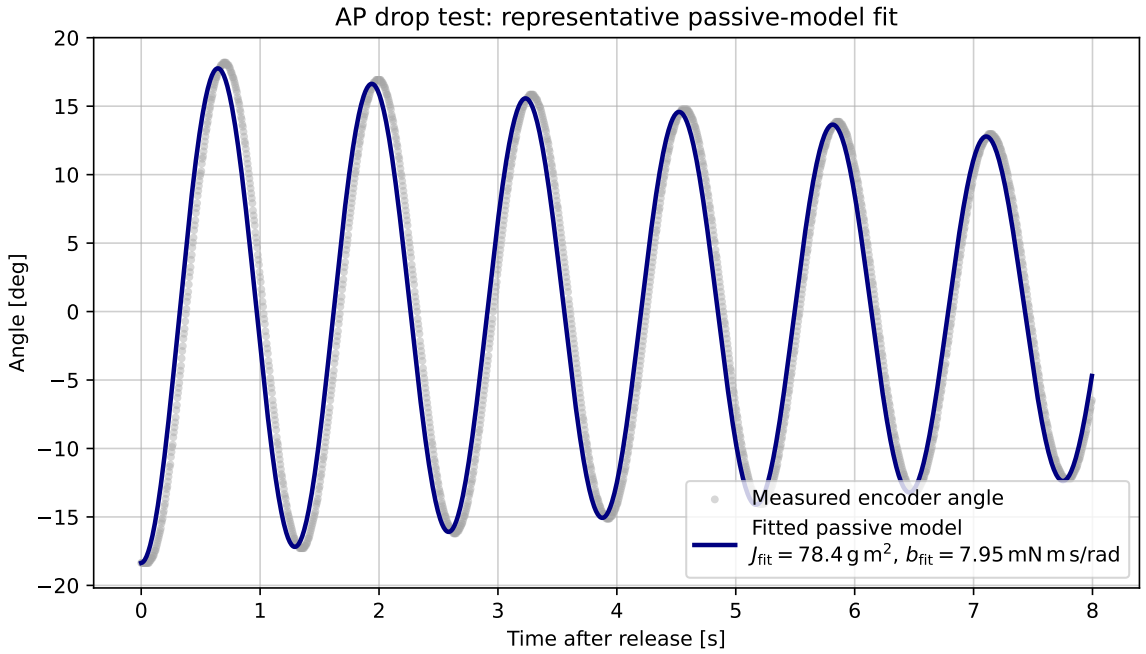


Figure 3.1: Representative AP drop test used for passive-model identification. The measured encoder trajectory is compared with the simulated response obtained using the parameters $J_{\text{fit}}^{\text{AP}} = 78.4\,\text{g}\,\text{m}^2$ and $b_{\text{fit}}^{\text{AP}} = 7.95\,\text{mN}\,\text{m}\,\text{s/rad}$ identified on this specific run. The arm is released from $\psi(0) = -18.36°$, with the motor disarmed and the propeller free to rotate. The fit RMSE is 0.43°.

The identified viscous damping coefficient $b_{\text{fit}}^{\text{AP}} \approx 9$ mN·m·s/rad reflects the combined contribution of pivot friction, drag of the rotating beam structure, and aerodynamic dissipation of the propeller and its cage. At the moderate release amplitudes used here, the linear damping model captures the trajectory faithfully. The validity of the linear damping assumption at larger amplitudes, where aerodynamic drag is expected to become quadratic in angular velocity, is not characterised in the present work and is revisited in Section 3.4.

3.2.3 Drop tests on the SATR

The SATR prototype comes with two cages mounted symmetrically about the pitch axis. This symmetric design reduces almost entirely the gravitational restoring moment, leaving only a small residual moment induced by the asymmetric placement of the IMU and the cables. The centre of mass is computed from the CAD model as the 3D CoG offset in the rotating plane, $l_{\text{cm}} = \sqrt{X_{\text{CoG}}^2 + Y_{\text{CoG}}^2}$, which results in a very short effective lever arm. The CAD-based quantities used in the identification are reported in Table 3.3.

Quantity	Value	Source
m_{eq} (equivalent arm mass)	0.906 kg	SolidWorks
l_{cm} (effective CoM offset from pivot)	5.04 mm	SolidWorks (3D CoG)
J_{CAD} (CAD-based inertia at pivot)	0.0518 kg·m^2	SolidWorks

Table 3.3: CAD-based quantities used in the identification of the SATR pitch dynamics.

Drop tests are realised under the same protocol used for the AP, with the motors disarmed and the propellers free. Five runs are recorded with the arm released from $\psi(0) \approx +87°$, near the horizontal plane. One of these five runs was not used for the identification because the arm was released from a different angle rather than from $+87°$, which was not consistent with the experimental protocol. The four remaining runs are retained. Unlike the AP, the SATR cannot complete a free oscillation: the mechanical layout in the Bosch 50×50 rail structure imposes a hard mechanical stop at $\psi \approx 0°$, against which the arm impacts when it goes from its release angle back toward the equilibrium. The release amplitude of $+87°$ is therefore not a methodological choice but the largest displacement allowed by the structure. Each run consists of a single quarter-period transient between the release angle and the structural end-stop, recorded by the encoder at 200 Hz.

The identification is restricted only to the segment of the trajectory that precedes the structure contact, so that the resulting dynamics of the impact does not affect the parameter estimation. The use of the nonlinear equation (3.14) makes the large release amplitude unproblematic, since no small-angle approximation is involved.

The four exploitable runs yield consistent values:

$$J_{\text{fit}}^{\text{SATR}} = 50.8 \pm 1.8 \text{ g} \cdot \text{m}^2. \tag{3.16}$$

The identified inertia agrees with the CAD-based value within 2 % ($J_{\text{fit}}^{\text{SATR}}/J_{\text{CAD}}^{\text{SATR}} = 50.8/51.8 = 0.98$), which provides a second cross-validation of the SolidWorks methodology, on a prototype with a significantly different geometry and mass distribution from the AP. The viscous damping coefficient, by contrast, is poorly constrained by the single-quarter-period descent observed on the SATR. The fit converges close to zero on three of the four exploitable runs, with the fourth yielding $b \approx 3.6$ mN·m·s/rad. This pattern is consistent with the limited information content of a descent without observable oscillation: the gravity term dominates the dynamics across the recorded interval, leaving little space for the optimiser to constrain b independently from J. An upper bound of $b < 4$ mN·m·s/rad is retained for the SATR, but the absolute value cannot be reported with the same confidence as on the AP. The mean fit RMSE across the four runs is 0.16°, indicating that the linear damped pendulum model captures the

descent of the SATR with high precision. A representative fit is shown in Figure 3.2.

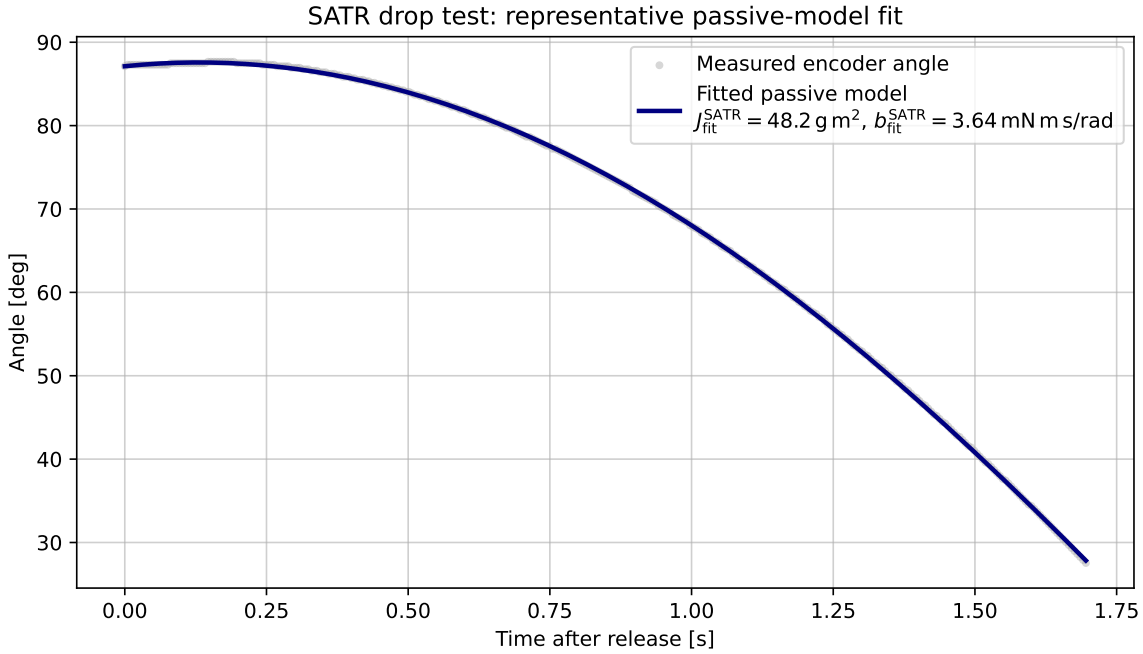


Figure 3.2: Passive drop test on the SATR (run with the highest identified damping). Grey markers correspond to the measured encoder angle, and the solid blue curve corresponds to the simulated passive-model response obtained with the fitted parameters $J_{\text{fit}}^{\text{SATR}}$ and $b_{\text{fit}}^{\text{SATR}}$. The motors were disarmed and the propellers were free during the test. The fit was restricted to $t \leq 1.7\,\text{s}$.

The identification campaign confirms the reliability of the SolidWorks-based mass-property extraction across prototypes of distinct geometry and mass distribution, with J_{fit} agreeing with J_{CAD} within 4 % on the AP and 2 % on the SATR. The absolute value of the viscous damping coefficient is well identified on the AP through the multi-cycle oscillation observed in free response, but remains poorly constrained on the SATR due to the single-quarter-period descent imposed by the mechanical layout. This asymmetry between the two prototypes does not affect the controller synthesis, since the gains of Section 3.3 are tuned empirically rather than computed from the identified parameters, but it is acknowledged as a limitation of the present identification methodology and is revisited in Section 3.4.

3.2.4 Motor, ESC, and propeller actuator

The lifting static gain of the actuator chain is characterised through dedicated PWM-step experiments performed on the AP. A step change in the PWM command is applied while the encoder records the angular response of the arm at 200 Hz. For each lifting step, the resulting steady-state pitch angle reached after the mechanical transient has

settled is plotted against the applied PWM offset. These data points form the static map of Figure 3.3, from which the effective lifting gain K_{lift} is obtained as a local slope relating the PWM input to the equilibrium response of the arm.

This gain is therefore a combined property of the actuator chain and the AP plant in the configuration used for the measurement, rather than a pure motor–ESC characteristic, consistent with the bundled actuator model introduced in Section 3.1.2. Because the map is nonlinear over the lifting range (detailed below), K_{lift} is most accurate as a local value in the neighbourhood of the operating point used for the campaign, and should not be read as a constant valid over the whole range.

Static gain asymmetry. The static map relating the positive lifting PWM offset Δp to the steady-state pitch angle of the AP, identified from the V1-cage step-hold experiments, is shown in Figure 3.3. It is well described by a quadratic law,

$$\psi_{\text{ss}} \propto \Delta p^2,$$

with $R^2 \approx 0.998$. This behaviour is consistent with the fact that propeller thrust scales approximately with the square of the rotational speed, and that the motor–ESC–propeller chain therefore does not behave as a linear actuator over the full PWM range.

The effective gain $\mathrm{d}\psi_{\text{ss}}/\mathrm{d}\Delta p$ is therefore not constant. It increases with the command, from about 0.02 deg/μs near the deadband to about 0.13 deg/μs near maximum lifting. As a representative local value near the closed-loop operating range,

$$K_{\text{lift}} \approx 0.08 \text{ deg}/\mu\text{s}$$

is retained as the nominal lifting gain. This value is a combined property of the actuator chain and of the AP plant in the V1 cage configuration used for the measurement, rather than a pure motor–ESC characteristic. Since the controller gains are tuned empirically rather than computed directly from K_{lift}, the precise value of this nominal gain is not critical to the closed-loop results. The closed-loop experiments of Chapter 4 are nevertheless consistent with this nonlinear actuator behaviour.

The reverse gain K_{opp} is extracted from the same preliminary campaign but under a different excitation protocol from K_{lift}, since no static equilibrium exists in the opposing direction: the AP rests with its heavier side hanging downwards and cannot settle below this position. K_{opp} is reported here as an order-of-magnitude observation rather than as a precise actuator parameter, and is not used by the controller, which operates exclusively in lifting actuation as motivated in Section 3.1.2. Only K_{lift} is therefore retained as the nominal actuator gain for the controller synthesis.

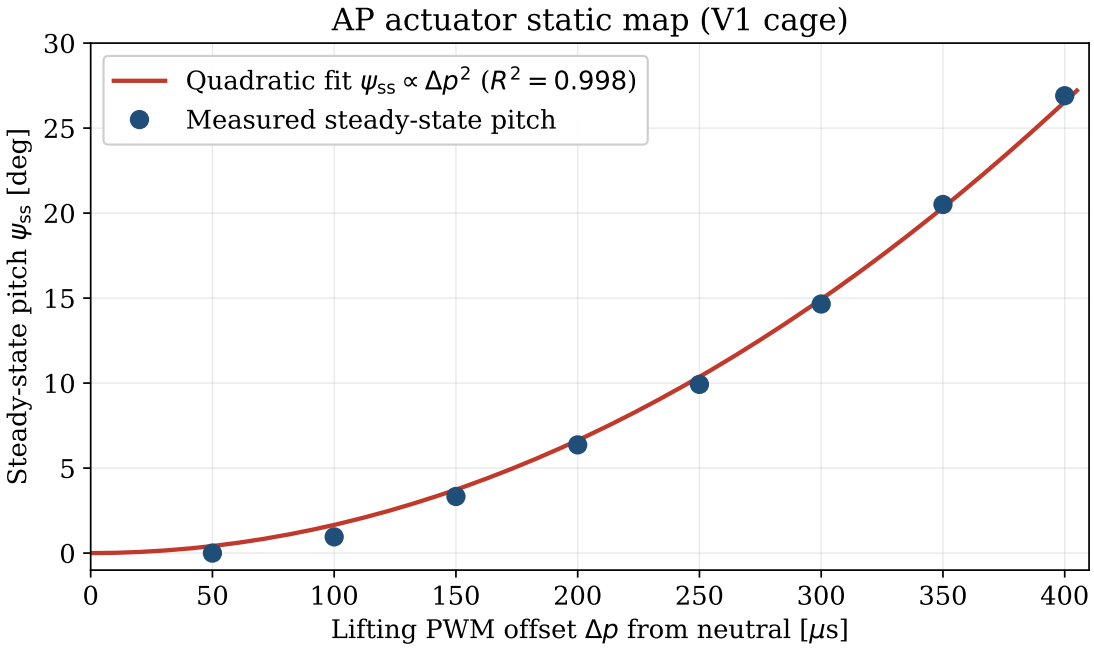


Figure 3.3: Static map of the AP actuator chain in the V1 cage configuration: steady-state pitch angle reached for each positive lifting PWM offset Δp (markers, mean over each PWM hold), together with a quadratic fit $\psi_{ss} \propto \Delta p^2$ giving $R^2 \approx 0.998$. The local slope around the closed-loop operating range gives the nominal gain $K_{\text{lift}} \approx 0.08$ deg/μs.

Actuator time constant. A preliminary step-test identification of the actuator time constant was attempted on the AP early in the project, but the indirect nature of the measurement (arm response rather than direct motor speed) and the sampling rate used in that campaign prevent a reliable separation between the various contributions to the actuator transient. A literature-based range of $\tau_{\text{actuator}} \in [50\,\text{ms}, 200\,\text{ms}]$ is therefore adopted in the present work, with the mechanical contribution from the propeller inertia typically dominating over the electrical contribution from the windings in similar UAV assemblies [16], [17]. The implications for the timescale separation assumption are revisited in Section 3.4.

Software safeguards. Two further parameters appear in the controller code as software-side safeguards against the ESC re-arming behaviour observed during preliminary tests: a PWM slew-rate limiter of 2 µs per iteration and a dwell time of 500 ms at neutral throttle between direction reversals. These are not properties of the actuator chain itself but design choices of the controller implementation, implemented by the controller algorithm described in Section 3.3.3.

3.2.5 Summary of identified parameters

The parameters identified in the present section, grouped by type and by prototype, are gathered in Table 3.4.

Table 3.4: Identified parameters across the AP and SATR prototypes. CAD-derived quantities are extracted from the SolidWorks assembly with all materials assigned. The absolute mechanical parameters J_{fit} and b_{fit} are identified by Nelder–Mead optimisation on the free-drop trajectories. The agreement ratio $J_{\text{fit}}/J_{\text{CAD}}$ provides a cross-validation of the CAD-based mass model. The actuator chain is identified on the AP and assumed shared across prototypes, consistent with the bundled actuator model of Section 3.1.2.

Parameter	**AP**	**SATR**	**Unit**	**Source**
Mechanical, CAD-derived				
m_{eq}	0.583	0.906	kg	SolidWorks
l_{cm}	327	5.04	mm	SolidWorks
J_{CAD}	77.6	51.8	$\text{g}\,\text{m}^2$	SolidWorks
Mechanical, drop-test fit (Nelder–Mead)				
J_{fit}	80.7 ± 1.3	50.8 ± 1.8	$\text{g}\,\text{m}^2$	5 / 4 runs
b_{fit}	9.0 ± 0.9	$< 4^{\dagger}$	$\text{mN}\,\text{m}\,\text{s}\,\text{rad}^{-1}$	5 / 4 runs
Cross-validation (CAD vs. fit)				
$J_{\text{fit}}/J_{\text{CAD}}$	1.04 (+4 %)	0.98 (−2 %)	–	Computed
Actuator chain (estimated on AP, shared)				
K_{lift}	≈ 0.08		deg/µs	PWM step
$K_{\text{opp}}^{\ddagger}$	$\sim 4\times$ lower		–	PWM step (qual.)
τ_{actuator}	50 to 200		ms	Lit. [16], [17]

† Poorly observable on the SATR. ‡ Reported as an observation, not used by the controller.

The TRMS does not appear explicitly in Table 3.4: its mechanical parameters are not identified independently in this work. The controller synthesis of Section 3.3.8 discusses how the AP and SATR results can serve as qualitative starting information for future TRMS control, but no TRMS gains are reported in this thesis. The implications of this choice, and the conditions under which a dedicated identification campaign on the TRMS would become necessary, are discussed in Section 3.4.

3.3 Controller synthesis

This section presents the pitch controller implemented and tuned on the AP and the SATR. The same control philosophy is then discussed as a possible starting point for the future TRMS controller, but the full TRMS is not closed-loop tested in the present work. The controller is a PID acting on the pitch error, with the addition of a gravity

feedforward term computed on the reference angle. The section starts by describing how the controller works and the rationale for each component, then goes into the practical implementation choices (gravity feedforward on the reference, anti-windup, filtering), and ends with the empirical tuning methodology and the gains obtained for each prototype.

3.3.1 Controller structure: PID with gravity feedforward

The pitch controller computes a normalised command $u_\psi(t) \in [-1, +1]$ from the pitch error $e(t) = \psi^*(t) - \psi_{\text{sensor}}(t)$, where ψ^* is defined in the sensor convention. In this convention, $\psi = 0°$ corresponds to the downward vertical rest position of the arm. The gravitational moment is therefore proportional to $\sin(\psi)$, since it becomes zero at the downward equilibrium and reaches its maximum magnitude when the arm is horizontal. The command u_ψ is later mapped to a PWM signal by the actuator interface described in Chapter 2.

The control law implemented in the Python script combines PID feedback with a gravity feedforward term. In the implementation, the proportional, integral and derivative contributions are computed in degrees and degrees per second, then normalised by 90° to obtain a dimensionless command:

$$u_\psi(t) = \text{sat}_{[-u_{\text{lim}},\, u_{\text{lim}}]} \left[\frac{K_p e(t) + K_i I(t) - K_d \dot{\psi}_{\text{sensor}}(t)}{90} + K_g \sin\Big(\psi_{\text{off}} + \psi^*(t)\Big) \right], \quad (3.17)$$

with

$$I(t) = \int_0^t e(\tau)\, \mathrm{d}\tau. \quad (3.18)$$

The physically ideal gravity feedforward term, in the final angle convention, would be proportional to $\sin(\psi^*)$. However, in the experimental AP implementation, the feedforward term was computed with an additional constant angular offset ψ_{off}, as shown in (3.17). This offset came from an earlier software convention used during the first controller tests. It should therefore not be interpreted as a physical rest angle in the final convention, but as an empirical offset present in the implemented controller.

For the SATR, the gravity feedforward gain was set to zero. The feedforward implementation was therefore effectively not used on this prototype, so the angular offset had no influence on the SATR closed-loop behaviour.

The choice of a PID rather than a simpler PD controller is motivated by the fact that holding the arm at an inclined setpoint requires a non-zero steady command to balance the gravitational moment: large on the AP, small but still non-zero on the near-balanced SATR. A PD controller applied to these systems does not produce a zero

steady-state error because this required commanded torque can only be supplied by a P-only term through a residual error $e_{ss} \neq 0$. The gravity feedforward term u_g removes most of this offset by adding an open-loop estimate of the command required to hold the reference position, and the integral term u_i then corrects the residual error caused by model error (imperfect knowledge of K_g, cage aerodynamic losses not modelled, cables). The derivative term u_d provides damping during transients and counteracts the very low mechanical damping ratio identified in Section 3.2.2.

3.3.2 Gravity feedforward on the reference angle

The gravity feedforward term in (3.17) is computed from the reference angle ψ^* rather than from the measured angle ψ_{sensor}. This choice deserves a justification, given that the natural intuition would be to compensate the gravitational torque at the actual position of the arm rather than at the desired one.

A measurement-based feedforward, written as

$$u_g(t) = K_g \sin\Big(\psi_{\text{off}} + \psi_{\text{sensor}}(t)\Big), \tag{3.19}$$

was tested on the AP during the first experiments and produced worse results in closed-loop than the reference-based formulation. Although this formulation is theoretically valid for an ideal model, it turns gravity compensation into an additional feedback path. As a result, any modelling error in K_g or any unmodelled loss in the system (cage aerodynamic losses, actuator delay, saturation) is then directly fed back to the controller. In practice, this made the closed-loop response of the system more oscillatory on the AP.

The reference-based formulation avoids this problem. It has a clear physical interpretation: it is the open-loop command that a known model would apply to hold the arm at the desired position. The PID feedback then only corrects the residual error caused by model imperfections and unmodelled losses.

3.3.3 Anti-windup strategy

The integral term in (3.17) accumulates error over time and can wind up to large values when the command saturates. This is a relevant issue on the present platform because the normalised command is bounded by a software throttle limit, and the PWM signal is itself bounded by the ESC pulse width signal range described in Chapter 2.

The integrator state is updated only when it does not saturate the command even further. Before updating the integrator, the controller evaluates a test command using

the current proportional, derivative, feedforward and previous integral contributions.

$$I_k = \begin{cases} I_{k-1}, & \text{if } u_{\psi,k}^{\text{test}} > u_{\text{lim}} \text{ and } e_k > 0, \\ I_{k-1}, & \text{if } u_{\psi,k}^{\text{test}} < -u_{\text{lim}} \text{ and } e_k < 0, \\ I_{k-1} + e_k\, T_s, & \text{otherwise.} \end{cases} \tag{3.20}$$

The updated integral state is then saturated between $-I_{\max}$ and $+I_{\max}$:

$$I_k \leftarrow \text{sat}_{[-I_{\max},\, I_{\max}]}(I_k)\,, \tag{3.21}$$

where $\text{sat}_{[a,b]}(x)$ corresponds to the saturation function that limits x to the interval $[a, b]$.

These two strategies preserve integral action when it helps reduce the tracking error, but prevent the integrator from accumulating in the wrong direction during saturation. The imposed limitation further guarantees that the integral contribution remains bounded and that recovery after saturation does not become too slow.

3.3.4 Encoder-based derivative filtering

The derivative term u_d in (3.17) requires an estimate of the pitch angular velocity $\dot{\psi}_{\text{sensor}}$. The controller implemented on the AP and the SATR supports several sensor modes: encoder mode, IMU mode, and fused mode. Only the fused mode combines the encoder and IMU measurements. In the encoder mode, the measured angle is the encoder angle and the derivative term is computed from a filtered velocity estimate. In the IMU mode, the measured angle is obtained from the BNO085 quaternion and the angular velocity is taken directly from the gyroscope report, meaning that in this mode, the derivative filter based on the encoder is not used. In the fused mode, the measured angle is obtained through a combination of the encoder and the IMU angles, but the derivative term still uses the same encoder-based velocity estimate.

The filtering described in this subsection therefore concerns the encoder and fused modes. The encoder position is sampled by the control loop at 200 Hz. With the HEDS-5540 encoder used in quadrature mode, the effective resolution is $4 \times 500 = 2000$ counts per revolution, corresponding to an angular resolution of

$$\Delta\psi_{\text{enc}} = \frac{360^\circ}{4 \times 500} = 0.18^\circ. \tag{3.22}$$

The angular velocity is estimated via two consecutive encoder samples:

$$\dot{\psi}_{\text{enc,raw},k} = \frac{\psi_{\text{enc},k} - \psi_{\text{enc},k-1}}{T_s}, \tag{3.23}$$

This estimate is therefore strongly affected by angular resolution. At the sampling period $T_s = 5$ ms, a single encoder count already corresponds to approximately $0.18°/0.005$ s $= 36°/$s. Without filtering, these huge variations would be amplified by the derivative gain and directly added to the motor command.

A first-order low-pass filter is applied to the raw differentiated signal:

$$\dot{\psi}_{\text{enc},k} = \alpha\, \dot{\psi}_{\text{enc,raw},k} + (1-\alpha)\, \dot{\psi}_{\text{enc},k-1}, \qquad \alpha = 0.3. \tag{3.24}$$

This filter was designed to smooth the velocity estimate while preserving the mechanical dynamics of the arm. Using a continuous-time equivalent approximation, the chosen value of α corresponds to a cutoff frequency of the order of 10–15 Hz at $T_s = 5$ ms. This bandwidth remains well above the dominant pitch dynamics identified in Section 3.2.2 ($\omega_n/2\pi \approx 0.77$ Hz on the AP), while staying well below the 100 Hz Nyquist frequency of the sampled loop.

The purpose of the filter is therefore not to filter the measured angle itself, but to make the velocity estimate suitable for derivative feedback. It reduces the high-frequency noise produced by the encoder resolution before it is multiplied by K_d, which limits rapid command oscillations and avoids unnecessary high-frequency PWM variations sent to the ESC and motor.

3.3.5 Empirical tuning methodology

The controller gains are tuned empirically through several experiments rather than computed by an analytical pole-placement procedure. This choice is consistent with the objective of the control study: the controller is used as a validation tool for the electromechanical platform, not as the main research contribution of the thesis. It also highlights the practical limitations of the identified model, in particular the actuator nonlinearities, the lifting/opposing actuation asymmetry, the PWM saturation limits, and the incomplete identification of the SATR damping.

Two classical tuning approaches were considered but not retained. The Ziegler–Nichols method, used in [18] for the aileron actuator, was not adopted because this method is known to produce aggressive gains that are not adequate for the present platform, where the motor–ESC–propeller chain is subject to saturation, slew-rate limits and neutral-dwell constraints, and where large oscillations may quickly drive the arm close to its mechanical limits.

The Broïda approach was also not retained. The AP and SATR pitch dynamics are not well represented by a monotonic first-order response: when released from an initial displacement, the arm behaves as a lightly damped pendulum around its rest

position. Fitting this response with a first-order transfer function would therefore give parameters with no meaningful physical interpretation and controller gains derived from an inappropriate model.

The gains are therefore adjusted incrementally on the real platform. A standard tuning procedure is used: it starts with the proportional gain K_p, increased until the arm shows a clear restoring action without sustained oscillation. The derivative gain K_d is then added to damp the transient response and reduce overshoot. On the AP, the gravity feedforward gain K_g is adjusted next to reduce the steady-state offset caused by the gravitational moment. Finally, the integral gain K_i is introduced to compensate the remaining steady-state error due to imperfect feedforward calibration, friction, cable effects, aerodynamic losses and actuator nonlinearities.

Each gain is increased only if the closed-loop response improves. When a clear performance degradation occurs, such as overshoot for excessive K_p, rapid command oscillations for too large K_d, or recovery issues for aggressive K_i, the gain is reduced to a smaller value. The SATR tuning reused the gains from the AP but was adapted to its more balanced mechanical configuration. In particular, the gravity feedforward gain is set to zero on the SATR because the residual gravitational moment is small enough to be mainly compensated by the integral term.

3.3.6 Tuned gains on the AP

The AP is the first prototype on which the pitch controller is tuned, and the gains obtained on this platform are used as a starting point for the tuning on the SATR. The final gains retained for the AP are gathered in Table 3.5.

Parameter	Value
K_p	0.8
K_i	0.3
K_d	0.5
K_g	0.55 to 1.0
$I_{\max}$	400 deg·s
Max throttle	100 %

Table 3.5: Final tuned gains on the AP.

A first observation is that the gravity feedforward gain K_g is not a single constant value, but varies with the reference angle over the tested range. The best steady-state behaviour is obtained with $K_g \approx 0.55$ for low setpoints close to the vertical downward rest position ($\psi^* \approx 10°$), while larger tested setpoints require values up to approximately

$K_g = 1.0$. The AP prototype could not be tested over a much larger pitch range because the first version of the propeller cage and the BLDC motor assembly were heavy, which limited the reachable setpoints of the platform.

This setpoint dependence should be interpreted with caution. In an ideal gravity feedforward law written in the final encoder convention, the increase of the command with the reference angle would be achieved by the $\sin(\psi^*)$ term, while K_g would remain constant. In the AP implementation, however, the feedforward term included the empirical angular offset ψ_{off} introduced in Section 3.3.1. The identified values of K_g should therefore not be interpreted as a direct physical gravity coefficient.

The observed dependence of K_g on the reference angle indicates that the implemented feedforward law does not fulfil its intended role: it does not behave as a single ideal gravity-compensation coefficient over the tested range. The most likely causes responsible for this behaviour include the empirical angular offset ψ_{off} used in the AP feedforward implementation, aerodynamic losses caused by the propeller cage, cable effects, and actuator nonlinearities. In the present thesis, this dependence is managed empirically by selecting a different value of K_g for each tested setpoint range.

3.3.7 Tuned gains on the SATR

The SATR is tuned starting from the AP gains, which are then adapted iteratively on the bench. The final gains are gathered in Table 3.6.

Parameter	Value
K_p	0.5
K_i	0.3
K_d	1.0
K_g	0
$I_{\max}$	60 deg·s

Table 3.6: Final tuned gains on the SATR.

Three differences from the AP gains deserve comment. The proportional gain K_p is reduced from 0.8 to 0.5, which comes from the fact that the SATR has a more balanced mass distribution with respect to the pitch axis than the AP, meaning that a smaller proportional gain is sufficient to produce the same restoring response, and larger values produce overshoot. The derivative gain is increased from 0.5 to 1.0 to provide additional damping and improve the transient response. The gravity feedforward gain is set to zero here, consistent with the near-balanced configuration discussed in Section 3.2.3: the

gravitational moment is small enough to be compensated by the integral term without the need for an explicit feedforward contribution.

The integral clamp $I_{\max}$ is reduced from $400^\circ \cdot \mathrm{s}$ to $60^\circ \cdot \mathrm{s}$. On the SATR, the residual steady-state error to compensate is small (no gravity feedforward is used; only manufacturing asymmetries contribute), so the integral term only needs to accumulate a small correction. A tighter clamp prevents over-accumulation during transients and improves recovery after manual disturbances, as observed empirically on the bench.

3.3.8 Extension to the TRMS

The closed-loop control of the TRMS was not performed in the present work. The assembly of the TRMS was completed late in the thesis schedule, and safety checks of the mechanical and electrical systems were prioritised over closed-loop tuning. For this reason, no gains are reported for the TRMS in this thesis.

Nevertheless, the AP and SATR prototypes provide a useful starting point for the future control implementation of the TRMS. The AP validates the basic actuation chain and the pitch feedback implementation, while the SATR provides a closer mechanical reference for the TRMS pitch axis because of its more balanced mass distribution and the presence of two motor–cage assemblies. The controller developed on the SATR can therefore serve as an initial reference for the future TRMS controller.

The yaw dynamics of the TRMS require a dedicated treatment. Unlike the AP and the SATR, the TRMS is a coupled two-degree-of-freedom system. Although the simplified model assumes ideal geometric decoupling between the pitch and yaw torques, the real platform is expected to exhibit coupling through parasitic rotor torques, gyroscopic effects, actuator asymmetry and configuration-dependent residual gravitational effects. The yaw loop should therefore not be tuned independently from the pitch loop over the full operating range.

For the TRMS control approach, a duplicated single-axis PID structure could be used as a starting point for the preliminary tuning, but it would not explicitly take into account the coupling between the two axes, the unmodelled coupling effects between the pitch and yaw axes, the parasitic rotor torques, or the gravity effects that depend on the configuration. A more suitable controller for the TRMS would require a complete identification campaign on the platform. An intermediate option, well documented for the TRMS, is to actively decouple the system into two SISO loops through a precompensator before tuning a standard controller on each axis [19]. Ultimately, a multivariable or cascaded strategy similar in spirit to the approach proposed by Belmonte et al. [14], or an optimal state-feedback design such as LQR with integral

action [20] would be more suitable for exploiting the full 2-DoF dynamics of the platform. This remains future work, consistently with the scope of the present thesis.

3.4 Discussion on the control approach

The control work introduced in this chapter is deliberately scoped as a validation tool for the electromechanical design rather than as an independent research contribution. The objective is therefore not to implement an optimal controller from a fully identified model, but to verify that the electromechanical prototypes can be actuated, measured, stabilised and controlled with common feedback techniques. The purpose of this section is to summarise the main limitations of this approach and to identify the aspects that should be addressed in future work.

3.4.1 Dependence on CAD-derived mass properties

The drop-test identification performed on the AP and the SATR provides absolute estimates of the inertia J and viscous damping coefficient b, but this is only possible because the equivalent mass m_{eq} and the centre-of-mass distance from the pivot l_{cm} are taken from the SolidWorks model. Without these quantities based on the SolidWorks model, the free-response trajectory would only reveal the ratios $m_{\mathrm{eq}}gl_{\mathrm{cm}}/J$ and b/J, rather than the individual parameter values.

The good agreement between J_{fit} and J_{CAD} on both the AP and the SATR indicates that the SolidWorks model is sufficiently accurate for the purpose of this work. Nevertheless, the identified mechanical parameters should still be interpreted as estimates rather than as completely independent measurements. Their accuracy depends on adequate material assignment, component masses, and positions of the centre of mass in the CAD assemblies. To reach a higher level of validation, an additional calibration experiment could be performed, for example by adding a known mass at a known distance from the pivot and checking the resulting change in the identified dynamics.

3.4.2 Limitations of the SATR damping identification

The SATR identification provides a reliable estimate of the pitch inertia, as shown by the close values of J_{fit} and J_{CAD}, but the damping coefficient could not be identified as accurately as on the AP. This comes from the mechanical arrangement of the SATR: the arm is limited to a single large-amplitude descent before contact with the mechanical Bosch structure, which prevents the arm from completing a free oscillation. As a result,

the recorded trajectory contains sufficient information to identify the inertia, but not enough to identify the damping coefficient with the same level of confidence. Three out of four runs converge to the optimiser lower bound, which is set to a small positive value to prevent physically unrealistic negative damping. The retained bound on $b_{\text{fit}}^{\text{SATR}}$ should therefore be interpreted as an order-of-magnitude estimate rather than as a precise damping parameter. This limitation does not compromise the controller tuning, because the SATR gains are adjusted empirically on the bench, but it limits the possibility of computing controller gains analytically from the identified model.

3.4.3 Empirical feedforward and actuator limitations

The implemented gravity feedforward on the AP improves the steady-state behaviour of the closed loop, but its implemented gain remains empirical. In an ideal implementation, the feedforward term would be described by a constant gain multiplying $\sin(\psi^*)$, with ψ^* being the reference pitch angle. In the experimental AP implementation, however, the feedforward term includes the empirical angular offset ψ_{off} that comes from an earlier sensor reference convention. The resulting gain K_g therefore cannot be interpreted as a direct coefficient for gravity compensation.

This explains the setpoint dependence of K_g already reported in Section 3.3.6. Beyond the angular offset itself, the static-gain approximation of the actuator introduced in Section 3.1.2 (a local linearisation of the strongly nonlinear PWM-to-thrust relation) also contributes, together with aerodynamic losses caused by the propeller cage and unmodelled cable effects. These contributions are not separated experimentally and are absorbed into the tuned feedforward gain.

The actuator model is also simplified. The actuation chain is represented by a static gain, and the actuator time constant is not identified directly because no rotary encoder is mounted on the motor shaft. The range adopted from the literature is sufficient to justify the static gain approximation as a working assumption, but it does not provide a precise dynamic model of the actuator. Future work should therefore include a direct measurement of the motor speed or a dedicated actuator identification campaign if controller design based on a dynamic model is required.

To make the static-gain assumption explicit, the adopted range $\tau_{\text{actuator}} \in [50, 200]$ ms corresponds to an actuator pole $1/\tau_{\text{actuator}} \in [5, 20]$ rad/s, which is to be compared with the dominant pitch dynamics of the AP, $\omega_n \approx 4.8$ rad/s (Section 3.2.2). The timescale separation therefore ranges from about a factor of four at the fast end of the literature range to roughly 1:1 at the slow end. This confirms that the separation is real but moderate rather than large, and justifies the static-gain model as a working assumption while explaining why the actuator dynamics cannot be neglected with full confidence.

The actuator gains obtained from the AP experiment should be considered as effective gains of the complete AP setup. They are not direct thrust measurements of the motor assembly, but values inferred from the equilibrium response of the complete AP prototype. They are therefore useful for empirical tuning and approximate modelling, but should not be interpreted as pure motor datasheet parameters.

3.4.4 Actuator asymmetry and workspace limitations

The identified actuator behaviour presents strong asymmetry between the lifting and opposing directions. This asymmetry aligns with the use of a propeller designed to operate efficiently only in one direction. In the AP and SATR experiments, this limitation is mitigated by operating mostly in lifting actuation: the controller lifts the arm, while downward corrections can rely partly on gravity and aerodynamic drag.

The current strategy is suitable for the AP and SATR because their useful workspace is naturally centred above the downward rest position. However, it limits the effectiveness of the controller and becomes more important for the full TRMS, where motion in both directions may be needed. Future control implementations should either explicitly take into account the lifting/opposing gain asymmetry or use a different propeller with more symmetric bidirectional thrust characteristics.

3.4.5 Summary

The control approach developed in this chapter validates the main electromechanical functions of the AP and SATR prototypes: sensing, actuation, feedback stabilisation, derivative damping, integral correction, and empirical gravity compensation. The approach is intentionally simple and experimentally tuned, which is consistent with the role of the control work in this thesis.

The main limitations are the dependence of the identification on CAD-derived mass properties, the poor observability of the SATR damping coefficient, the empirical nature of the AP feedforward term, the absence of a directly identified actuator time constant, and the strong lifting/opposing actuation asymmetry. These limitations do not compromise the validation role of the AP and SATR experiments, but they define the boundary between the present classical PID-based approach and the more complete model-based or multivariable control strategy that would be needed for the final TRMS prototype.

The closed-loop control of the complete TRMS remains future work. The AP and SATR results provide useful starting information, but the coupled pitch and yaw

dynamics of the full platform will require a dedicated identification and tuning campaign on the assembled system.

Chapter 4

Experimental Validation

This chapter presents the experimental validation performed on the AP and SATR prototypes. The objective of this chapter is to verify experimentally that the two intermediate prototypes developed in Chapters 1 and 2 can be actuated, measured, stabilised, and controlled. These experiments demonstrate that the main building blocks of the platform are functional and that the control architecture can be implemented on the real system.

The AP validation focuses on the pitch dynamics with a single rotor, the feedback loop based on encoder measurements, and the PID controller with gravity compensation. The SATR validation checks that the same actuation and sensing architecture can still be applied to a more balanced structure, and that the prototype can be stabilised to a desired pitch angle despite the presence of the second rotor and the modified mass distribution.

The complete TRMS prototype was assembled and mechanically and electrically verified, but no closed-loop control was implemented on it in this thesis. Its complete pitch and yaw MIMO validation is therefore left as future work.

4.1 Experimental setup

Each validation experiment is performed with the embedded architecture described in Chapter 2. The control loop runs on the Raspberry Pi at a frequency of 200 Hz, while the ESCs are controlled via PWM signals generated by the `pigpio` library. For the closed-loop experiments on the AP and SATR, the HEDS-5540 encoder is used as the primary sensor for the pitch angle, which provides a stable incremental measurement. The BNO085 IMU measurements are still logged during the experiments, but they are not used for feedback in the results reported below.

For each run, the controller logs the time, encoder angle, IMU angle, angular velocity estimate, setpoint, tracking error, integral state, normalised command, individual control contributions, and PWM command. For the following validation results, the main metrics extracted from these logs are the steady-state angle, steady-state error, maximum reached angle, overshoot, PWM saturation, and finally the qualitative disturbance rejection behaviour.

4.2 Validation on the aero-pendulum

The AP is the first prototype that went through closed-loop validation. Its configuration corresponds intentionally to a worst-case scenario for the actuation chain and for the controller because the motor, propeller, ESC, and V1 cage are all located at the end of the beam, while the pivot is located at the opposite end. This results in a large gravitational moment compared to the later SATR and TRMS configurations, which must be compensated by the controller. This makes the AP an essential test for the actuation chain and for the pitch controller in a worst-case configuration.

The controller used for the AP validation is the PID controller with gravity feedforward, introduced in Section 3.3.1. The gains used during the final AP campaign are:

$$K_p = 0.8, \qquad K_i = 0.3, \qquad K_d = 0.5,$$

with the gravity feedforward gain K_g adjusted according to the tested setpoint, as discussed in Section 3.3.6.

4.2.1 Closed-loop step response and reachable pitch range

The first AP validation test consists of applying fixed pitch setpoints and observing the closed-loop response of the system. Three repeated runs are performed for each of the setpoints 10°, 20°, and 25°, while an additional test is performed at 30° to show the practical limit of the AP configuration. The gravity feedforward gain K_g is adapted based on the tested setpoint, with values of 0.55 at 10°, 0.85 at 20°, and 1.0 at 25° and 30°.

The results are summarised in Table 4.1. The steady-state angle is computed over the last five seconds of each run. For the repeated setpoints, the table reports the mean value over the three runs.

Setpoint	K_g	Final angle	Static error	Max. angle	Comment
10°	0.55	9.95°	0.05°	12.72°	reached
20°	0.85	20.00°	0.00°	22.74°	reached
25°	1.00	24.89°	0.11°	27.42°	reached, near saturation
30°	1.00	26.01°	3.99°	27.90°	not reached

Table 4.1: AP closed-loop step-response summary. The final angle is computed over the last five seconds of each run. The values for 10°, 20°, and 25° are averaged over three repeated runs, while the 30° case corresponds to a single limit test.

The AP reaches the three tested setpoints up to 25° with a very small steady-state error. The final error remains below 0.15° in the three repeated setpoint groups, which confirms the effectiveness of the combined gravity feedforward and integral action. Thanks to the repeated runs, the results show that the response is consistent across runs: the standard deviation of the final steady-state angle remains below 0.05° for all repeated setpoints.

The 30° test reveals the practical limitation of the AP prototype. Although the controller raises the arm upwards properly, the final angle stabilises around 26°, meaning that the setpoint is not reached. This result is not considered as a failure of the feedback control structure, but rather as a limitation of the performance of the actuation chain in the V1 configuration. The PWM command reaches its minimum value corresponding to the maximum lifting actuation, and the controller remains close to saturation during most of the run. This ceiling is consistent with the open-loop static characterisation of Section 3.2.4. The lifting PWM offset is limited to about 375 µs (from the neutral value of 1500 µs minus the signal-deadband of 25 µs, down to the maximum-lifting command at 1100 µs), and the measured steady-state pitch of the AP reaches only about 27° at this maximum value in the V1 configuration. The 30° setpoint therefore exceeds the maximum lifting capacity of the platform (the command saturates at the PWM floor) rather than indicating a failure of the feedback structure. The heavy V1 propeller cage and the BLDC motor assembly thus impose a practical limit on the reachable pitch angle of the AP, approximately 25° with small steady-state error, with an absolute ceiling near 27° at maximum lifting.

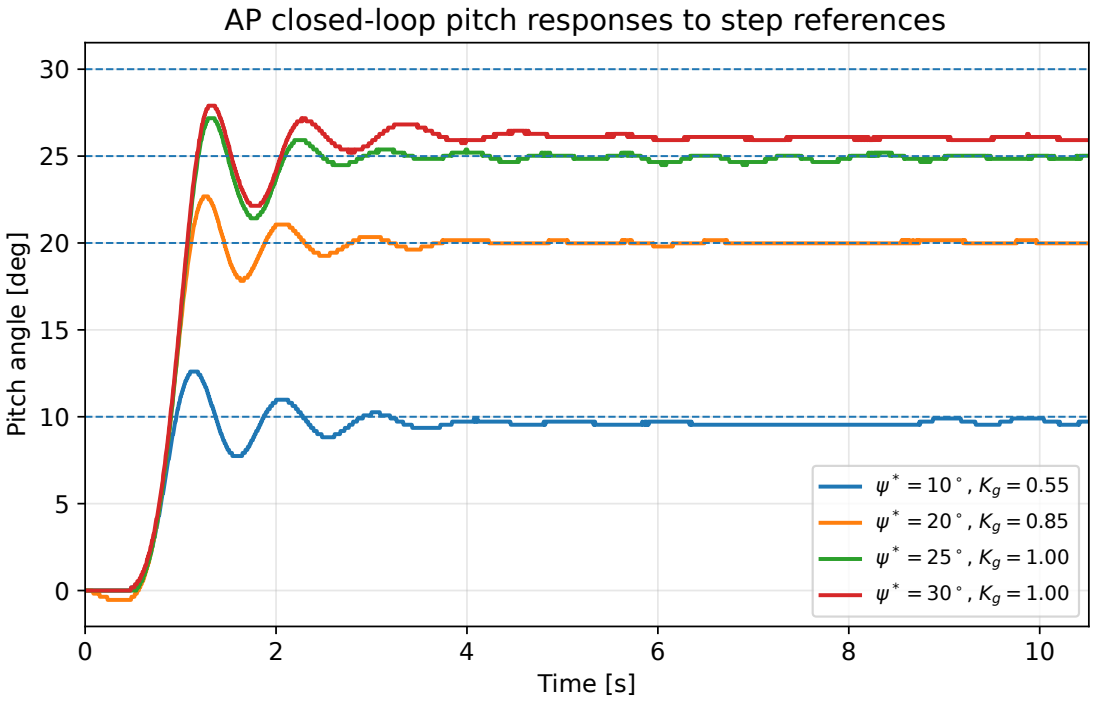


Figure 4.1: AP closed-loop step responses for the tested pitch setpoints. The responses at 10°, 20°, and 25° reach the commanded setpoint, whereas the 30° test reveals the actuator limit of the AP configuration.

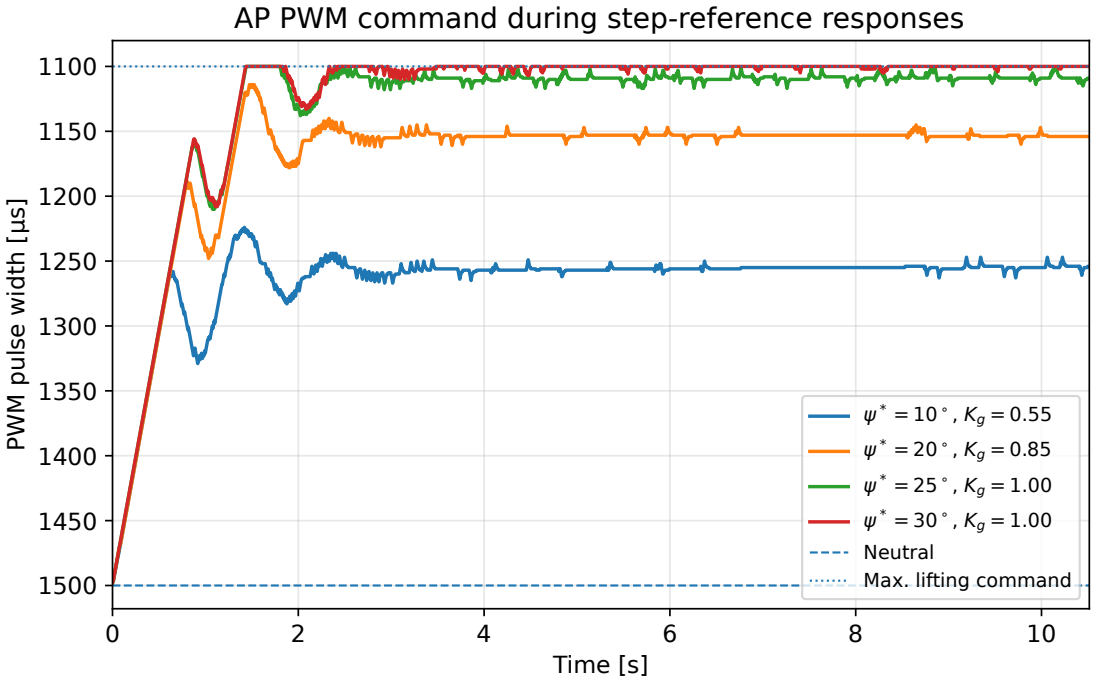


Figure 4.2: PWM command during the AP step-response tests. The 30° run reaches the maximum lifting actuation limit, confirming that the corresponding steady-state error is caused by saturation of the actuation chain.

4.2.2 Disturbance rejection

A disturbance rejection test is performed at a setpoint of 20°. The same controller structure is used, with the derivative gain slightly increased to $K_d = 0.7$ for this disturbance-rejection test. During the test, the arm is manually displaced away from its equilibrium position several times, and the controller manages to reach the desired angle again after each perturbation.

Before the manual perturbations, the AP manages to stabilise around the setpoint with a small steady-state error. Over the interval from 4 to 8 s, the mean pitch angle is approximately 20.00° with a standard deviation of only 0.06°. During the perturbations, the measured angle reaches a minimum of approximately 10.6° and a maximum of approximately 27.7°, corresponding to deviations of roughly −9.4° and +7.7° with respect to the setpoint. After the perturbations, the arm is brought back toward the commanded position by the controller.

This test confirms that the controller does not only stabilise the AP at a fixed setpoint, but is also able to recover from external disturbances within the tested operating range. The recovery is asymmetric because the controller relies on lifting actuation to raise the arm upwards, while downward corrections depend only on gravity and passive damping because the controller does not use opposing actuation. This behaviour is consistent with the one-sided actuation strategy introduced in Section 3.1.2.

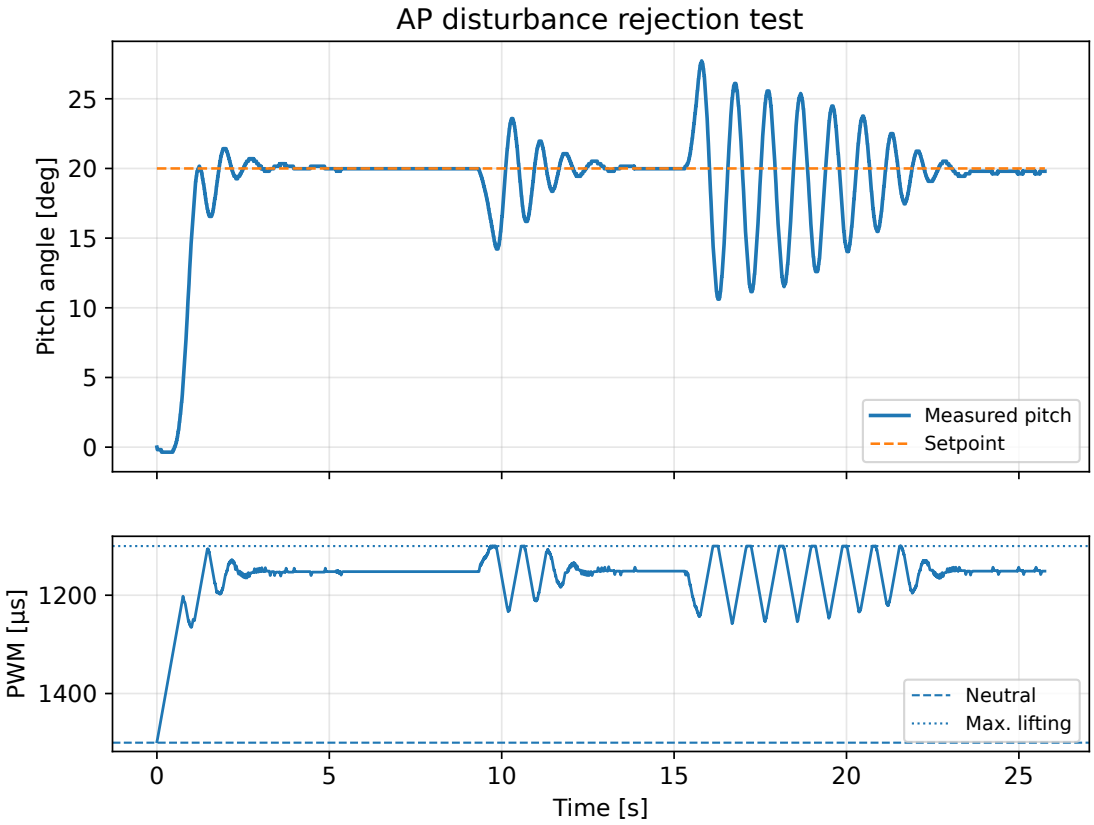


Figure 4.3: AP disturbance rejection test at a 20° setpoint. The arm is manually perturbed several times and returns toward the commanded pitch angle after each perturbation.

4.2.3 Exploratory sinusoidal tracking

Additional tests are carried out with sinusoidal pitch tracking of amplitude 5° around mean angles of 10° and 20°. These tests are not used as a validation criterion for the control architecture, given that the AP configuration is intentionally unfavourable for tracking due to its unidirectional actuation and large gravitational moment. However, these tests provide qualitative information about the tracking limitations of the current control strategy.

The sinusoidal tests provide qualitative insight into the tracking limitations of the AP. The measured response follows the reference qualitatively but with a reduced amplitude and a phase lag that grow with frequency, which is the expected signature of a system tracking a reference close to the limit of its bandwidth. At the frequencies tested, the reference varies too fast for the AP with its unfavourable configuration, namely one-sided actuation and a large gravitational moment. The system cannot follow these fast variations, but slower references certainly would be tracked more closely. These tests are therefore interpreted as an exploratory observation of the tracking

limitations rather than as a quantitative bandwidth identification or a validation of trajectory-tracking performance, consistent with the worst-case role assigned to the AP.

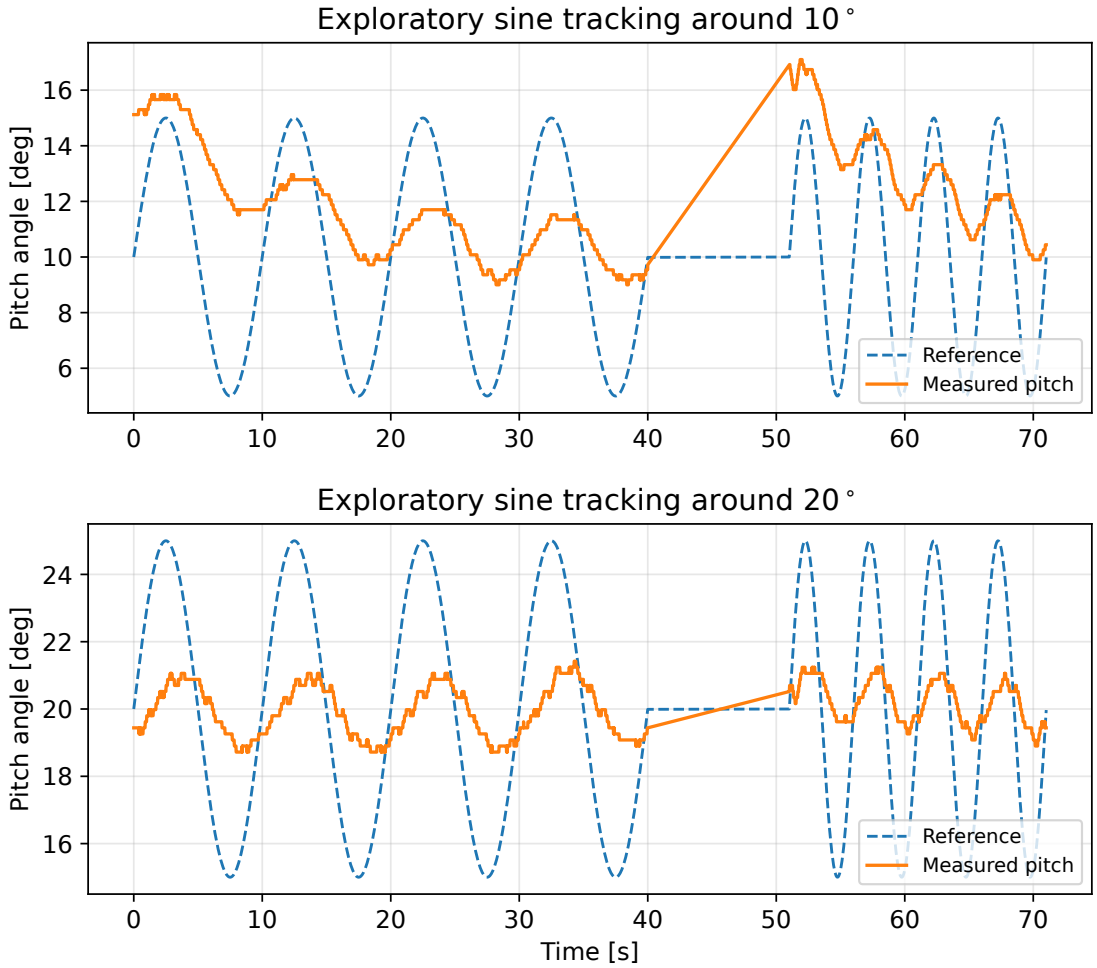


Figure 4.4: Exploratory AP sinusoidal tracking test. The measured response shows reduced amplitude and visible phase lag with respect to the reference, illustrating the tracking limitations of the AP configuration.

4.2.4 AP validation summary

The AP validation confirms the correct operation of the main electromechanical building blocks of the platform. The closed-loop controller based on the HEDS-5540 encoder runs at the intended sampling frequency, the ESC and BLDC motor provide sufficient actuation authority to stabilise the unbalanced arm up to approximately 25°, and the PID controller with gravity feedforward achieves small steady-state errors over the tested range.

The AP also reveals the first practical limitation of the design. The 30° setpoint cannot be reached in the V1 cage configuration because the actuation chain saturates before reaching the desired setpoint. This limitation is consistent with the mechanical

lessons learned from the AP in Chapter 1: the V1 cage is heavy and aerodynamically penalising, motivating the more compact V2 cage used on the SATR and TRMS prototypes.

4.3 Validation on the single-axis twin-rotor prototype

The SATR is used as the second closed-loop validation step. In comparison with the AP, the SATR is designed with a more balanced mass distribution around the pitch axis and includes the two motor–cage assemblies that are later reused on the TRMS. The purpose of this validation is therefore to verify that the same actuation, sensing, and PID architecture remains operational on a dual-rotor system, while also observing the coupling effects caused by the tail rotor.

The controller used in the SATR validation is the same PID controller introduced in Section 3.3.1, with the gains reported in Section 3.3.7:

$$K_p = 0.5, \qquad K_i = 0.3, \qquad K_d = 1.0, \qquad K_g = 0.$$

Unlike on the AP, no gravity feedforward is used. The small remaining gravitational imbalance of the SATR is handled by the integral term.

4.3.1 Closed-loop pitch step response

The first SATR validation test consists of imposing fixed pitch setpoints of 20°, 40°, 60°, and 80°. The yaw axis stays mechanically locked during these tests, and the control loop uses the HEDS-5540 encoder for pitch feedback. The main rotor is used to raise the arm about the pitch axis, while the tail rotor is kept inactive during these closed-loop tests.

The results are summarised in Table 4.2. The steady-state angle is computed over the last five seconds of each run. For the 80° setpoint, two repeated runs are averaged.

Setpoint	Final angle	Static error	Max. angle	Mean steady PWM
20°	20.04°	−0.04°	22.86°	1389 µs
40°	39.96°	0.04°	44.64°	1384 µs
60°	60.00°	0.00°	64.08°	1380 µs
80°	80.01°	−0.01°	81.90°	1381 µs

Table 4.2: SATR closed-loop pitch step-response summary. The final angle is computed over the last five seconds of each run.

The SATR manages to reach all tested setpoints up to 80° with negligible steady-state error. This confirms that the pitch controller remains valid for the current configuration and that a gravity feedforward term is no longer required for the SATR configuration. The steady-state PWM command stays approximately in the same range for all tested setpoints, around 1380 µs–1390 µs, which confirms that the SATR is much more balanced than the AP prototype. The controller therefore mainly compensates residual imbalance, friction, and aerodynamic losses rather than a large gravity torque as on the AP.

The transient response remains stable across the tested range, and a qualitative comparison with the AP is instructive. The AP step responses (Figure 4.1) exhibit features which are characteristic of a lightly damped second-order system, consistent with the very low mechanical damping of the AP (Section 3.2.2). The SATR responses (Figure 4.5), by contrast, rise more smoothly toward the setpoint, closer to a well-damped second-order behaviour, with only a moderate overshoot at the intermediate setpoints (a maximum angle of 44.64° for a 40° setpoint and 64.08° for a 60° setpoint). This change in closed-loop signature illustrates how the mechanical design of the SATR, with its balanced mass distribution, together with the associated re-tuning of the gains, reshapes the dynamic response of the platform. The response at 80° remains stable and reaches the setpoint without saturation, confirming that the achievable pitch range of the SATR is larger than that of the AP.

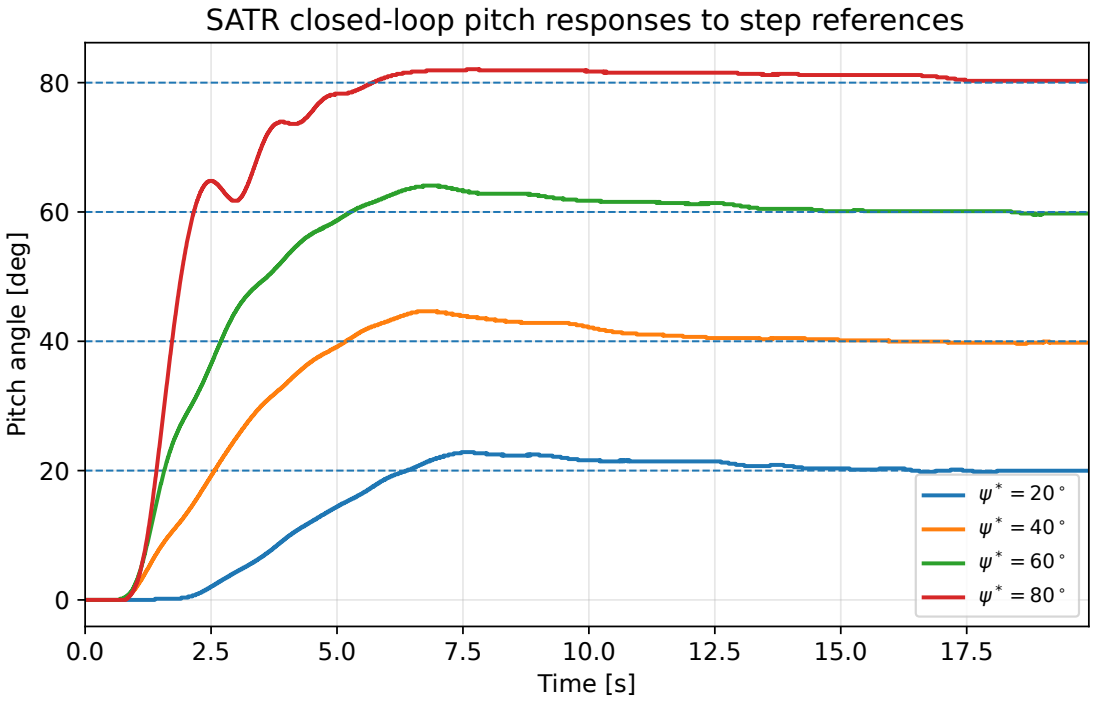


Figure 4.5: SATR closed-loop pitch step responses for the tested setpoints. The controller reaches all commanded angles with negligible steady-state error and without gravity feedforward.

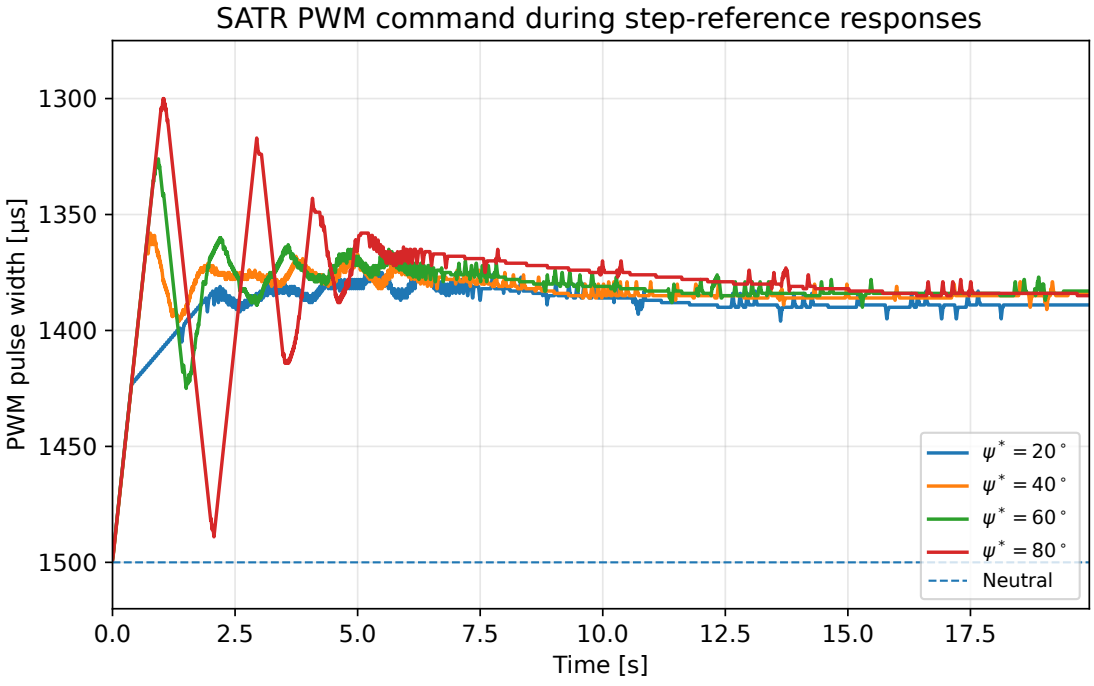


Figure 4.6: PWM command during the SATR pitch step-response tests. The steady-state PWM remains in a similar range for all tested setpoints, reflecting the more balanced mass distribution of the SATR compared with the AP.

4.3.2 Disturbance rejection

A longer run at a 40° setpoint is used to evaluate the disturbance rejection capability of the SATR control loop. During this test, the arm is manually moved away from its target position multiple times, and the controller response is recorded.

The first part of the run is the same as the 40° step response presented in the previous section, with the arm stabilised around the setpoint from approximately 0 to 20 s. After this stabilisation interval, the arm is manually perturbed several times: a first small downward perturbation is applied around 25 s, which shows good recovery of the controller. Then, around 30 s, a larger upward perturbation is applied, which also demonstrates a slow but consistent recovery of the controller towards the setpoint. Finally, a large downward perturbation is applied around 45 s, which shows the controller struggling to recover with an abrupt spike reaching approximately 84.6°, then an abrupt drop to approximately 22.0°, followed by a slow recovery towards the setpoint.

This test confirms that the SATR pitch loop is able to reach fixed setpoints and recover from small disturbances, but it also exhibits the limits of recovery from larger disturbances. As on the AP, the response remains asymmetric because the controller primarily uses the lifting direction and relies on passive gravitational return for downward corrections. Nevertheless, recovery is still achieved with the tested disturbances, even if the response becomes slower and more oscillatory for larger perturbations.

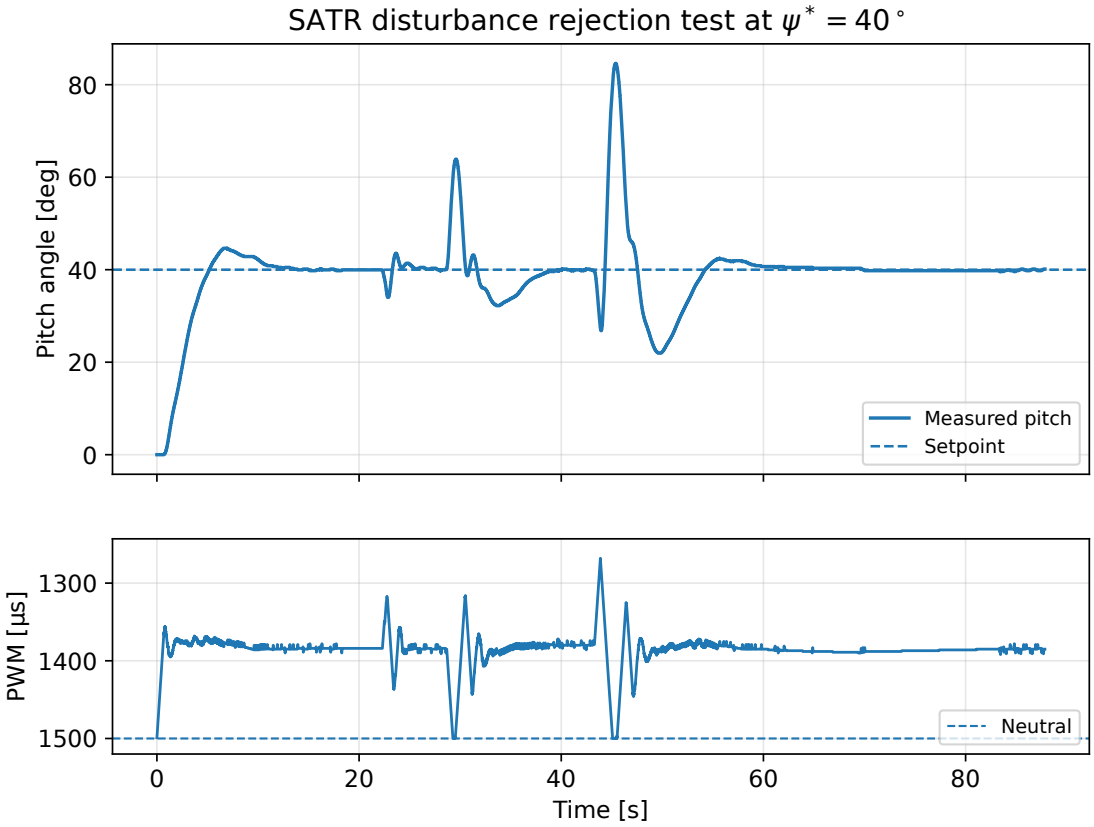


Figure 4.7: SATR disturbance rejection test at a 40° setpoint. The arm is manually perturbed and the controller returns the pitch angle towards the commanded position.

4.3.3 Open-loop tail-rotor coupling

The final SATR validation test was performed to investigate the effect of the tail rotor on the pitch axis. In an ideal SATR geometry, the tail rotor should not affect the pitch dynamics because its thrust direction is meant to produce torque only about the yaw axis. Nevertheless, in practice, the cage geometry, airflow interaction, mechanical misalignments, and small mounting inaccuracies of the motors can introduce a parasitic pitch contribution from the tail rotor. The magnitude of the observed deflection must, however, be interpreted in the context of the near-balanced design of the SATR. As characterised in Section 3.2.3, the gravitational restoring moment of the SATR is very small ($l_{\mathrm{cm}} \approx 5$ mm). Because this restoring moment is what opposes any pitch torque at equilibrium, even a moderate parasitic torque from the tail rotor is sufficient to produce a significant steady-state pitch deflection. The large angles reported in Table 4.3 at high tail-rotor commands are therefore a consequence of the weak pitch restoring moment, rather than evidence of a severe mechanical misalignment. The very property that makes the SATR easy to lift in pitch also makes it highly sensitive to disturbances coming from the tail rotor.

To evaluate this effect, the main rotor is kept at neutral throttle (1500 µs), while the tail rotor PWM is decreased step by step from 1500 µs to 1100 µs. Each PWM level is held for approximately 3 s, and the resulting pitch angle is recorded by the encoder.

The measured response shows that the pitch coupling remains negligible for near-neutral PWM values. Down to approximately 1250 µs, the pitch angle remains below about 1.3°. However, the effect becomes significant at larger tail commands: the pitch angle reaches approximately 28° at 1200 µs, about 77° at 1150 µs, and finally almost 88° at 1100 µs.

Tail PWM command	Measured pitch angle
1500 µs	0.0°
1450 µs	0.0°
1400 µs	0.18°
1350 µs	0.18°
1300 µs	0.18°
1250 µs	1.26°
1200 µs	28.0°
1150 µs	77.0°
1100 µs	87.7°

Table 4.3: Open-loop tail-rotor coupling measured on the SATR. The main rotor is kept at neutral throttle while the tail rotor command is varied.

This result demonstrates that the SATR cannot be considered as a perfectly decoupled single-input single-output (SISO) pitch prototype when the tail rotor is commanded at high levels. The coupling is negligible for near-neutral PWM values, but becomes dominant close to maximum tail actuation. This observation is important for the TRMS: even if the simplified TRMS model assumes geometric decoupling between pitch and yaw torques, the real platform is expected to exhibit coupling effects that must be taken into account during future MIMO identification and controller design.

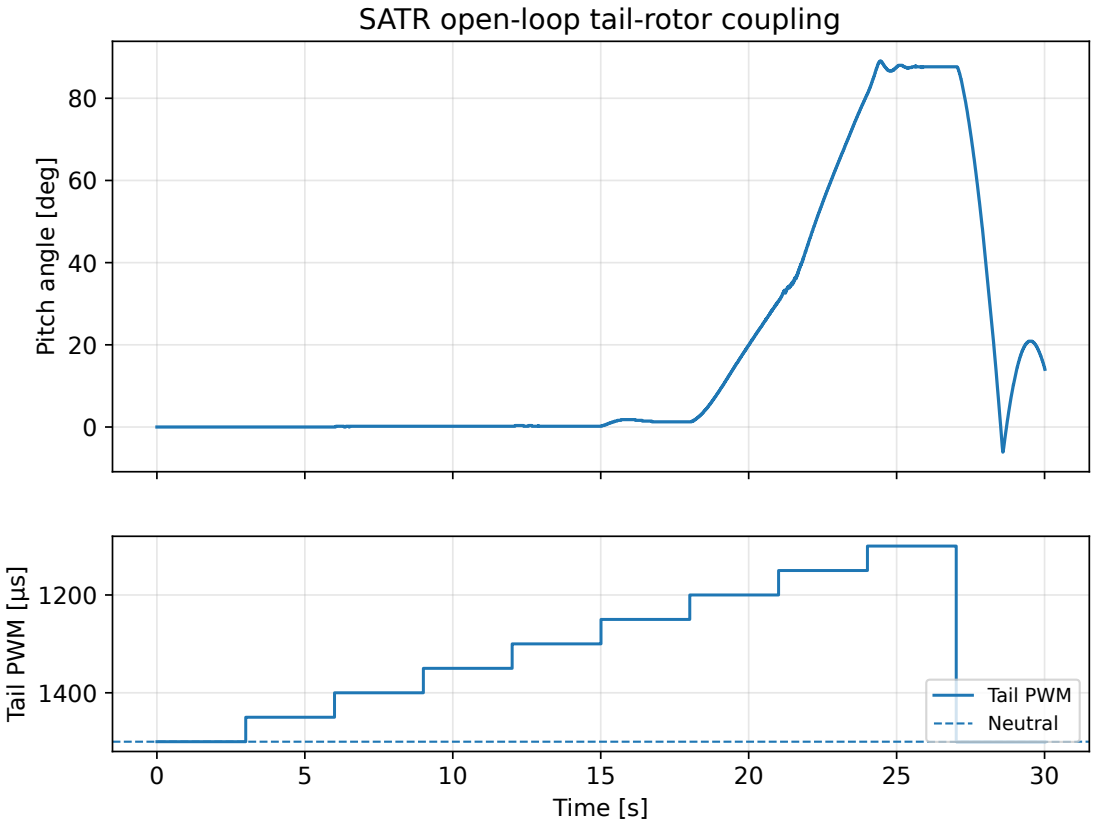


Figure 4.8: Open-loop SATR tail-rotor coupling test. The main rotor is kept at neutral throttle while the tail rotor command is stepped from neutral to maximum actuation.

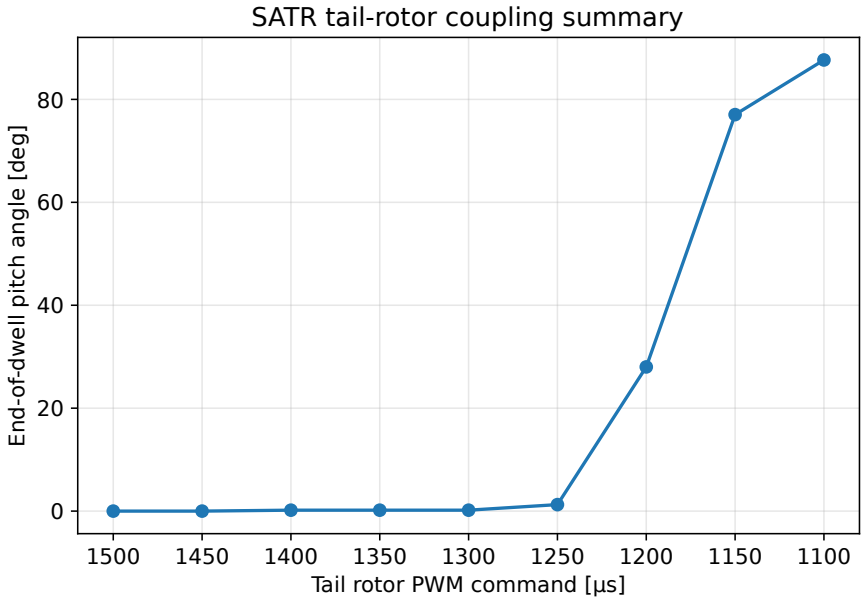


Figure 4.9: Measured pitch angle as a function of the tail rotor PWM command. The parasitic pitch coupling remains small up to approximately 1250 µs and then increases rapidly.

4.3.4 SATR validation summary

The SATR validation confirms that the electromechanical architecture validated on the AP can be transferred to a two-rotor configuration. The pitch loop reaches setpoints up to 80° with negligible steady-state error, without requiring any gravity feedforward term. This confirms the mechanical benefit of the more balanced SATR design and validates the use of integral action to compensate the remaining small errors.

The open-loop tail-rotor test also reveals an important limitation: the tail rotor produces a non-negligible parasitic pitch effect at high command levels. This supports the modelling choice made in Chapter 3, where the TRMS coupling terms are treated as disturbances in the simplified model and identified as future work for complete MIMO control.

4.4 Validation summary

The experimental validation confirms the progressive role of the AP and SATR prototypes in the development of the final TRMS platform. The AP validates the pitch control loop with a single rotor in a difficult configuration, with a heavy V1 cage and a large gravitational moment. The controller manages to reach a maximum pitch angle of approximately 25° with small steady-state error, while the 30° test reveals the practical limit of the AP configuration.

The SATR validation confirms that the same embedded architecture can be moved to a more balanced twin-rotor structure. The pitch controller reaches pitch angles up to approximately 80° without gravity feedforward, showing that the mechanical design of the SATR strongly reduces the need for compensation. The open-loop tail-rotor test also reveals a significant parasitic pitch coupling at high tail commands, which confirms that the final TRMS should not be treated as two perfectly independent single-axis systems.

Overall, the experiments validate the AP and SATR as intermediate prototypes for the development of the final dual-rotor platform. The full TRMS was assembled and checked mechanically and electrically, but its future closed-loop validation is left as future work.

Chapter 5

Conclusion: Improvements and Future Work

5.1 Summary of contributions

The objective of this master's thesis was to design, build, and progressively validate a dual-rotor aero-system intended for future education and research activities in control engineering at the EPL control laboratory. The motivation was to provide an open, modifiable, and reproducible alternative to commercial dual-rotor laboratory platforms, in particular the Quanser Aero 2, giving the laboratory access to the mechanical design files, the electrical architecture, and the embedded control code required for future maintenance, extension, and pedagogical adaptation.

The work was conducted through an incremental prototyping strategy. Instead of building the complete Twin Rotor MIMO System (TRMS) directly, three prototypes of increasing complexity were designed and built. The aero-pendulum (AP) was used to validate the single-axis actuation and sensing chain in a worst-case configuration. The single-axis twin-rotor prototype (SATR) then introduced a second actuator, the tail rotor, and a more balanced mass distribution while keeping the yaw axis mechanically constrained. Finally, the complete TRMS integrated the two degrees of freedom through a dedicated pitch and yaw pivot architecture.

From a mechanical point of view, this work produced numerous custom 3D-printed components and assemblies for the three prototypes. The AP validated the first pivot architecture, encoder integration, motor link, and the first propeller cage concept. The SATR then introduced the centred pivot and the improved V2 propeller cage. Finally, the TRMS extended this architecture to two DoF through separate pitch and yaw pivot arrangement, constructed around a carbon-fibre pitch shaft, an M6 yaw rod, a U-shape connector, a support tower, and mechanical locking pins. This resulted in a

mechanically assembled platform that provides a solid basis for future MIMO pitch and yaw control experiments.

From an electrical and embedded point of view, the project validated a complete architecture based on a Raspberry Pi 4 for sensing, actuation, real-time control, and data logging. The BNO085 IMU provides attitude measurements based on quaternions and sensor fusion, while the HEDS-5540 encoder was integrated and validated on the AP and SATR prototypes as an independent, drift-free angular position sensor. The A2212 brushless motors are controlled through Basic ESC 30A units in bidirectional mode. The embedded code implements PWM generation, slew-rate limitation, neutral dwell protection, sensor selection, PID computation, and CSV logging.

The control chapter provides a simplified dynamic model of each prototype, an experimental identification campaign, and a validation of the PID controller on the AP and SATR. Passive drop tests were performed on the AP and SATR to identify the pitch inertia and damping parameters of the prototypes. The agreement between the CAD-derived inertias and the experimentally fitted values confirmed that the SolidWorks model was sufficiently accurate for the purpose of this work. The controller was then tuned empirically and used as a validation tool for the electromechanical design rather than as an independent contribution to control theory.

The experimental validation conducted on the AP and SATR prototypes confirmed the utility of the incremental approach. The AP was successfully stabilised up to approximately 25° using a PID controller with gravity feedforward, while the 30° test demonstrated the practical actuator limit of the V1 configuration. On the SATR prototype, the same control architecture was successfully ported to the two-rotor configuration, which reached pitch setpoints up to 80° without gravity feedforward. The open-loop tail-rotor test also revealed a significant parasitic pitch coupling at high tail PWM commands, confirming that the complete TRMS should not be treated as two perfectly independent single-axis systems.

Ultimately, this thesis demonstrates that the proposed architecture is suitable as an open and reproducible platform for a dual-rotor educational system. The AP and SATR prototypes validate the sensing, actuation, embedded software, identification, and closed-loop pitch control chain. The final TRMS is mechanically and electrically operational as a physical prototype, while complete closed-loop MIMO validation remains for future work.

5.2 Comparison with the Quanser Aero 2

The developed platform should not be interpreted as a direct performance replacement for the Quanser Aero 2. The Quanser Aero 2 remains a mature, compact, industrially manufactured laboratory system with calibrated hardware, robust mechanics, and a complete software environment. It is therefore better suited for direct deployment in teaching laboratories when the objective is to focus only on controller design and experimental operation, without modifying the hardware or the embedded implementation.

The contribution of the present platform is different. Its main value lies in its openness and modifiability. The mechanical parts are designed from standard aluminium profiles and 3D-printed components, the sensors and actuators are commercially available, and the embedded control loop runs on a Raspberry Pi using accessible Python code. This makes the system easier to inspect, repair, modify, and extend. For an educational laboratory, this openness is valuable because it allows students and future thesis projects to engage not only with the controller, but also with the complete physical chain that connects mechanical design, sensing, actuation, embedded implementation, modelling, and experimental validation.

Compared with the Quanser Aero 2, the present platform is therefore less mature but more transparent. It is not yet a ready-to-use laboratory product, but it provides the EPL control laboratory with a documented experimental basis that can be adapted to future pedagogical needs. Additional sensors can be integrated, mechanical parts can be redesigned, and alternative control strategies can be implemented without depending on proprietary hardware or software. This makes the platform particularly relevant for laboratories or student projects where understanding and modifying the system are part of the learning objectives.

5.3 Limitations of the current prototype

Several limitations remain in the current state of the project. The most important one is that the complete TRMS has not yet been validated in closed-loop MIMO operation in pitch and yaw. The final prototype has been mechanically assembled and electrically checked, but the full coupled control campaign was not completed within the thesis schedule. The AP and SATR experiments therefore validate the main building blocks of the platform, but they do not yet demonstrate complete MIMO control of the final system.

A second limitation concerns the sensing architecture of the final TRMS. The HEDS-5540 encoder was successfully integrated and validated on the AP and SATR

prototypes, but it was not mechanically mounted on the final TRMS at the time of writing. As a result, the final TRMS currently relies on the BNO085 IMU for pitch and yaw measurements. This is sufficient for preliminary bench checks, but future closed-loop MIMO control would benefit from independent encoder measurements, especially for yaw, where IMU drift and fusion latency can become limiting factors.

The actuator model also remains simplified. The motor–ESC–propeller assembly is represented through an effective static gain, and the actuator time constant is not identified directly because no motor-speed sensor is mounted on the shaft. This approximation was sufficient for empirical PID tuning on the AP and SATR, but it does not provide a detailed dynamic model of the actuation chain. The strong asymmetry between lifting and opposing actuation is another important limitation. The selected CCW propellers are efficient in their nominal direction but much less effective in reverse, which restricts the usefulness of bidirectional control and motivates the one-sided actuation policy used in the validation experiments.

The aerodynamic influence of the propeller cages is another limitation. The V1 cage used on the AP was heavy and penalising, limiting the reachable pitch range of the prototype. The V2 cage used on the SATR and TRMS improves the mechanical design, but its aerodynamic losses were not characterised in detail. These losses are absorbed empirically into the tuned controller gains, especially the gravity feedforward gain on the AP, rather than being modelled explicitly.

Finally, the identification campaign has its own limitations. The AP drop tests provided reliable estimates of inertia and damping because several oscillations were observed. On the SATR, however, the mechanical layout allowed only a single large-amplitude descent before the arm reached the structural stop. This was sufficient to cross-check the inertia, but not to identify the damping coefficient with the same confidence. Since the controller was tuned empirically, this did not prevent closed-loop validation, but it limits the possibility of deriving analytical gains from a fully identified model.

5.4 Future work

The first priority for future work is the completion of the final TRMS assembly into a fully usable laboratory prototype. Although the main mechanical structure is assembled, the platform still requires a clean integration of the remaining hardware, including a dedicated enclosure for the electronics and the Raspberry Pi display. This final integration should also include proper cable routing, mechanical protection of the control electronics, and a more practical user interface for laboratory operation. In

parallel, the encoder integration should be completed on the final prototype, either on the yaw axis, the pitch axis, or both, depending on the selected sensing strategy.

Once the final prototype is fully instrumented, the next step is the control-oriented characterisation of the TRMS. The first experiments should validate each axis separately using the mechanical locking pins: pitch control with the yaw axis locked, and yaw control with the pitch axis locked. This would provide a controlled transition between the SATR validation and the full 2-DoF TRMS operation. A dedicated system-identification campaign should then be performed on the final prototype to estimate the pitch and yaw dynamics, the residual gravitational effects, the damping, and the coupling between both axes.

The actuator characterisation should also be improved. A direct thrust stand or motor-speed measurement would allow the motor–ESC–propeller dynamics to be identified independently from the arm dynamics. This would clarify the relation between PWM command, motor speed, propeller force, and effective torque applied to the platform. Such a campaign would also make it possible to quantify the forward–reverse asymmetry more precisely and to evaluate whether alternative propellers with more symmetric bidirectional behaviour could improve the controllable workspace of the TRMS.

The propeller cages should also be characterised further. The AP results showed that the cage can have a strong influence on both mass distribution and actuation efficiency. Future work could therefore include direct thrust tests with and without the cage, comparisons between cage designs, or CFD simulations of the airflow around the propeller guards. This would help separate aerodynamic losses from controller tuning effects and could guide a lighter and less dissipative cage design.

Another important extension is the development of a communication interface between MATLAB and the experimental plant. In the present work, the control loop is executed directly on the Raspberry Pi through Python scripts. For future laboratory use, a MATLAB interface would allow students to send references, tune parameters, retrieve measurements, and analyse experimental data directly from the MATLAB environment. This would make the platform easier to integrate into existing control courses and would bring it closer to the workflow of commercial educational systems, while keeping the hardware and software architecture open.

From a control perspective, the present PID strategy should be seen as a baseline. After the single-axis validation and the identification of the coupled dynamics, a first full TRMS controller could be implemented as two conservatively tuned PID loops for pitch and yaw. If the coupling effects are significant, more advanced strategies should then be considered, such as decoupling control, cascaded control, an LQR controller, or

multivariable control methods accounting for pitch and yaw coupling, gyroscopic effects, actuator asymmetry, and gravitational effects.

The platform also opens several pedagogical extensions. Future laboratory sessions could ask students to compare encoder-only, IMU-only, and fused sensor feedback. They could also try to implement complementary or Kalman filtering, to identify actuator dynamics experimentally, to tune PID gains on the real system, or to compare single-axis and coupled control strategies. Because the platform is open, students can also inspect the mechanical design, modify the CAD files, understand the wiring, and work directly with the embedded code.

In conclusion, this thesis produced a functional and documented electromechanical basis for an open dual-rotor aero-system. The AP and SATR prototypes demonstrate that the selected mechanical, electrical, sensing, actuation, and embedded-control choices are suitable for closed-loop experiments. The final TRMS prototype is assembled and ready for final integration, instrumentation, identification, and full pitch and yaw control validation. Once these steps are completed, the platform will provide the EPL control laboratory with a flexible and reproducible experimental system for education and research in nonlinear and multivariable control.

Bibliography

[1] A. Soenen, "From model-based to data-driven control: Applications to self-balancing robots," M.S. thesis, Université catholique de Louvain, 2024. [Online]. Available: https://hdl.handle.net/2078.2/37475

[2] *Aero 2: Reconfigurable dual-rotor aerospace experiment for controls education and research*, Product datasheet, Quanser Inc., 2022. [Online]. Available: https://quanserinc.box.com/shared/static/0y4nbjzt1ea3rug3k3pkf5urrmsmuxtn.pdf

[3] *HEDM-55xx/560x & HEDS-55xx/56xx Quick Assembly Two and Three Channel Optical Encoders*, Data sheet, AV02-1046EN, November 20, 2014, Avago Technologies, Nov. 2014.

[4] APC Propellers, *8x4 Propeller Performance Data*, https://www.apcprop.com/files/PER3_8x4.dat, Performance data file, version v2022-0915, simulation date: September 22, 2022, Sep. 2022.

[5] J. Brandt and M. Selig, "Propeller Performance Data at Low Reynolds Numbers," en, in *49th AIAA Aerospace Sciences Meeting including the New Horizons Forum and Aerospace Exposition*, Orlando, Florida: American Institute of Aeronautics and Astronautics, Jan. 2011, ISBN: 978-1-60086-950-1. DOI: 10.2514/6.2011-1255 [Online]. Available: https://arc.aiaa.org/doi/10.2514/6.2011-1255

[6] *A2212/13T Technical Data*, Motor data sheet, MOTOR-KV1000, Olimex Ltd.

[7] *Basic ESC Documentation (New)*, Electronic speed controller documentation, forward/reverse BLHeli_S firmware, Blue Robotics, Jan. 2018. [Online]. Available: http://docs.bluerobotics.com/bescr3/

[8] *Raspberry Pi 4 Model B Datasheet*, Release 1.1, RP-008341-DS-1, Raspberry Pi (Trading) Ltd., Mar. 12, 2024. [Online]. Available: https://www.raspberrypi.org

[9] *Laboratory Power Supply: Operating Instructions*, Operating instructions for DPPS-16-30, 1–16 V/DC, 0–30 A, item no. 1086555, Voltcraft. [Online]. Available: https://www.conrad.com/en/p/voltcraft-dpps-16-30-bench-psu-adjustable-voltage-1-16-v-dc-0-30-a-480-w-usb-programmable-no-of-outputs-1-x-1086555.html#productDownloads

[10] E. T. Enikov and G. Campa, "Mechatronic Aeropendulum: Demonstration of Linear and Nonlinear Feedback Control Principles With MATLAB/Simulink Real-Time Windows Target," en, *IEEE Transactions on Education*, vol. 55, no. 4, pp. 538–545, Nov. 2012, ISSN: 0018-9359, 1557-9638. DOI: 10.1109/TE.2012.2195496 [Online]. Available: http://ieeexplore.ieee.org/document/6193186/

[11] CEVA, Inc., *BNO08X datasheet: SH-2 SiP sensor hub module with integrated 9-axis MEMS sensors*, Rev. 1.17, https://www.ceva-ip.com/wp-content/uploads/BNO080_085-Datasheet.pdf, CEVA, Inc., 2023.

[12] Joan, *pigpio*, https://github.com/joan2937/pigpio, Software library for Raspberry Pi GPIO control, latest release v79.

[13] Adafruit Industries, *Adafruit CircuitPython BNO08x*, https://github.com/adafruit/Adafruit_CircuitPython_BNO08x, Software library for BNO08x IMUs.

[14] L. Belmonte, R. Morales, A. Fernández-Caballero, and J. Somolinos, "Robust Decentralized Nonlinear Control for a Twin Rotor MIMO System," en, *Sensors*, vol. 16, no. 8, p. 1160, Jul. 2016, ISSN: 1424-8220. DOI: 10.3390/s16081160 [Online]. Available: https://www.mdpi.com/1424-8220/16/8/1160

[15] A. Rahideh, M. Shaheed, and H. Huijberts, "Dynamic modelling of a TRMS using analytical and empirical approaches," en, *Control Engineering Practice*, vol. 16, no. 3, pp. 241–259, Mar. 2008, ISSN: 09670661. DOI: 10.1016/j.conengprac.2007.04.008 [Online]. Available: https://linkinghub.elsevier.com/retrieve/pii/S0967066107000962

[16] W. Selby, *Quadrotor model verification: An experimentally derived accurate model*, https://wilselby.com/research/arducopter/model-verification/.

[17] J. Eschmann, D. Albani, and G. Loianno, "Data-Driven System Identification of Quadrotors Subject to Motor Delays," en, in *2024 IEEE/RSJ International Conference on Intelligent Robots and Systems (IROS)*, Abu Dhabi, United Arab Emirates: IEEE, Oct. 2024, pp. 8095–8102, ISBN: 979-8-3503-7770-5. DOI: 10.1109/IROS58592.2024.10801441 [Online]. Available: https://ieeexplore.ieee.org/document/10801441/

[18] S. Gustin, "Design and implementation of a simplified aircraft model for the study of roll stabilization in turbulence," M.S. thesis, Université catholique de Louvain, 2025. [Online]. Available: https://hdl.handle.net/2078.2/46249

[19] J. K. Pradhan and A. Ghosh, "Design and implementation of decoupled compensation for a twin rotor multiple-input and multiple-output system," en, *IET Control Theory & Applications*, vol. 7, no. 2, pp. 282–289, Jan. 2013, ISSN: 1751-8644, 1751-8652. DOI: 10.1049/iet-cta.2012.0162 [Online]. Available: https://ietresearch.onlinelibrary.wiley.com/doi/10.1049/iet-cta.2012.0162

[20] A. Phillips and F. Sahin, "Optimal control of a twin rotor MIMO system using LQR with integral action," en, in *2014 World Automation Congress (WAC)*, Waikoloa, HI: IEEE, Aug. 2014, pp. 114–119, ISBN: 978-1-889335-49-0. DOI: 10.1109/WAC.2014.6935709 [Online]. Available: http://ieeexplore.ieee.org/document/6935709/

Appendices

Appendix A

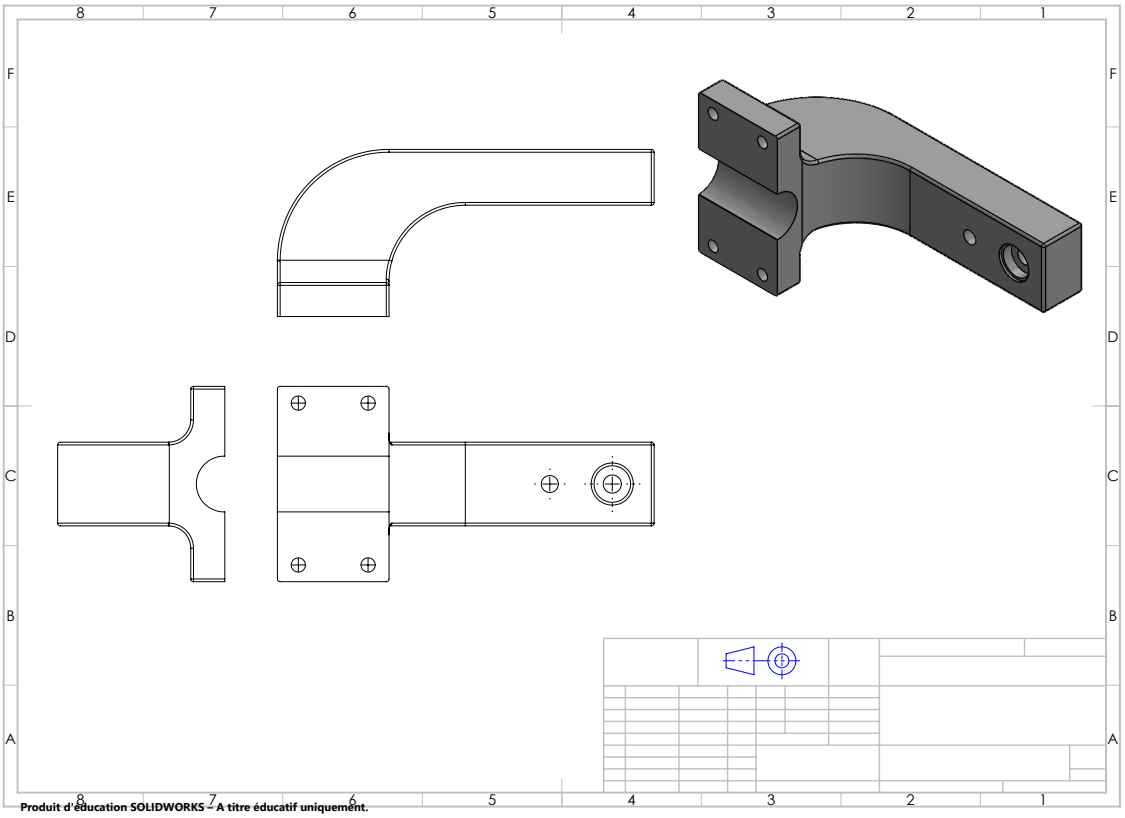
Specification Chart

Date	Specifications
Functions	
19/02/26	F1: Provide two degrees of freedom (pitch and yaw).
19/02/26	F2: Actuate the platform with two rotors.
19/02/26	F3: Reproduce the coupled MIMO dynamics of a twin-rotor system.
19/02/26	F4: Allow closed-loop trajectory tracking on both axes.
19/02/26	F5: Measure attitude on both axes (pitch and yaw).
19/02/26	F6: Execute the control loop in real time.
23/04/26	F7: Allow independent locking of each axis for incremental testing.
Functional Requirements (FR)	
23/04/26	FR1.1: Pitch pivot designed for 360° rotation, usable range limited by cable routing.
23/04/26	FR1.2: Yaw range of approximately ±60° (120° total).
22/05/26	FR1.3: Wiring routed and secured to avoid entanglement over the usable rotation range.
12/03/26	FR2.1: Two A2212 brushless motors controlled through PWM.
12/03/26	FR2.2: Propellers sized to fit within the propeller cages.
19/02/26	FR2.3: Thrust sufficient to drive both axes over the usable range.
23/04/26	FR3.1: Pitch and yaw mechanically coupled, representative of TRMS cross-coupling.

Date	Specifications
12/03/26	FR4.1: Motor actuation in both directions to allow trajectory tracking.
26/03/26	FR5.1: Pitch measured by a rotary quadrature encoder.
23/04/26	FR5.2: Pitch measurement resolution $\leq 0.2°$ ($0.18°$ per tick after $\times 4$ decoding).
23/04/26	FR5.3: Yaw measured by the IMU (6-axis fusion).
26/03/26	FR6.1: Real-time control loop on a Raspberry Pi 4 (Python), update rate ≥ 200 Hz.
22/05/26	FR7.1: Mechanical locking pins to immobilise the pitch or yaw axis independently.
Constraints (C)	
23/04/26	C1: Safe for operation by students.
19/02/26	C2: Powered only from a laboratory bench supply (no LiPo batteries).
19/02/26	C3: Reproducible with common components and manufacturing processes.
23/04/26	C4: Fit on existing laboratory benches.
23/04/26	C5: Transportable by a single person.
19/02/26	C6: Open and modifiable design.
Constraint Requirements (CR)	
26/03/26	CR1.1: Each propeller fully guarded by a cage $\Rightarrow$ no contact possible with the blades.
23/04/26	CR2.1: Only use of a laboratory bench power supply (battery chemistry excluded).
19/02/26	CR3.1: Custom parts reproducible on a standard FDM 3D printer.
19/02/26	CR3.2: Purchased parts easily available from common retailers.
23/04/26	CR4.1: Base contained within an A3 footprint (420×297 mm).
23/04/26	CR5.1: Total mass low enough to be carried by one person.
23/04/26	CR6.1: Mechanical CAD, electrical schematics and embedded code documented and modifiable.

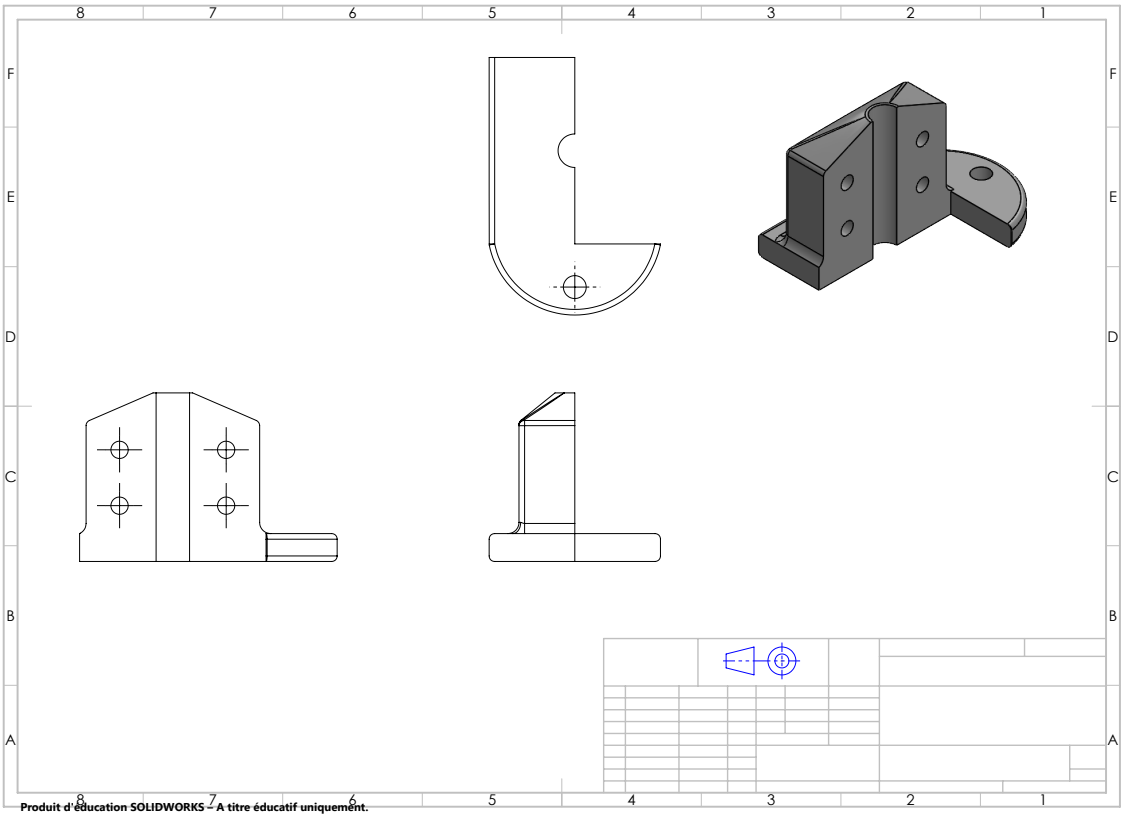
Appendix B

U-shape connector



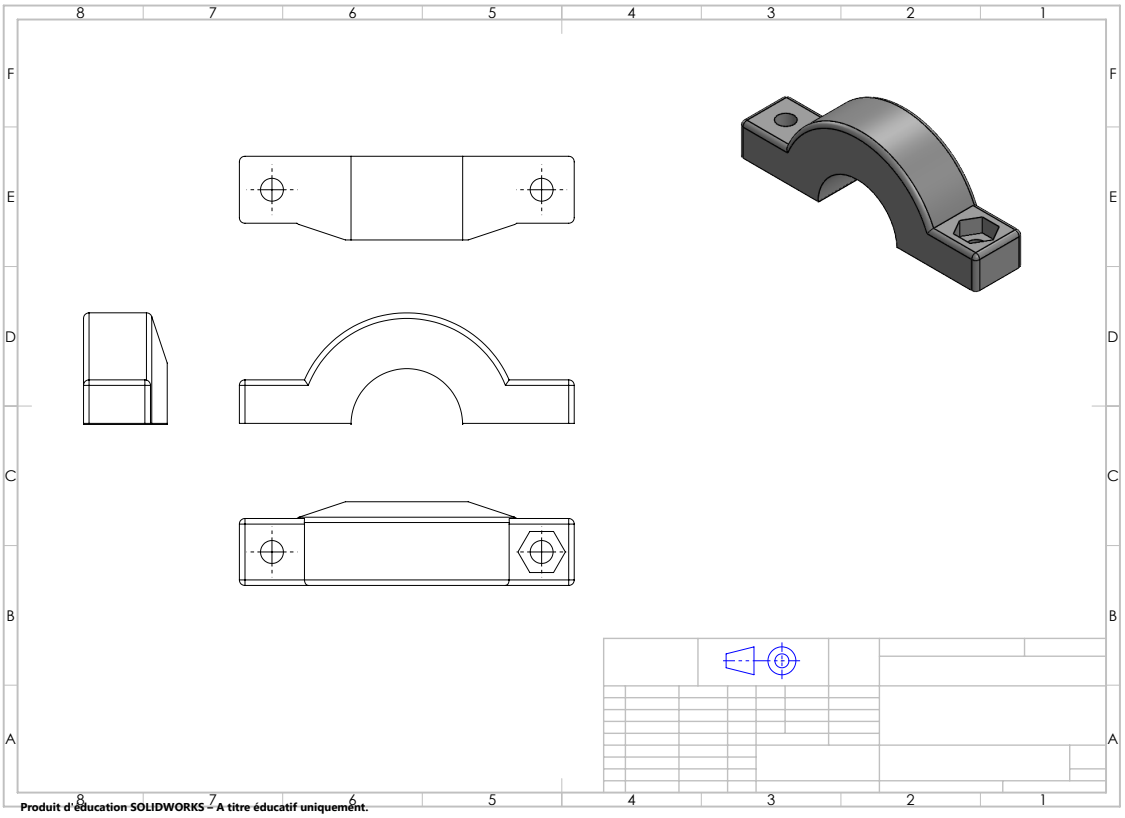
Appendix C

Connector M6 rod



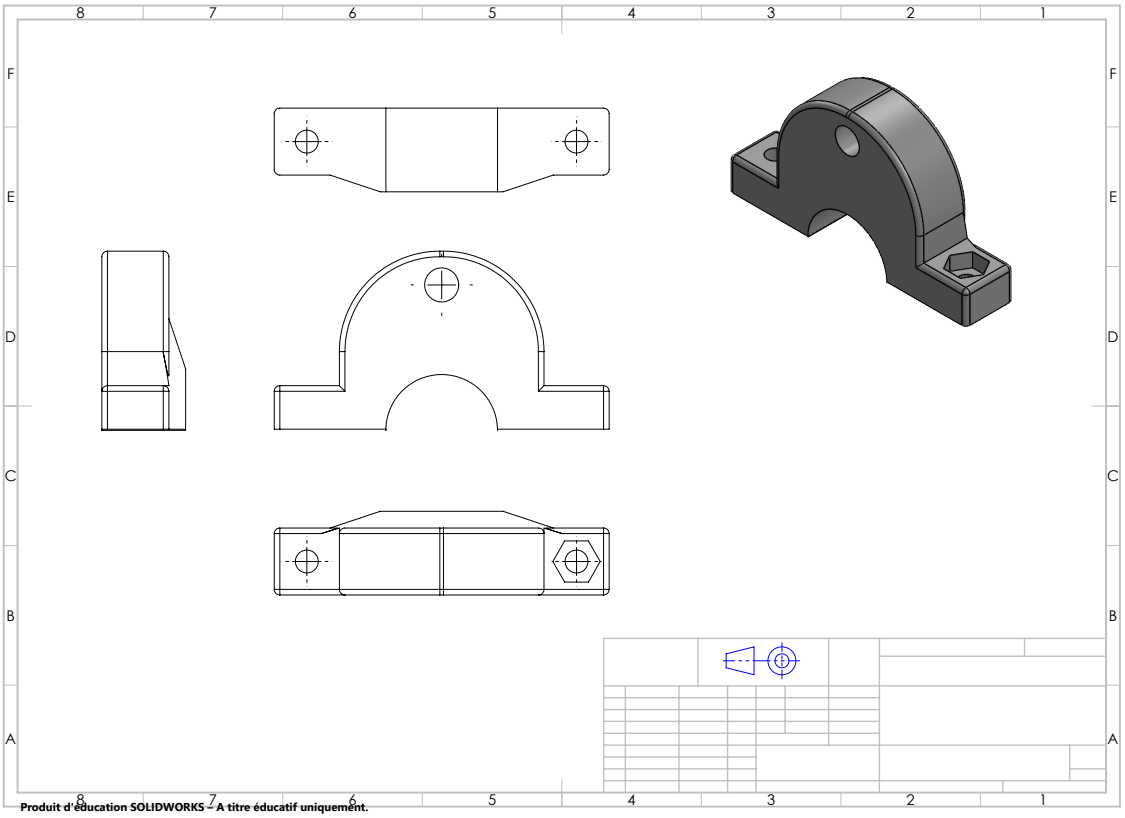
Appendix D

M18 rod ring



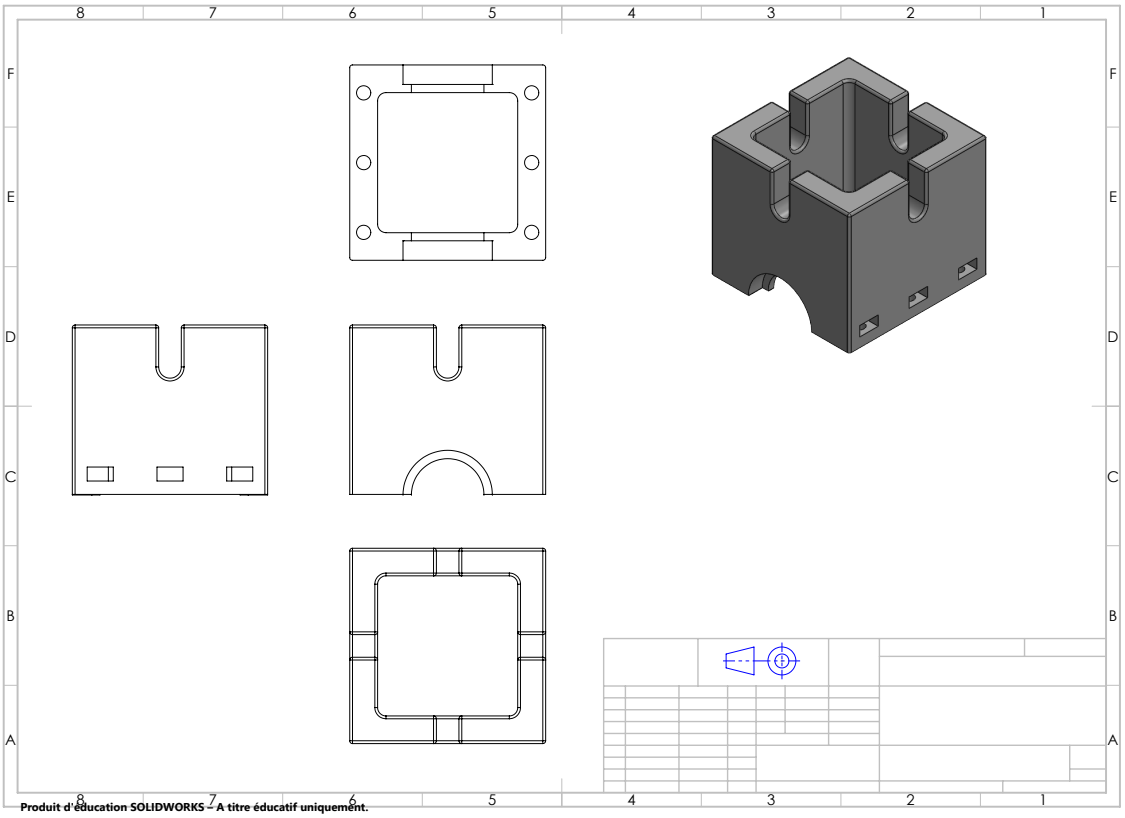
Appendix E

Extended M18 rod ring



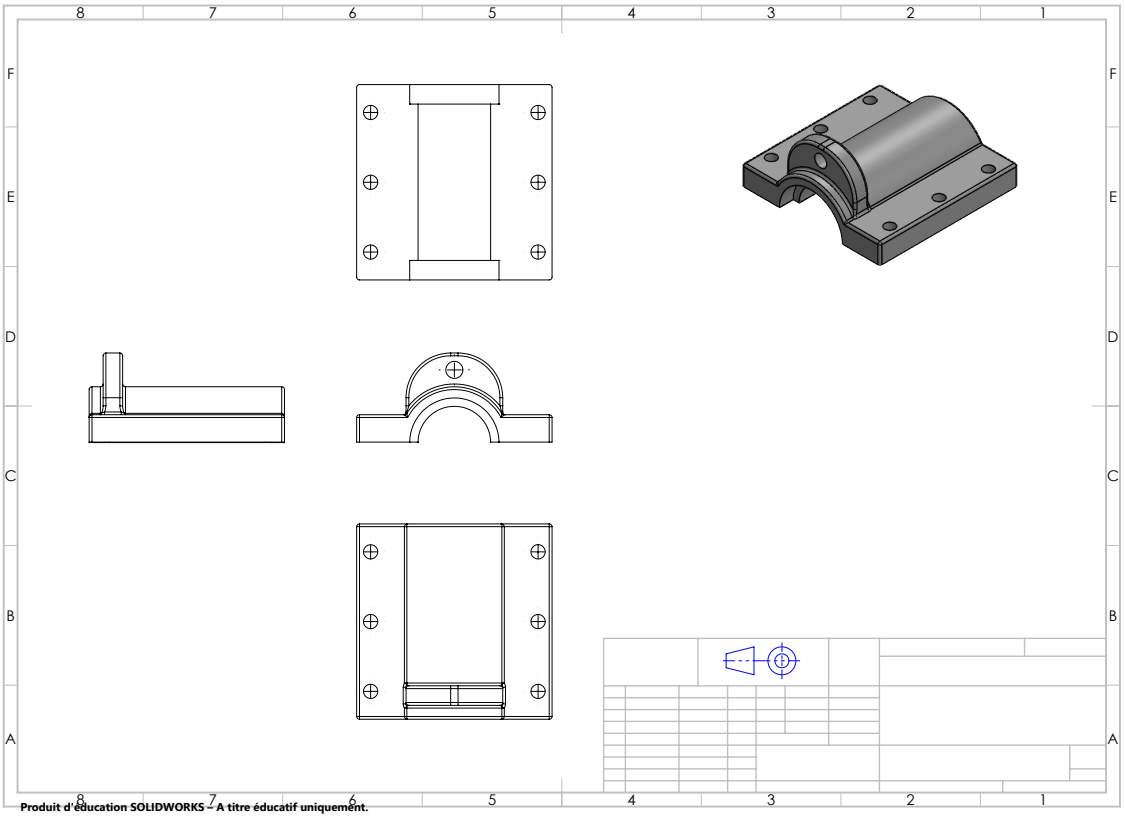
Appendix F

Pitch-axis lower connector



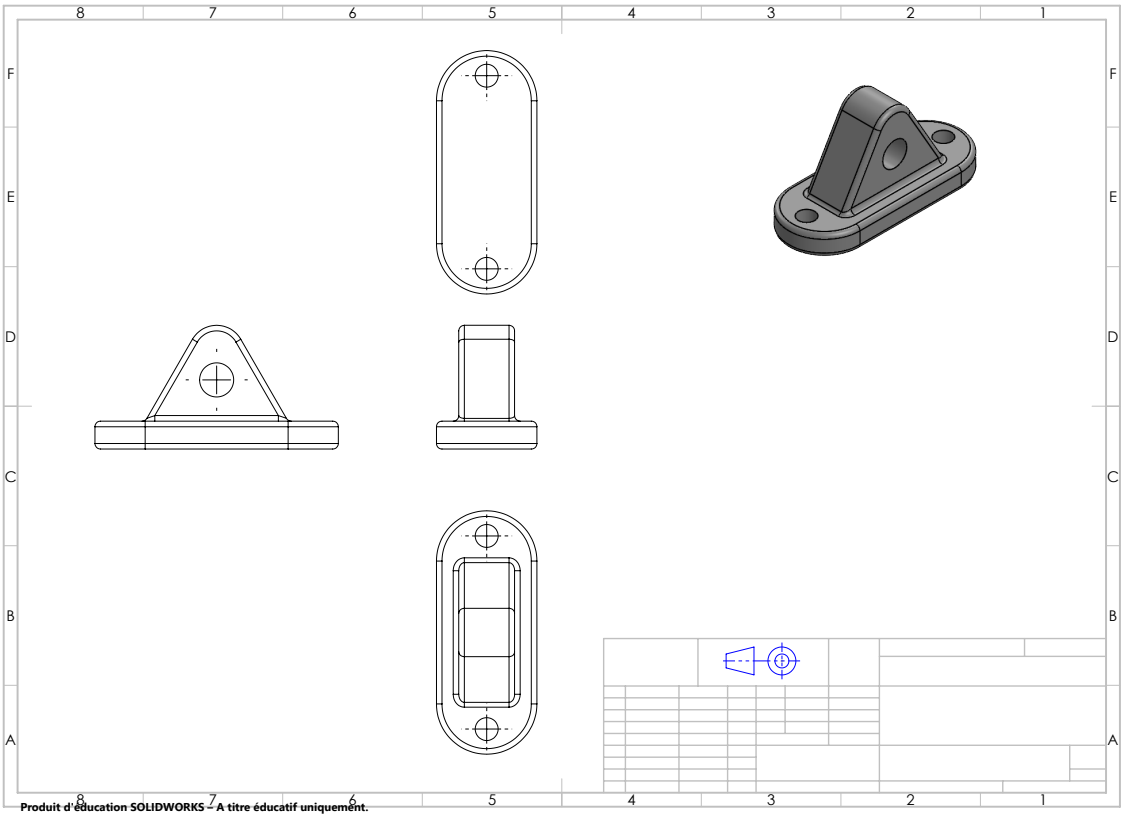
Appendix G

Pitch-axis upper connector



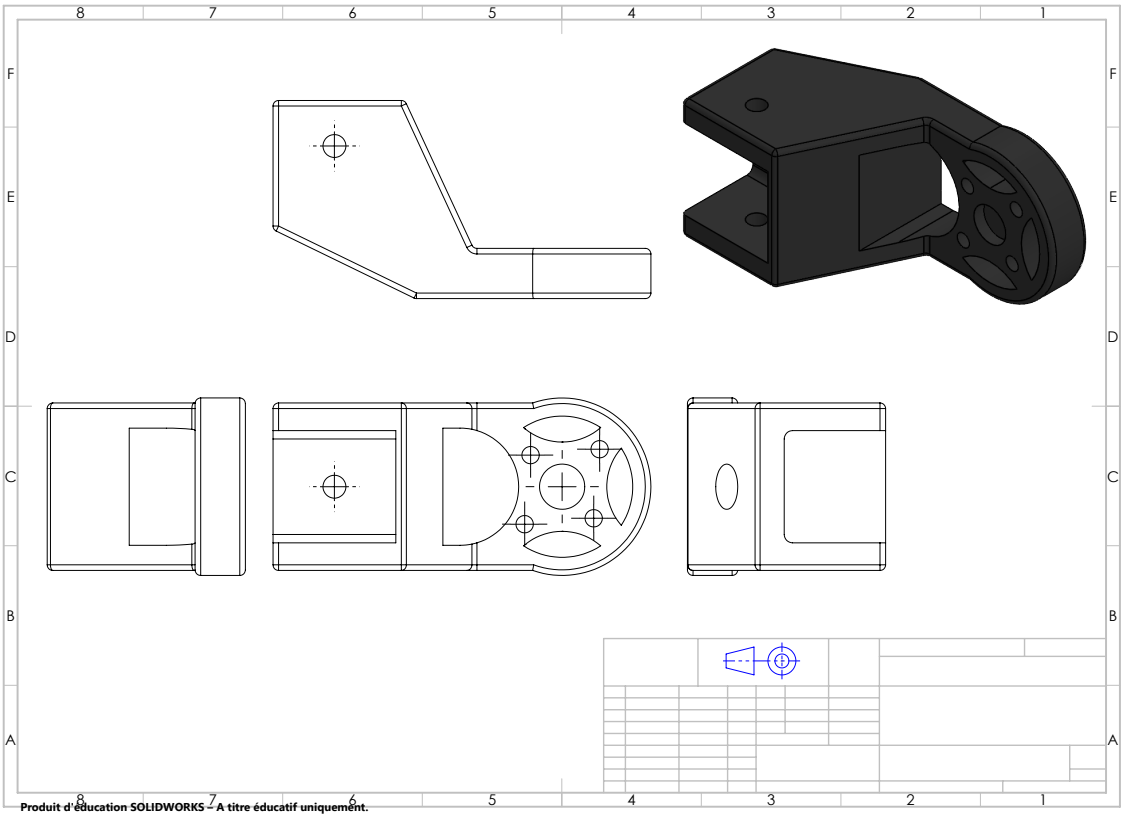
Appendix H

Yaw blocker connector



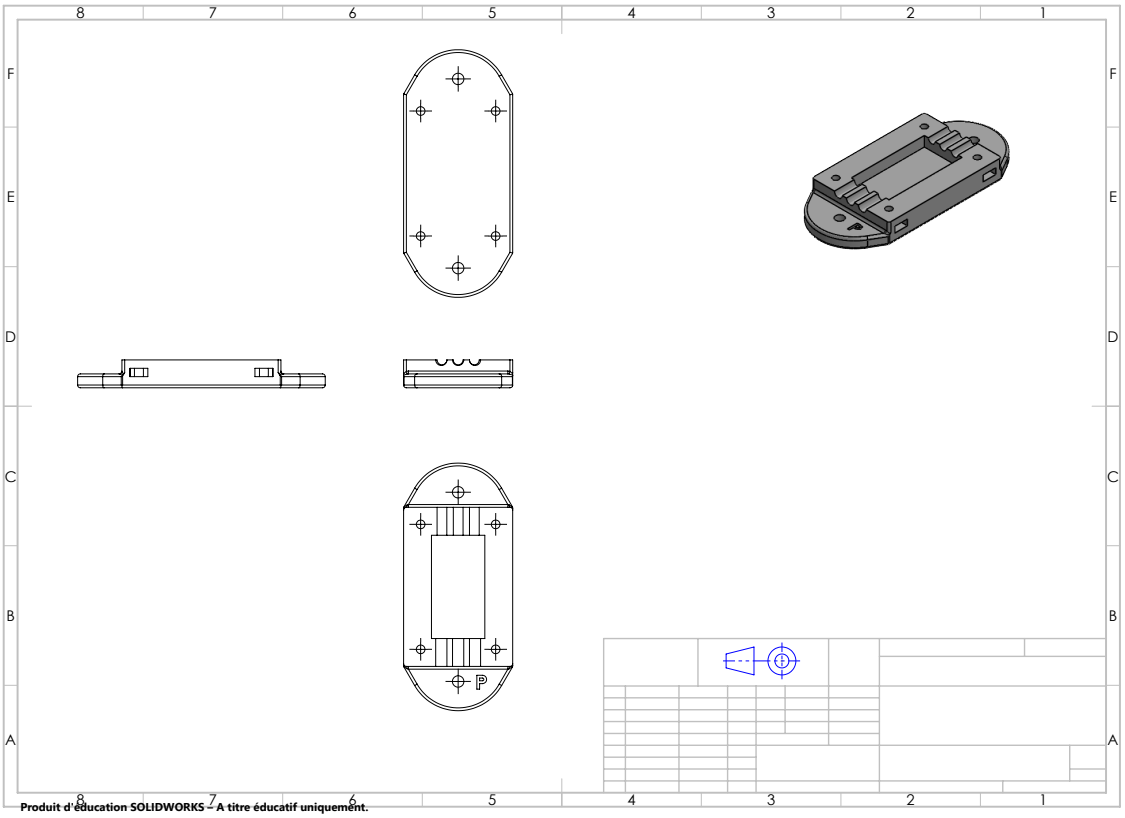
Appendix I

Motor link V2



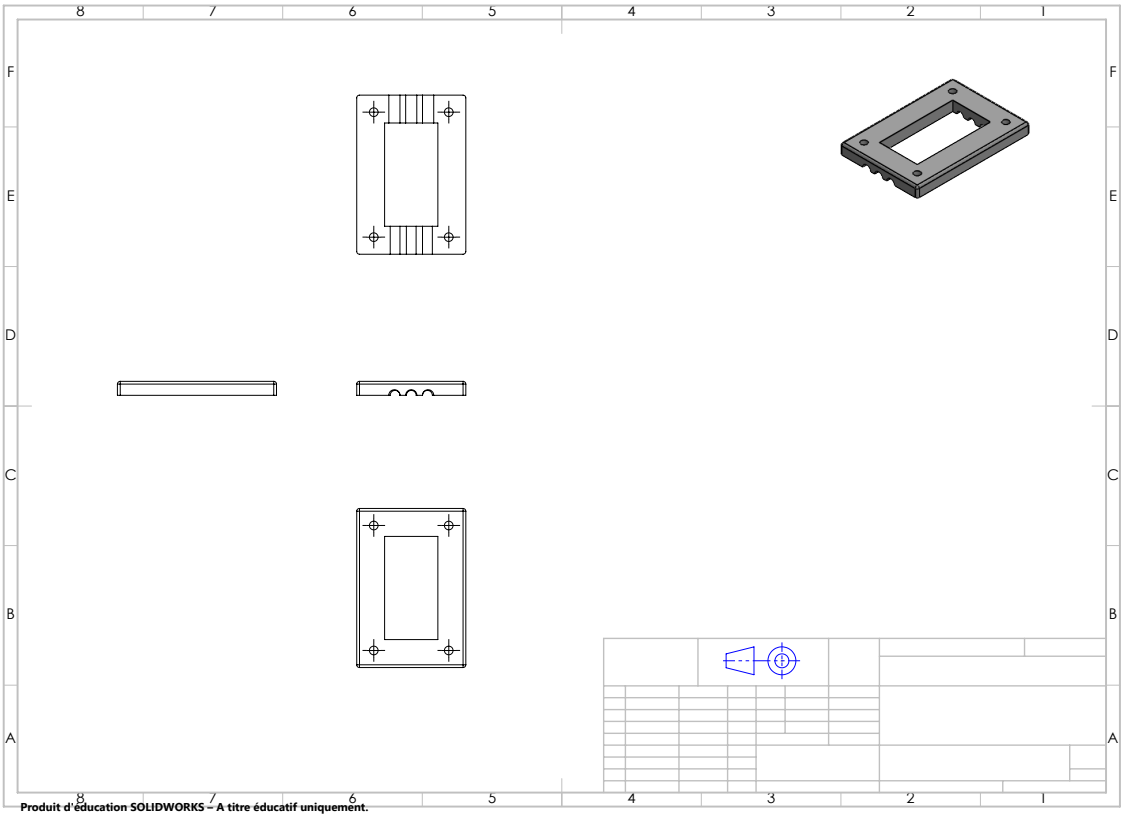
Appendix J

ESC lower connector



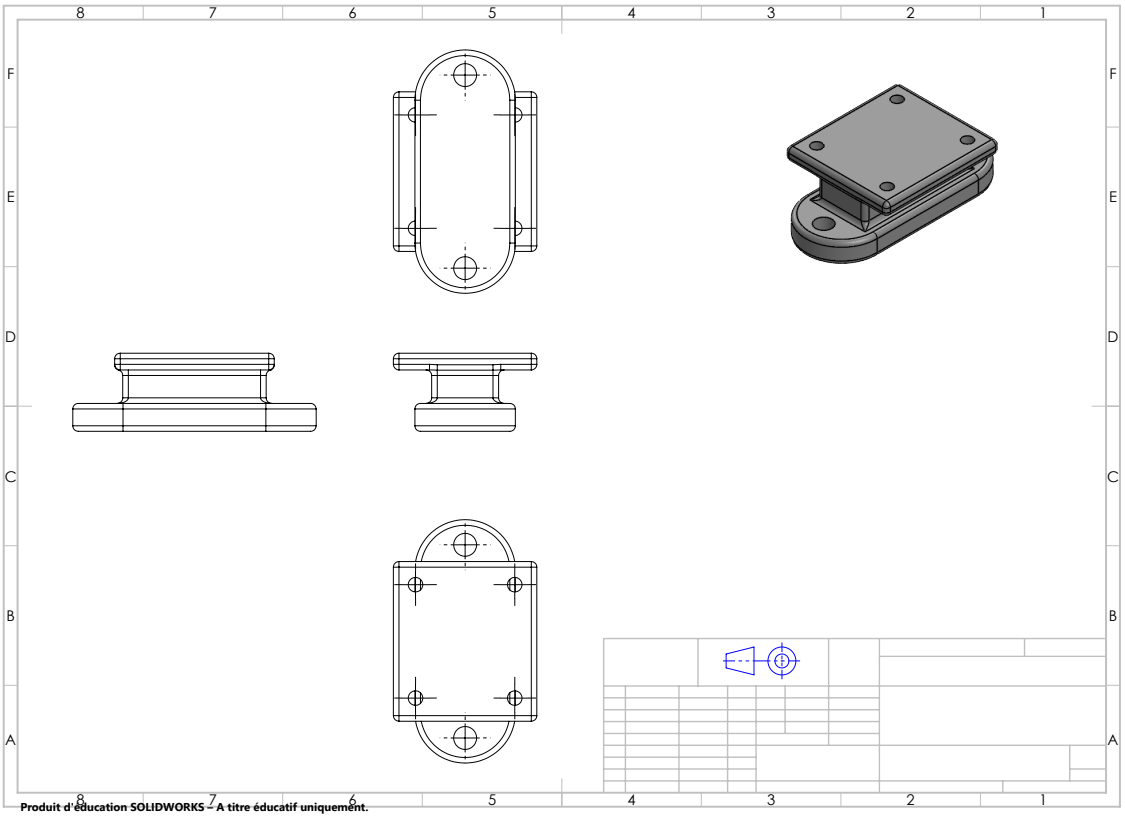
Appendix K

ESC upper connector



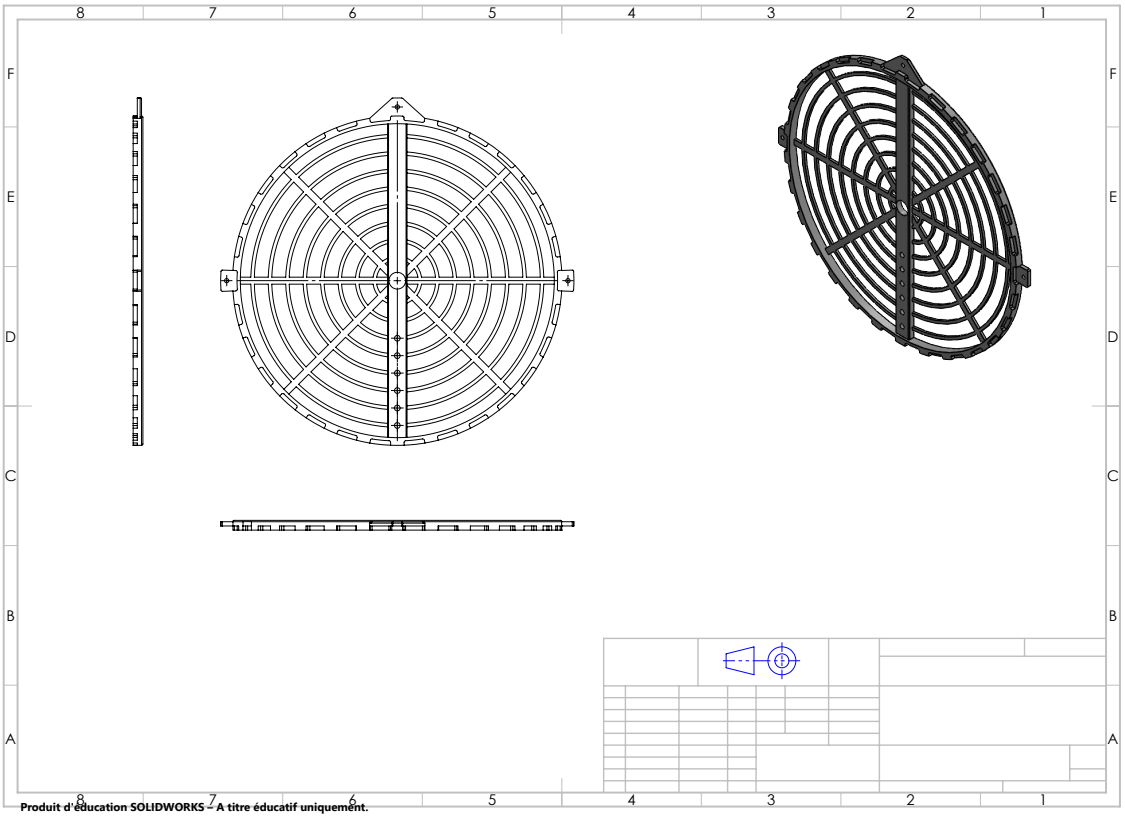
Appendix L

IMU connector



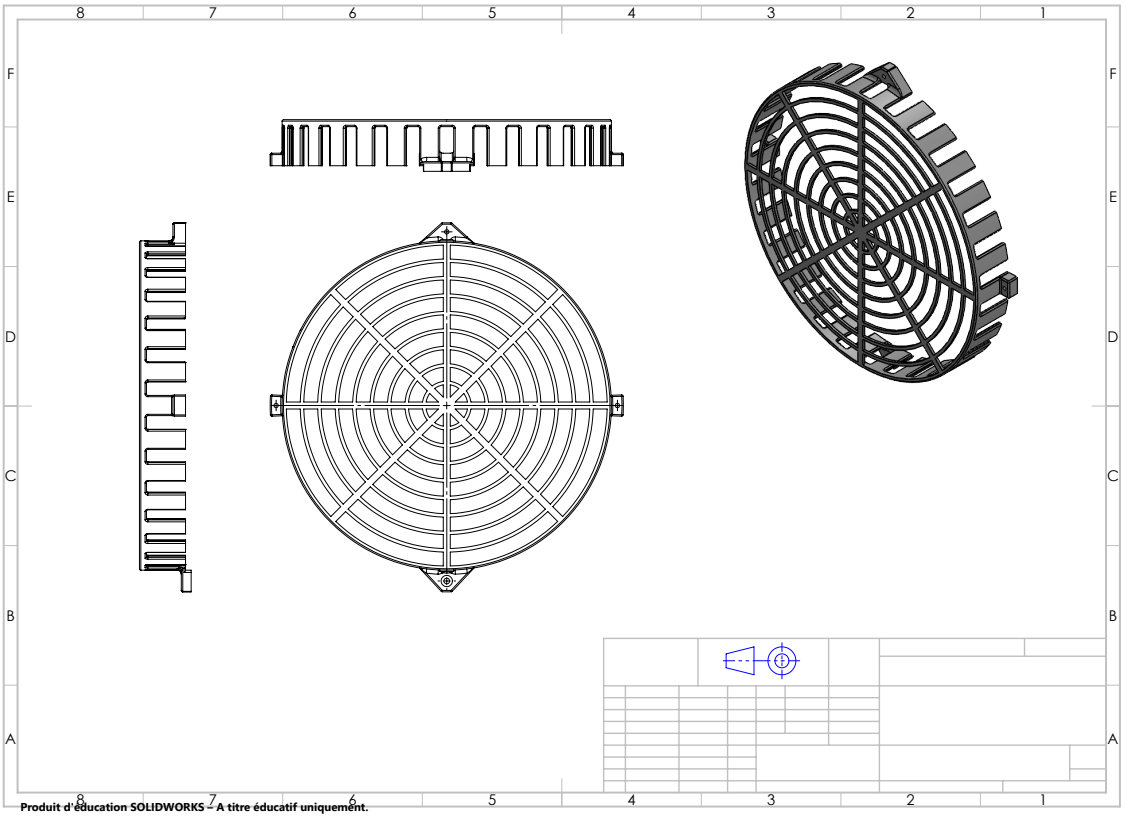
Appendix M

Propeller cage lower part



Appendix N

Propeller cage upper part



UNIVERSITÉ CATHOLIQUE DE LOUVAIN
École polytechnique de Louvain
Rue Archimède, 1 bte L6.11.01, 1348 Louvain-la-Neuve, Belgique | **www.uclouvain.be/epl**